

AD-A010 425

NONLINEAR DEFORMATION OF GRAPHITIC MATERIALS

SOUTHERN METHODIST UNIVERSITY

PREPARED FOR
AIR FORCE MATERIALS LABORATORY

FEBRUARY 1975

DISTRIBUTED BY.

NTIS

National Technical Information Service
U. S. DEPARTMENT OF COMMERCE

AD A010425

162079

AFML-TR-74-259

NONLINEAR DEFORMATION OF GRAPHITIC MATERIALS

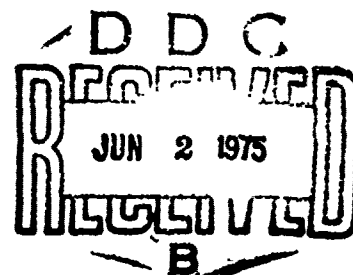
CIVIL & MECHANICAL ENGINEERING DEPARTMENT
SMU INSTITUTE OF TECHNOLOGY
DALLAS, TEXAS 75275

TECHNICAL REPORT AFML-TR-74-259

FEBRUARY 1975

FINAL REPORT FOR PERIOD MARCH 1973 - JUNE 1974

Approved for public release; distribution unlimited.



AIR FORCE MATERIALS LABORATORY
AIR FORCE SYSTEMS COMMAND
WRIGHT-PATTERSON AIR FORCE BASE, OHIO 45433

Reproduced by
NATIONAL TECHNICAL
INFORMATION SERVICE
US Department of Commerce
Springfield, VA. 22151

NOTICE

When Government drawings, specifications, or other data are used for any purpose other than in connection with a definitely related Government procurement operation, the United States Government thereby incurs no responsibility nor any obligation whatsoever; and the fact that the Government may have formulated, furnished, or in any way supplied the said drawings, specifications, or other data, is not to be regarded by implication or otherwise as in any manner licensing the holder or any other person or corporation, or conveying any rights or permission to manufacture, use, or sell any patented invention that may in any way be related thereto.

This report has been reviewed and cleared for open publication and/or public release by the appropriate Office of Information (OI) in accordance with AFR-190-17 and DODD 5230.9. There is no objection to unlimited distribution of this report to the public at large or by DDC to the National Technical Information Service (NTIS).

Copies of this report should not be returned unless return is required by security considerations, contractual obligations, or notice on a specific document.

This technical report has been reviewed and is approved for publication.

Charles L. Budde
CHARLES L. BUDDE, Capt. USAF
Project Monitor
Space and Missiles Branch
Systems Support Division
AF Materials Laboratory

FOR THE DIRECTOR

Henry E. Beck
HENRY E. BECK, Major, USAF
Chief, Space and Missiles Branch
Systems Support Division
AF Materials Laboratory

ACCESSION FOR	
NTIS	White Section <input checked="" type="checkbox"/>
DDC	Ball Section <input type="checkbox"/>
UNAN: CHICED	<input type="checkbox"/>
JUSTIFICATION	
BY	
DISTRIBUTION/AVAILABILITY CODES	
Dist.	ATL. and/or SPECIAL
At	

UNCLASSIFIED

SECURITY CLASSIFICATION OF THIS PAGE (When Data Entered)

REPORT DOCUMENTATION PAGE		READ INSTRUCTIONS BEFORE COMPLETING FORM
1 REPORT NUMBER AFML-TR-74-259	2 GOVT ACCESSION NO.	3 RECIPIENT'S CATALOG NUMBER AD-A010425
4 TITLE (and Subtitle) NONLINEAR DEFORMATION OF GRAPHITIC MATERIALS		5 TYPE OF REPORT & PERIOD COVERED FINAL TECHNICAL REPORT March 1973 to June 1974
		6 PERFORMING ORG. REPORT NUMBER none
7 AUTHOR(s) ROBERT M. JONES AND DUDLEY A.R. NELSON, JR.		8 CONTRACT OR GRANT NUMBER(s) AF F33615-73-C-5124
9 PERFORMING ORGANIZATION NAME AND ADDRESS CIVIL AND MECHANICAL ENGINEERING DEPARTMENT SOUTHERN METHODIST UNIVERSITY INSTITUTE OF TECHNOLOGY, DALLAS, TEXAS 75275		10 PROGRAM ELEMENT, PROJECT, TASK AREA & WORK UNIT NUMBERS 63311F 627A0009
11 CONTROLLING OFFICE NAME AND ADDRESS AIR FORCE MATERIALS LABORATORY/MXS WRIGHT-PATTERSON AFB, OHIO 45433		12 REPORT DATE February 1975
		13 NUMBER OF PAGES 162
14 MONITORING AGENCY NAME & ADDRESS (if different from Controlling Office)		15 SECURITY CLASS. (of this report) UNCLASSIFIED
		15a DECLASSIFICATION/DOWNGRADING SCHEDULE
16 DISTRIBUTION STATEMENT (of this Report) Approved for Public Release; Distribution Unlimited		
17 DISTRIBUTION STATEMENT (of the abstract entered in Block 20, if different from Report)		
18 SUPPLEMENTARY NOTES Reproduced by NATIONAL TECHNICAL INFORMATION SERVICE US Department of Commerce Springfield, VA 22151		
19 KEY WORDS (Continue on reverse side if necessary and identify by block number) Graphite, Composite Materials, Stress Analysis, Orthotropy, Material Modeling		
20 ABSTRACT (Continue on reverse side if necessary and identify by block number) Artificial graphites have been used for the past decade in reentry vehicle nosetips. Severe design requirements are imposed on nosetips because of their operational environment. Thus, accurate stress analysis procedures are of paramount importance. A new model for the deformation behavior of this group of nonlinear transversely isotropic materials under initial loading is described. This material model, which is based on a new deformation theory of orthotropic plasticity, has excellent potential for description of the unusual phenomenon (cont'd on back)		

DD FORM 1473
1 JAN 73

EDITION OF 1 NOV 65 IS OBSOLETE

UNCLASSIFIED

SECURITY CLASSIFICATION OF THIS PAGE (When Data Entered)

PRICES SUBJECT TO CHANGE

UNCLASSIFIED

SECURITY CLASSIFICATION OF THIS PAGE(When Data Entered)

(Block 20 - continued)

of "biaxial (multiaxial) softening" found in ATJ-S graphite. Biaxial softening is characterized by the development of larger strains in biaxial tension than in uniaxial tension, in contradiction to conventional Poisson effects. Moreover, another characteristic of graphite deformation behavior, different moduli in tension and compression, is accounted for. The model is examined for sensitivity to (1) a nonsymmetric compliance matrix, (2) how the material model constants are obtained, and (3) variations in material properties. Comparisons are made between strain values obtained with the material model incorporated in a finite element computer analysis and strain values measured in off-axis uniaxial tests and biaxial tests.

ii

UNCLASSIFIED

SECURITY CLASSIFICATION OF THIS PAGE(When Data Entered)

FOREWORD

This final report was submitted by Southern Methodist University, Institute of Technology, Dallas, Texas 75275 under USAF Contract F33615-73-C-5124, Job Order 627A0009. The work, a new nonlinear deformation material model for graphitic reentry vehicle nose tip materials, was performed for the Air Force Materials Laboratory, Wright-Patterson AFB, Ohio 45433. Captains Charles L. Budde and John R. Koenig (AFML/MXS) served as project engineers.

Dr. Robert M. Jones was the Principal Investigator. Mr. Dudley A. R. Nelson, Jr. was the Graduate Research Assistant. The extensive cooperation of Mr. Julius Jortner of McDonnell-Douglas Astronautics Company, Huntington Beach, California is sincerely appreciated.

Pages iv and v are Blank.

TABLE OF CONTENTS

LIST OF FIGURES	viii
LIST OF TABLES.	xi
NOMENCLATURE.	xii
1. INTRODUCTION	1
1.1 Material Nonlinearities	2
1.2 Different Moduli in Tension and Compression	6
1.3 Summary Remarks	11
2. NONLINEAR DEFORMATION MODEL.	13
2.1 General Description of Model Characteristics.	14
2.2 Effect of Material Model Constants.	21
2.3 Iteration and Convergence Studies	33
2.4 Sensitivity Studies	39
2.4.1 Symmetry of the Compliance Matrix.	39
2.4.2 Evaluation of Material Constants	41
2.4.3 Variation in Material Properties	43
3. ELASTIC MODELS FOR DIFFERENT MODULI IN TENSION AND COMPRESSION .	47
3.1 Introduction.	47
3.2 Weighted Compliance Model	50
3.3 Restricted Compliance Model	54
3.4 Summary	58
4. NONLINEAR DEFORMATION MODELS FOR DIFFERENT MODULI IN TENSION AND COMPRESSION.	60
4.1 Introduction.	60
4.2 Iteration Procedure for Material Models	64
4.3 Strain Energy Functions	68
4.4 Nonlinear Weighted Compliance Material Model.	70
4.5 Nonlinear Restricted Compliance Material Model.	74
4.6 Summary	76
5. COMPARISON OF PREDICTED AND MEASURED STRAIN RESPONSE UNDER UNIAXIAL OFF-AXIS LOADING.	78
5.1 Introduction.	78
5.2 Description of Test Specimens and Procedures.	78
5.3 Comparisons of Predicted and Measured Strain Response . . .	82
5.3.1 Material Properties.	82
5.3.2 Method of Presentation of Results.	82
5.3.3 Tensile Strain Correlations.	87
5.3.4 Compressive Strain Correlations for Nonlinear Weighted Compliance Model.	90

TABLE OF CONTENTS, continued

5.3.5	Compressive Strain Correlations for Nonlinear Restricted Compliance Model.	90
5.4	Summary	98
6.	COMPARISON OF PREDICTED AND MEASURED STRAIN RESPONSE UNDER BIAXIAL LOADING.	100
6.1	Introduction.	100
6.2	Room Temperature Strain Correlations.	101
6.2.1	Strain Correlations for Nonlinear Material Model Predictions.	103
6.2.2	Strain Correlations for Nonlinear Multimodulus Material Model Predictions with the 16K9 Data Base . .	109
6.2.3	Strain Correlations for Nonlinear Restricted Compliance Material Model Predictions with the ICO Data Base.	115
6.3	Fracture Strain Correlations.	122
6.4	2000°F Strain Correlations.	126
6.5	Summary	133
7.	CONCLUDING REMARKS	135
APPENDIX A	COMPARISON OF THE TOTAL STRAIN ENERGY APPROACH WITH THE DISTORTIONAL ENERGY APPROACH FOR ISOTROPIC MATERIALS . . .	142
REFERENCES.	147

LIST OF FIGURES

1. Graphite Billet Coordinate System.	3
2. Common Nosetip Geometries.	4
3. Biaxial Tensile Behavior of Graphite (ν decreasing).	5
4. Stress-Strain Curve for a Material with Different Moduli in Tension and Compression	7
5. Comparison of Actual Stress-Strain Behavior with the Bilinear Model	10
6. ATJ-S Graphite Stress-Strain Behavior.	15
7. Uniaxial Interpretation of the Strain Energy Function, U	17
8. Representation of Stress-Strain Behavior for Direct Moduli	20
9. Representation of S^+ -Strain Behavior for Poisson's Ratios.	20
10. Stress-Strain Behavior of Strain-Hardening Materials with Negative B	23
11. Schematic Behavior of Material Property Versus Strain Energy Curves for Various Values of A , B , C , and U_0	23
12. Material Property Versus Strain Energy Curves for $A=1$, $B=.05$, $U_0=1$, and $C=.1, .5, 1$, and 1.25	24
13. Material Property Versus Strain Energy Curves for $A=1$, $B=.5$, $U_0=1$, and $C=.1, .5, 1$, and 1.25	25
14. Normalized Stress-Strain Curves for $B=.05$ and $C=.1, .5, 1$, and 1.25	27
15. Normalized Stress-Strain Curves for $B=.5$ and $C=.1, .5, 1$, and 1.25	28
16. Uniqueness Versus Nonuniqueness of the Material Property - Energy Relationship	29
17. Effect of Material Constant B on the Stress-Strain Curve	31
18. Stress-Strain Response for Various Relative Magnitudes of B and C	32
19. Iteration Procedure.	34
20. Convergence of Iteration Procedure	35
21. One-Element Plane Stress Model	35
22. Approximation of Modulus-Energy Data with Material Property Equations	42

LIST OF FIGURES, continued

23. Interpretation of Percentage Deviations in Strains.	44
24. Variation of Material Properties.	45
25. Relation of Principal Stress (p-q- θ) Coordinates to Body and Principal Material (r-z- ϕ) Coordinates.	48
26. Positive and Negative Shear Stress at 45° to Principal Material Directions	57
27. Tensile Stress-Strain Behavior of Graphite.	61
28. Compressive Stress-Strain Behavior of Graphite.	61
29. Strain Profiles Under Increasing Stress Levels for a Material that Softens Under Tension and Hardens Under Compression.	62
30. Iteration Procedure for Nonlinear Multimodulus Materials.	65
31. Variation of Weighted Strain Energy	71
32. Principal Material (x, y, z) Directions Versus Load (x', y', z') Directions.	73
33. Relation of Test Specimen Slabs to Billet	79
34. Relation of Tension Specimens to Slab	79
35. Relation of Compression Specimens to Slab	79
36. Tension Bar Gage Section.	81
37. Compression Rod Gage Section.	81
38. Off-Axis Behavior-Tension, $\alpha=0^\circ$	86
39. Off-Axis Behavior-Tension, $\alpha=45^\circ$	86
40. Off-Axis Behavior-Tension, $\alpha=70^\circ$	88
41. Off-Axis Behavior-Tension, $\alpha=90^\circ$	88
42. Off-Axis Behavior-Compression, $\alpha=0^\circ$, WCM.	91
43. Off-Axis Behavior-Compression, $\alpha=45^\circ$, WCM	91
44. Off-Axis Behavior-Compression, $\alpha=70^\circ$, WCM	92
45. Off-Axis Behavior-Compression, $\alpha=90^\circ$, WCM	92
46. Off-Axis Behavior-Compression, $\alpha=0^\circ$, RCM, E_{zc}	94

LIST OF FIGURES, continued

47. Off-Axis Behavior-Compression, $\alpha=45^\circ$, RCM, ϵ_{zc}	94
48. Off-Axis Behavior-Compression, $\alpha=70^\circ$, RCM, ϵ_{zc}	95
49. Off-Axis Behavior-Compression, $\alpha=90^\circ$, RCM, ϵ_{zc}	95
50. Off-Axis Behavior-Compression, $\alpha=0^\circ$, RCM, ϵ_{rc}	96
51. Off-Axis Behavior-Compression, $\alpha=45^\circ$, RCM, ϵ_{rc}	96
52. Off-Axis Behavior-Compression, $\alpha=70^\circ$, RCM, ϵ_{rc}	97
53. Off-Axis Behavior-Compression, $\alpha=90^\circ$, RCM, ϵ_{rc}	97
54. Hollow Graphite Biaxial Test Specimen	102
55. Finite Element Model of Hollow Graphite Biaxial Test Specimen . .	104
56. Predicted and Measured Strains in a Hollow Graphite Biaxial Test Specimen - Room Temperature Nonlinear Material Model	105
57. Predicted and Measured Strains in a Hollow Graphite Biaxial Test Specimen - Room Temperature Nonlinear WCM Predictions - 16K9 Data Set	110
58. Predicted and Measured Strains in a Hollow Graphite Biaxial Test Specimen - Room Temperature Nonlinear RCM Predictions - 16K9 Data Set	114
59. Predicted and Measured Strains in a Hollow Graphite Biaxial Test Specimen - Room Temperature Nonlinear RCM Predictions - 1C0 Data Set.	117
60. Predicted and Measured Strains in a Hollow Graphite Biaxial Test Specimen - Room Temperature Fracture Results - Nonlinear WCM Predictions - 16K9 Data Set	124
61. Predicted and Measured Strains in a Hollow Graphite Biaxial Test Specimen - Room Temperature Fracture Results - Nonlinear RCM Predictions - 16K9 Data Set	125
62. Predicted and Measured Strains in a Hollow Graphite Biaxial Test Specimen - Nonlinear RCM Predictions - 2000°F Average Data Set.	130
63. Predicted and Measured Strains in a Hollow Graphite Biaxial Test Specimen - Nonlinear RCM Predictions - 2000°F Revised Data Set.	132
64. Distortional Versus Total Strain Energy	143
65. Prediction of G_{sec}	145

LIST OF TABLES

1. Composite Materials Tensile and Compressive Moduli Relationships . . .	8
2. Material Property Constants for the Young's Moduli of ATJ-S Graphite and 7075-T6 Aluminum.	21
3. Effect of Loading and Material Constants B and C on Convergence of the Iteration Procedure.	37
4. Baseline Values of Constants in Material Property Equations for Nonsymmetric Compliance Matrix Study	40
5. Strain Results for Nonsymmetric Compliance Matrix Study.	40
6. Deviations in Strains for Different Procedures for Determining Material Constants	44
7. Deviations in Strains for $\pm 10\%$ Variations in Material Properties . . .	46
8. Constants in Material Property Equations for 16K9 Billet Data Base at 70°F.	84
9. 1C0 Data Base at 70°F for Nonlinear Material Model	107
10. Percentage Deviations of Nonlinear RCM Strain Predictions from Measured Strains.	115
11. 1C0 Data Base at 70°F for Nonlinear RCM.	118
12. Percentage Deviations of Nonlinear RCM Strain Predictions from Measured Strains.	121
13. Fracture Stresses and Strains at 70°F from Billet 16K9-27 (Ref. 7, p. 52)	123
14. Percentage Deviations of Nonlinear RCM Strain Predictions (Weighted Energy Approach) from Fracture Strains	126
15. Average Data Base at 2000°F.	128
16. Revised Data Base at 2000°F.	131

NOMENCLATURE

A_i, B_i, C_i, U_{0i}	= constants in i^{th} material property equation [Eq. (5)]
E_r, E_z, E_θ	= Young's moduli in principal material directions
E'_{rz}	= Young's modulus at 45° to r and z directions
E_{sec}	= secant modulus
G_{rz}	= shear modulus in rz plane
n	= constant in energy weighting function [Eq. (29)]
r, z, θ	= radial, axial, and circumferential directions [Fig. 2]
U	= strain energy function [Eq. (4)]
x, y, z	= rectangular coordinates aligned with principal material directions
x', y', z'	= rectangular coordinates in nonprincipal material directions
α	= angle of orientation of off-axis tests
γ_{rz}	= shear strain in rz plane
$\epsilon_r, \epsilon_z, \epsilon_\theta$	= strains in principal material directions
$\epsilon_{x'}, \epsilon_{y'}, \epsilon_{z'}$	= strains in x', y', z' directions
ν_r, ν_θ, ν_z	= Poisson's ratios for principal material directions [Eq. (2)]
$\sigma_r, \sigma_z, \sigma_\theta, \tau_{rz}$	= axisymmetric stresses in principal material coordinates

Subscripts

c = compression

t = tension

w = weighted

Superscripts

mn = principal material coordinates

pq = principal stress coordinates

1. INTRODUCTION

Artificial graphites have been used for the past decade in reentry vehicle nosetips. Accurate stress analysis procedures are essential in the design of nosetips because of exacting performance requirements. A successful nosetip design must have, on one hand, enough material to avoid a burn-through failure due to ablation from aerodynamic heating. On the other hand, a nosetip cannot have so much material that a thermal stress-generated failure results due to high thermal gradients. The key element in any stress analysis is the stress-strain (constitutive) relationship or material model.

The stress analysis problems inherent to reentry vehicle nosetip design were discussed by Jones [1] in 1967 along with numerous specific problems by other authors in the same conference proceedings volume. Since then, nosetip stress analysis technology has been periodically reviewed. In 1970, results of the aborted Graphite Advanced Development Plan were summarized from a stress analysis and material modeling point of view [2]. Also, an extremely valuable interagency conference was held by the Atomic Energy Commission [3]. More recently, Schneider et al [4] described much of the current thermodynamic and elastic stress analysis procedures for reentry vehicle nosetips. Also, Jones and Koenig [5] discussed the material modeling characteristics necessary for stress analysis of reentry vehicle nosetips.

Graphites used for reentry vehicle nosetips are manufactured in cylindrical billets. In the billet compaction process, the more or less elliptically shaped highly anisotropic graphite particles tend to lie with their long axes perpendicular to the billet axis. Moreover, the particles are randomly oriented in planes perpendicular to the billet axis. The properties in the plane perpendicular to the billet axis are therefore isotropic. However, perpendicular to that plane, i.e., parallel to the billet axis, the properties are quite

different. Accordingly, ATJ-S graphite is a transversely isotropic material with its principal material directions aligned with the cylindrical coordinate system, r, z, θ , of the billet shown in Fig. 1. Reentry vehicle nosetips are made as axisymmetric bodies with the symmetry axis being the billet axis. Thus, the billet cylindrical coordinate system is also used for a nosetip.

Two common nosetip geometries, shell tips and plug tips, are shown in Fig. 2. The internal contour of the shell tip must be designed to have a wall thickness sufficient to satisfy the ablation requirements, but thin enough to avoid a thermal stress failure. For the plug tip, the exposed length of the plug, the shank diameter, and the interface angle between the plug and the surrounding heat shield material can be varied to obtain a plug tip that can survive a trajectory from a thermal stress versus ablation point of view. For both nosetip geometries, the thermal and mechanical stresses and strains cannot be predicted to the accuracy required to obtain the desired design confidence by using previously available material models.

1.1 MATERIAL NONLINEARITIES

A new phenomenon known as "biaxial (multiaxial) softening" was found in tests of ATJ-S graphite [5-9]. Biaxial softening is characterized by the development of slightly larger strains in biaxial tension than in uniaxial tension, as shown in Fig. 3, in contradiction to what might be anticipated on the basis of conventional Poisson effects. This phenomenon is attributed to plastic volume changes resulting from internal tearing or microcracking. Other distinguishing characteristics of graphites, which render them more difficult to theoretically model than most metals, are transversely isotropic nonlinear stress-strain behavior; different tensile and compressive stiffnesses and strengths; and unloading behavior which is dependent on stress level. Thus, the usual concepts of classical plasticity are not applicable to graphites.

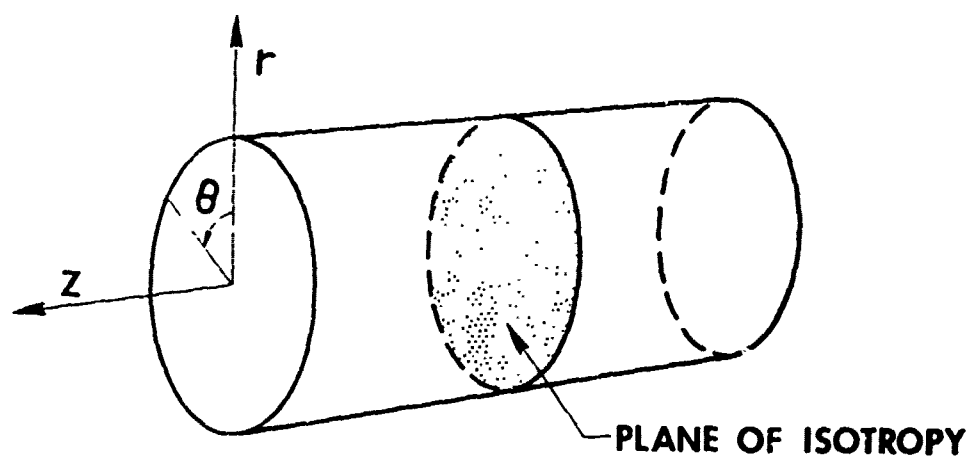
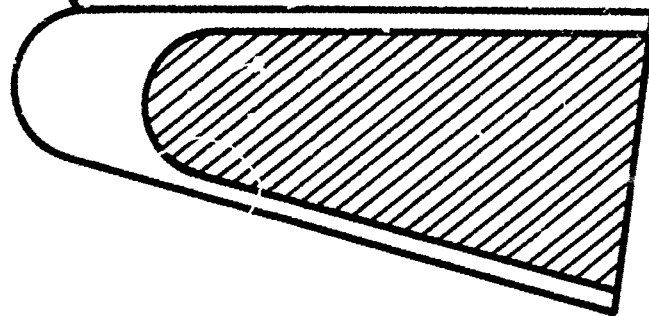


FIGURE 1 GRAPHITE BILLET COORDINATE SYSTEM

SHELL NOSETIP



PLUG NOSETIP

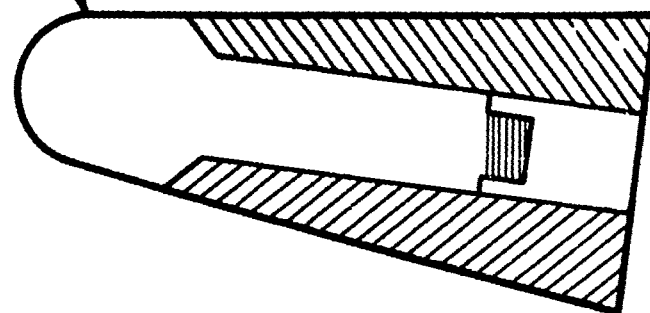


FIGURE 2 COMMON NOSETIP GEOMETRIES

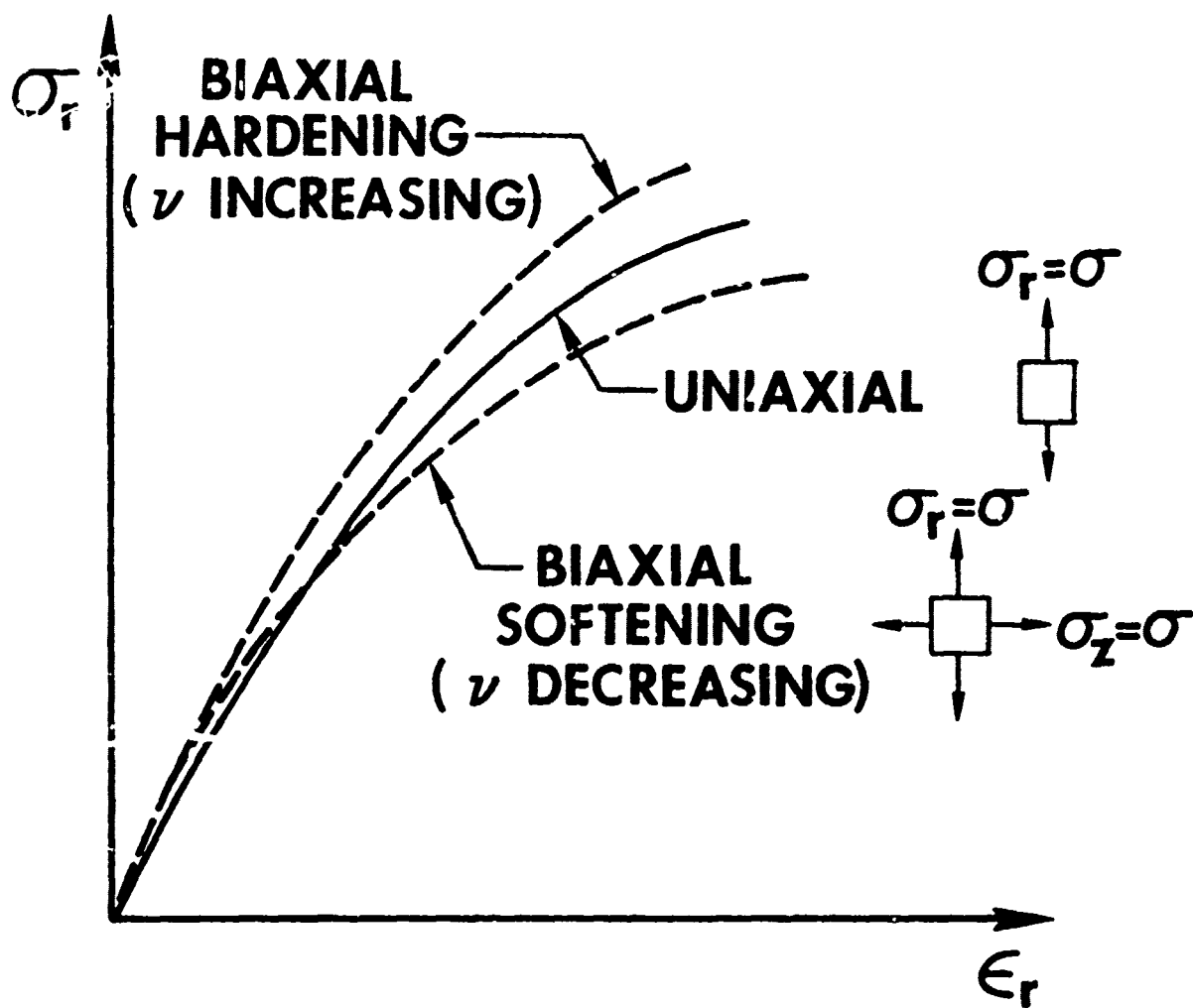


FIGURE 3 BIAxIAL TENSILE BEHAVIOR OF GRAPHITE (ν DECREASING)

1.2 DIFFERENT MODULI IN TENSION AND COMPRESSION

A significant characteristic of graphites is their different behavior under tensile and compressive loads. Both the elastic moduli (stiffnesses) and the strengths in principal material property directions of these orthotropic materials are different for tensile loading than for compressive loading. This characteristic behavior is shown schematically in the stress-strain curve of Figure 4. This phenomenon is but one of several differences that make composite materials more difficult to analyze (and hence design) than the more common structural materials such as aluminum.

Both fiber-reinforced and granular composite materials have different moduli in tension and compression as displayed in Table 1. Unidirectional glass fibers in an epoxy matrix have compressive moduli 20% lower than the tensile moduli [10]. For some unidirectional boron/epoxy fiber-reinforced laminae, the compressive moduli are about 15-20% larger than the tensile moduli [11]. In contrast, some unidirectional graphite/epoxy fiber-reinforced laminae have tensile moduli up to 40% greater than the compressive moduli [11]. Other fiber-reinforced composites such as carbon/carbon have tensile moduli from two to five times the compressive moduli [12]. Thus, no clear pattern of larger tensile than compressive moduli or vice versa exists for fiber-reinforced composite materials. A plausible physical explanation for this puzzling circumstance has yet to be made.

For granular composite materials, the picture is no clearer. ZTA graphite has tensile moduli as much as 20% lower than the compressive moduli [13]. On the other hand, ATJ-S graphite has tensile moduli as much as 20% more than the compressive moduli [14].

Many other materials have different tensile and compressive moduli. Which modulus is higher may depend on the fiber or granule stiffness relative to the

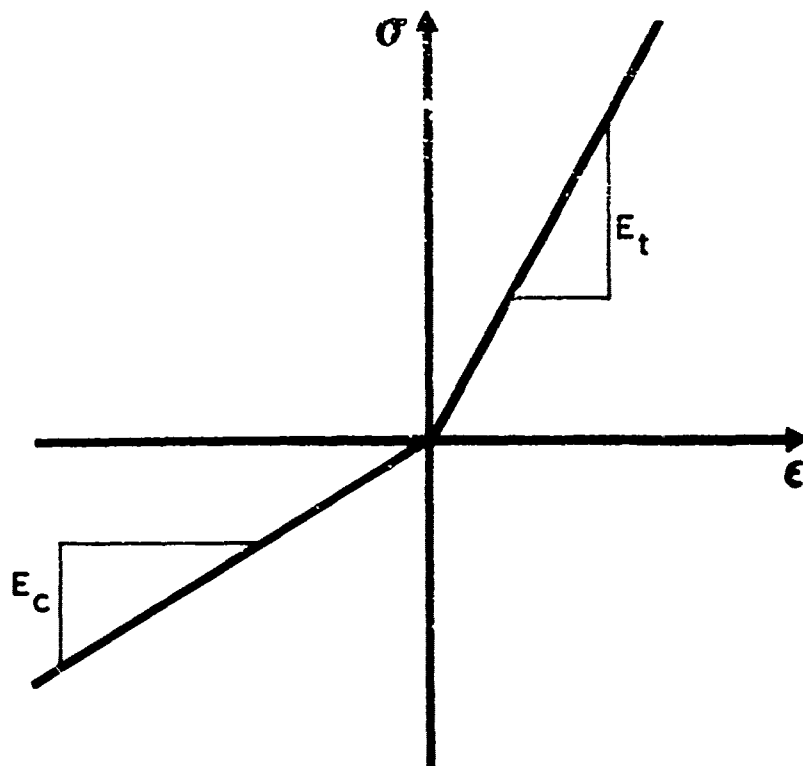


FIGURE 4 STRESS-STRAIN CURVE FOR A MATERIAL WITH DIFFERENT MODULI IN TENSION AND COMPRESSION

TABLE 1
COMPOSITE MATERIALS TENSILE AND COMPRESSIVE MODULI RELATIONSHIPS

MATERIAL	FIBEROUS OR GRANULAR	REPRESENTATIVE MODULI RELATIONSHIP
GLASS/EPOXY	FIBEROUS	$E_t = 1.25E_c$
BORON/EPOXY	FIBEROUS	$E_c = 1.2E_t$
GRAPHITE/EPOXY	FIBEROUS	$E_t = 1.4E_c$
CARBON/CARBON	FIBEROUS	$E_t = 2-5E_c$
ZTA GRAPHITE	GRANULAR	$E_c = 1.25E_t$
ATJ-S GRAPHITE	GRANULAR	$E_t = 1.2E_c$

matrix stiffness. Such a relationship would influence whether the fibers or granules tend to contact and hence stiffen the composite. A general physical explanation of the reasons for different behavior in tension and compression is not yet available. Investigation of the micromechanical behavioral aspects of composite materials may lead to a rational explanation of this phenomenon. Until such an explanation is available, the apparent behavior can be used in analyzing the stress-strain behavior of materials. That is, even without knowing why the materials behave as they do, we can model their apparent behavior.

Actual stress-strain behavior is probably not as simple as shown in Fig. 4. Instead, a nonlinear transition region may exist between the tensile and compressive linear portions of the stress-strain curve [15]. The measurement of strains near zero stress is difficult to perform accurately, but the stress-strain behavior might be as shown in Figure 5 wherein replacement of the actual behavior by a bilinear model is offered as a simplification of obviously nonlinear behavior. For most materials, the mechanical property data is not sufficient to justify use of a more complex material model. A possible disadvantage of bilinear stress-strain curve approximation is the discontinuity in slope (modulus) at the origin of the stress-strain curve.

Given that the uniaxial stress-strain behavior is approximated by a bilinear representation, the definition remains of the actual multiaxial stress-strain, or constitutive, relations that are required in structural analysis. Over the past ten years, Ambartsumyan and his co-workers, [References 16 to 19], in the process of obtaining solutions for stress analysis of shells and bodies of revolution, defined a set of stress-strain relations that will be referred to herein as the Ambartsumyan material model. Jones [20] applied the model to the problem of buckling under biaxial loading of circular cylindrical shells made of an isotropic material. However, in application of the Ambartsumyan

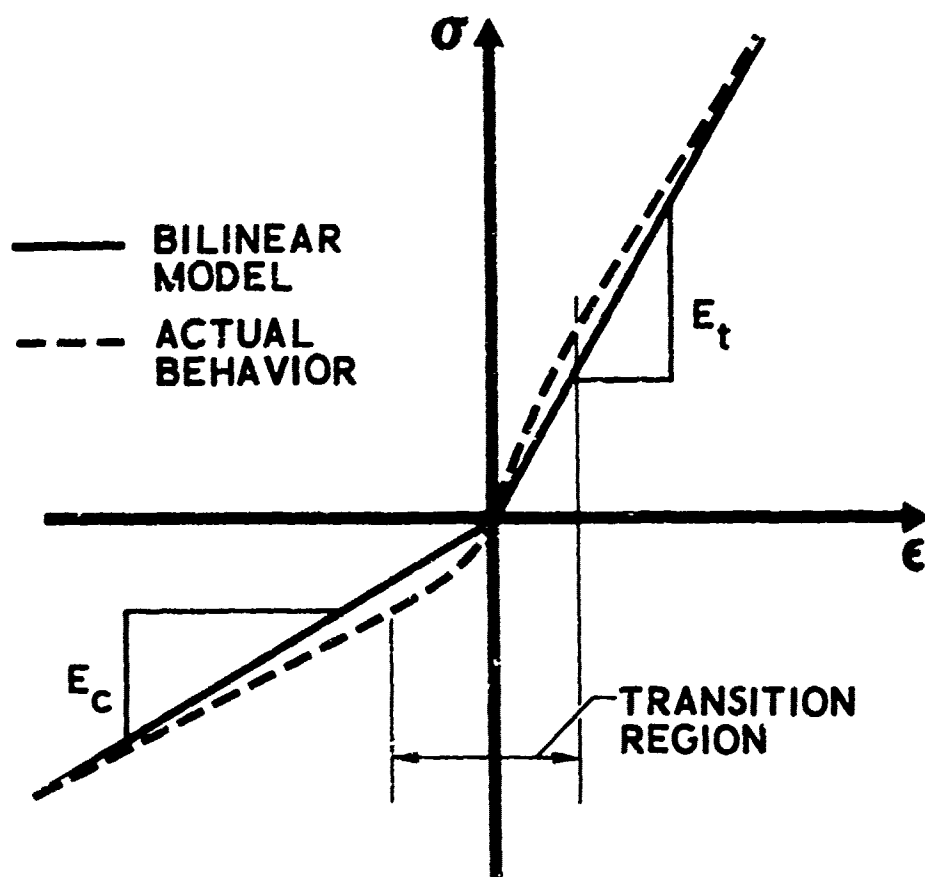


FIGURE 5 COMPARISON OF ACTUAL STRESS-STRAIN BEHAVIOR WITH THE BILINEAR MODEL

material model to orthotropic materials, certain deficiencies, such as a non-symmetric compliance matrix in the stress-strain relations, are apparent.

Jones [22] also applied modified bilinear stress-strain relations to the buckling of shells with multiple layers of orthotropic material with different moduli in tension and compression. His modifications consisted of weighting tensile and compressive compliances according to the proportions of the principal stresses in order to obtain a symmetric compliance matrix. Isabekian and Khachatryan [23] made the Ambartsumyan material model compliance matrix symmetric just by enforcing certain relations between the material properties. Their relations are part of the basis for the present report.

1.3 SUMMARY REMARKS

In this report, a new material model is presented for the initial loading behavior of graphites. This inherently simple material model, which is based on a new deformation theory of orthotropic plasticity, has excellent potential for the description of the biaxial softening phenomenon. A pragmatic engineering approach is used to analyze an important problem that has thus far not been amenable to solution by classical plasticity approaches. The model is particularly applicable to materials for which a finite plastic volume change is exhibited; i.e., the usual restriction of plasticity theories to zero plastic volume change is discarded. The model is examined for sensitivity to (1) a nonsymmetric compliance matrix, (2) how the material model constants are obtained, and (3) variations in material properties. Finally, favorable comparisons are made between predicted strain values obtained with the new material model incorporated in the SAAS III finite element computer program [24] and experimental strain values from biaxial tests conducted by Jortner [6-9].

This report is divided into several parts: nonlinear deformation model,

different moduli in tension and compression elastic model, nonlinear deformation model for materials with different moduli in tension and compression, comparison of predicted and measured off-axis uniaxial response, and comparison of predicted and measured biaxial strain response. This approach is taken to build up the final comprehensive model by examining the individual facets of the parts of the model separately. We therefore are able to assimilate the basic concepts of the final model in a palatable piecemeal fashion.

2. NONLINEAR DEFORMATION MODEL

Current material models are not adequate for prediction of multiaxial nonlinear stress-strain response of graphitic materials. Thus, a new material model will be formulated in the following sections. The general characteristics of the new model are described in Section 2.1. The effect of the constants in the new material model is determined in Section 2.2. Iteration and convergence of the material model to actual nonlinear stress-strain behavior is demonstrated in Section 2.3. Finally, the sensitivity of the model to nonsymmetry of the compliance matrix, the values of the material constants, and inherent material property data scatter is discussed in Section 2.4.

First, however, the graphite material model due to Weng [25,26] will be described. He uses a deformation theory of plasticity approach to develop a generalized nonlinear stress-strain relation for a class of bodies made of transversely isotropic materials. Two important assumptions are made in his formulation in addition to the restriction to monotonically increasing proportional loads. The first assumption is that the deformations do not alter the degree or direction of the anisotropy of the material. The implications and validity of this assumption for artificial graphites will be explored further in Section 2.4. The second assumption is that the shape of the nonlinear stress-strain curves is identical for all stress components. Consequently, the Poisson's ratios in Weng's model are constant for all deformation levels. Weng's generalized stress-strain relation for an anisotropic material is

$$\epsilon_i = \sum_{j=1}^6 S_{ij} \sigma_j \phi \quad i = 1, 2, \dots, 6 \quad (1)$$

where nonlinear effects are introduced through the variable proportionality function, ϕ . In addition, ϵ_i = strain components, S_{ij} = compliances, and σ_j = stress components. The function ϕ is the effective strain divided by the effective stress and is obtained by curve-fitting both uniaxial and biaxial experi-

mental data. However, for nonisotropic materials, no physically meaningful definition exists for effective stress and effective strain.

For artificial graphites, the normal stress - normal strain curves are similar, but not identical, in shape (see Fig. 6). Also, the Poisson's ratios are not always constant; they can decrease substantially due to microcracking related to the biaxial softening phenomenon. Accordingly, Weng's model cannot be used to obtain engineering correlation between theory and experiment.

2.1 GENERAL DESCRIPTION OF MATERIAL MODEL CHARACTERISTICS

In the new material model, Weng's assumption of identically shaped stress-strain curves is discarded as is his restriction to constant Poisson's ratios. One objective of this research is to incorporate the new material model in the finite element stress analysis computer program SAAS III [24]. For that program, the most general case that can be analyzed is the axisymmetric deformation of an axisymmetric body made of a nonlinear orthotropic material and loaded in an axisymmetric manner. Consequently, the new material model is discussed for this case. Of course, the concept of the model is applicable to more general loading and deformation, as well as more general materials.

The orthotropic stress-strain relations for an axisymmetric elastic body under axisymmetric load are:

$$\begin{Bmatrix} \epsilon_r \\ \epsilon_z \\ \epsilon_\theta \\ \gamma_{rz} \end{Bmatrix} = \begin{bmatrix} \frac{1}{E_r} & -\frac{\nu_{rz}}{E_r} & -\frac{\nu_{r\theta}}{E_r} & 0 \\ -\frac{\nu_{rz}}{E_r} & \frac{1}{E_z} & -\frac{\nu_{z\theta}}{E_z} & 0 \\ \frac{\nu_{r\theta}}{E_r} & -\frac{\nu_{r\theta}}{E_z} & \frac{1}{E_\theta} & 0 \\ 0 & 0 & 0 & \frac{1}{G_{rz}} \end{bmatrix} \begin{Bmatrix} \sigma_r \\ \sigma_z \\ \sigma_\theta \\ \tau_{rz} \end{Bmatrix} \quad (2)$$

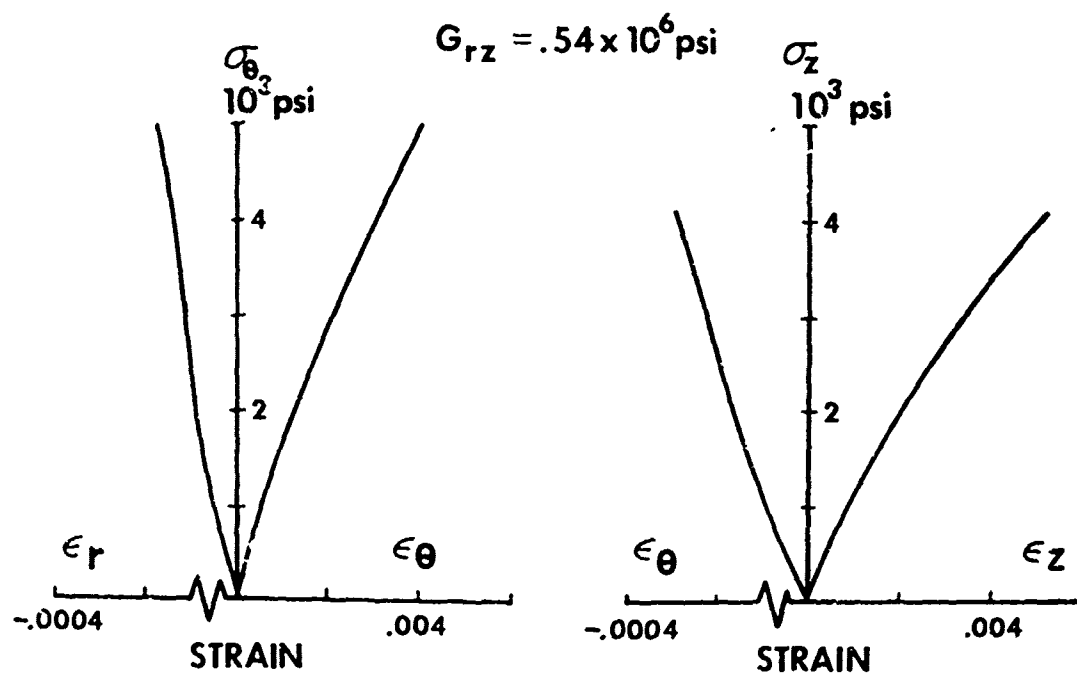


FIGURE 6 ATJ-S GRAPHITE STRESS-STRAIN BEHAVIOR

Directions denoted by the subscripts r , z , and θ are principal material directions. The elastic material constants in the compliance matrix of Eq. (2) are

E_r = Young's modulus in the r direction

E_z = Young's modulus in the z direction

E_θ = Young's modulus in the θ direction

$\nu_{rz} = -\epsilon_z/\epsilon_r$ for the loading $\sigma_r = \sigma$ (all other stresses zero)

$\nu_{r\theta} = -\epsilon_\theta/\epsilon_r$ for the loading $\sigma_r = \sigma$ (all other stresses zero)

$\nu_{z\theta} = -\epsilon_\theta/\epsilon_z$ for the loading $\sigma_z = \sigma$ (all other stresses zero)

G_{rz} = Shear modulus in the rz plane

The reciprocal relations of orthotropic elasticity

$$\nu_{rz}/E_r = \nu_{zr}/E_z, \nu_{r\theta}/E_r = \nu_{\theta r}/E_\theta, \nu_{z\theta}/E_z = \nu_{\theta z}/E_\theta \quad (3)$$

can be used to express alternative definitions for the Poisson's ratios in terms of the seven independent elastic constants.

In the present material model, the seven independent material properties are allowed to vary (independently) with the state of stress and strain. (In contrast, Weng introduced nonlinear effects by using a single proportionality function, ϕ .) In order to relate the material properties to a multiaxial stress state, the energy function,

$$U = (\sigma_r \epsilon_r + \sigma_z \epsilon_z + \sigma_\theta \epsilon_\theta + \tau_{rz} \gamma_{rz})/2 \quad (4)$$

is used. This function is half the function used by Weng in his material model for graphites. Since unloading is not considered, the distinction between inelasticity and nonlinear elasticity is not relevant at this point. Consequently, the right-hand side of Eq. (4) corresponds to the strain energy of the equivalent linear elastic system at each stage of deformation in a deformation theory of plasticity. The composition of U for a uniaxial loading case ($\sigma_x = \sigma$ and all other stresses zero) is depicted in Fig. 7. Two important points

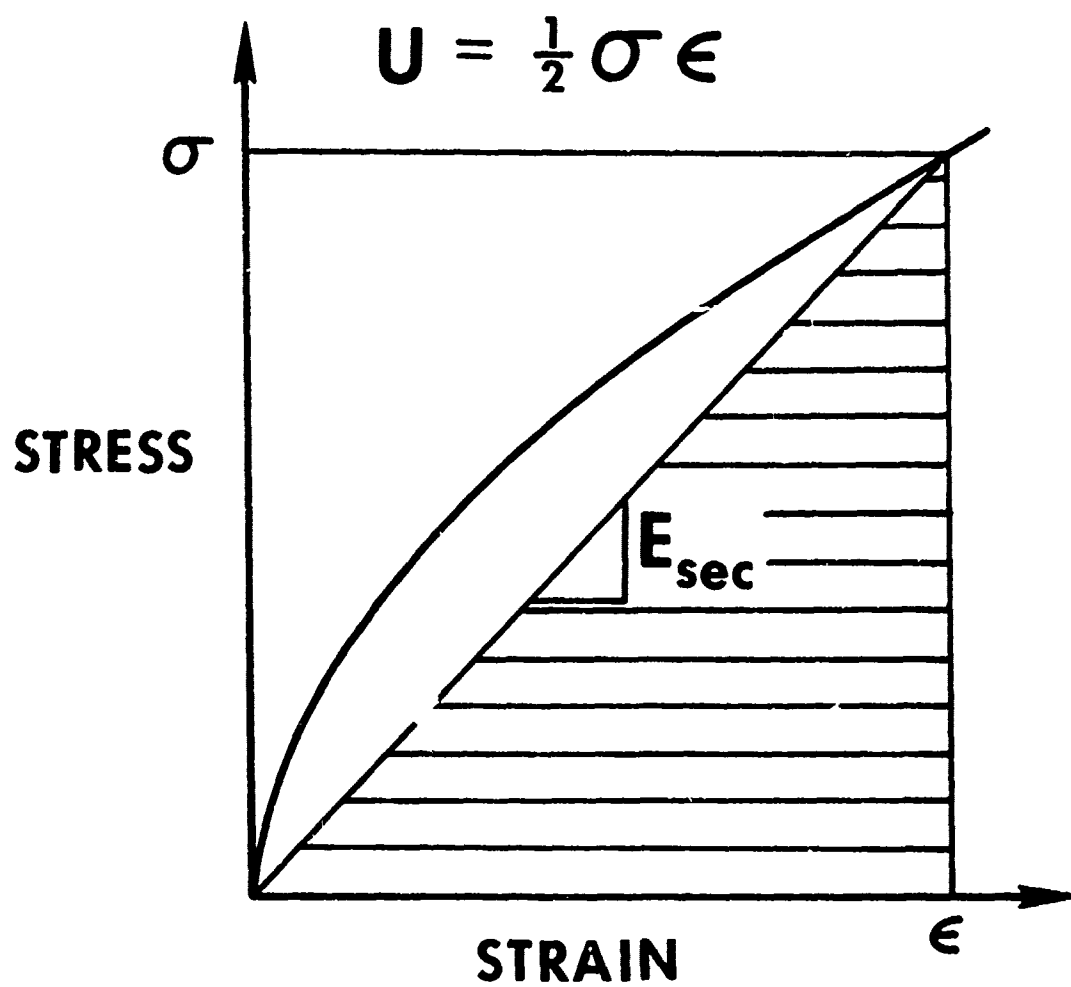


FIGURE 7 UNIAXIAL INTERPRETATION OF THE STRAIN ENERGY FUNCTION, U

should be noted about the function U : (1) it is a scalar and (2) its value depends only on the final state of stress and strain, not on the manner by which these states were reached [27]. Thus, in a computer program, the strain energy U is found by the multiplication of the eight values in Eq. (4) rather than numerical integration of the stress-strain histories representing the strain energy density or the complementary energy density.

In the present approach, equations are developed to relate the material properties to the strain energy U . As long as the material property changes monotonically (increasing or decreasing) for increasing values of the strain energy, a unique relationship for the properties in terms of U does exist. Material properties-versus- U curves can be obtained from uniaxial stress-strain data for the material and are approximated by

$$\text{Material Property}_i = A_i \left[1 - B_i (U/U_{0i})^{C_i} \right] \quad (5)$$

where i is the numerical designation of the specific material property. Equation (5) can be fit to all material property-versus- U curves quite effectively for ATJ-S graphite and should be flexible enough to represent many other engineering materials. Although more general, Eq. (5) is similar in form to the well-known Ramberg-Osgood stress-strain relation [28].

The constant A in Eq. (5) is the initial (elastic) value for the property. Thus, the dimensions of the material property are reflected in the dimensions of A . The constant U_0 is included in Eq. (5) to establish a dimensionless ratio and, thus, a dimensionally correct equation independent of the value of C . Both U_0 and U have the dimensions of energy density (stress). The numerical value of U_0 is arbitrary and is selected before the values of B and C are determined.

Constants B and C in Eq. (5) are dimensionless; their numerical values can be determined by at least two different approaches. First a least squares fit

(regression analysis) approach can be used. A second simpler technique is to solve simultaneously for the two constants using data at only three points on the property-versus- U curve. Since the value of U can be larger under multi-axial loading than under uniaxial loading, the material property equations are often extrapolated for multi-axial cases. For this reason, the second approach is recommended. The three points can easily be selected to prejudice the material property equation toward a better representation of the material property-versus- U curve at large values of U . Thus, difficulties that would otherwise arise under extrapolation are avoided.

Typical material property curves for ATJ-S graphite are shown in Figure 6. Schematics of those curves and associated material property equations for a modulus and a Poisson's ratio are shown in Figures 8 and 9, respectively. The type of uniaxial stress-strain data required to define the material property equations is also shown in these figures. Secant moduli are used when the stress-strain curve ceases to be linear.

The new material model with material properties defined in Eq. (5) was incorporated in the SAAS III program. Therefore, for an orthotropic material, the constants A_i , B_i , C_i and U_{0i} are input to the program for the seven independent material properties. If the degree of anisotropy of the material is less than orthotropic, e.g., transversely isotropic or isotropic, fewer constants (5 sets for transverse isotropy and 2 sets for isotropy) are necessary. In SAAS III, a maximum of six material types are permitted. Each material can have properties specified at a maximum of twelve temperatures. Thus, the number of sets of required constants is a function of the number of materials, the anisotropy of each material, and the number of temperatures at which properties are specified for each material.

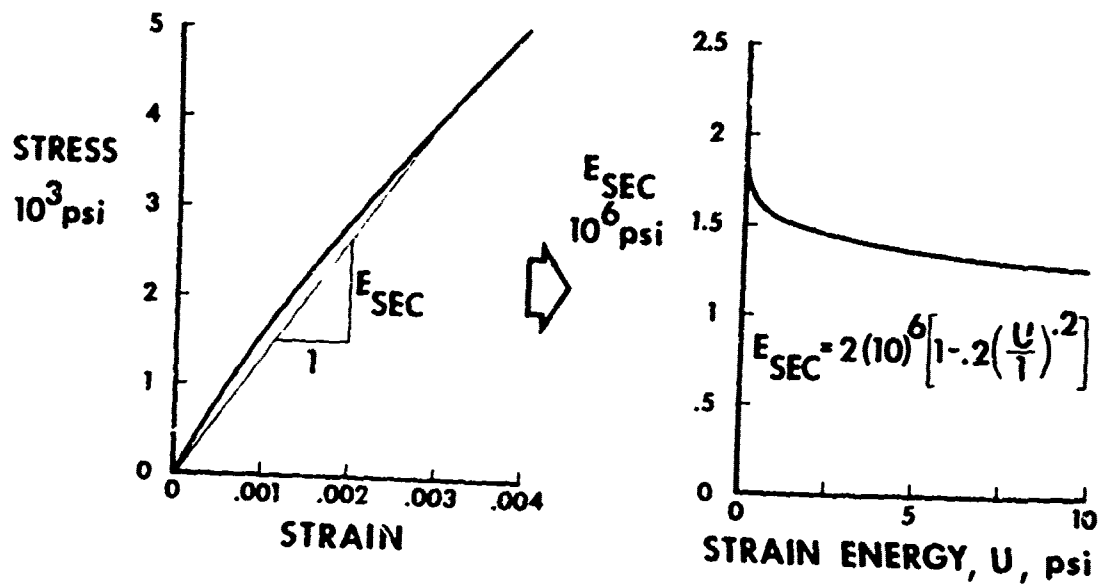


FIGURE 8 REPRESENTATION OF STRESS-STRAIN BEHAVIOR FOR DIRECT MODULI

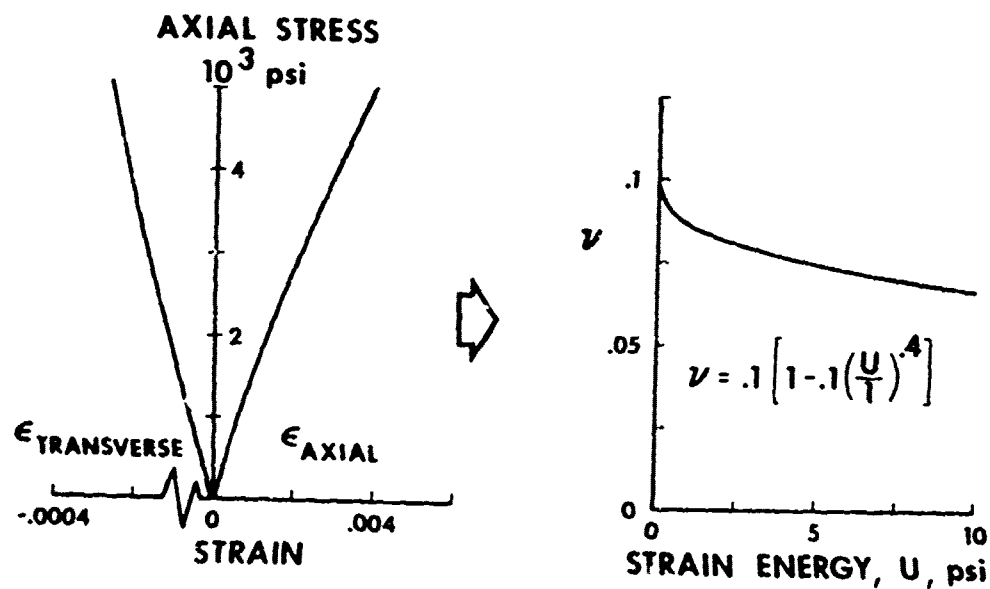


FIGURE 9 REPRESENTATION OF STRESS-STRAIN BEHAVIOR FOR POISSON'S RATIOS

2.2 EFFECT OF MATERIAL MODEL CONSTANTS

The general shapes of the material property-versus- U curves for different values of the constants A_i , B_i , and C_i are discussed in this section.

The material model constant A_i is used to define the initial slope (elastic value) of the property. Thus, the effect of A_i on the shape of the material property-versus- U curve can easily be appreciated. For Young's moduli, values of A are always positive to guarantee a positive strain energy density. For Poisson's ratios, values of A can be either positive or negative because ν can have either sign (for isotropic materials, $-1 < \nu < 1/2$; more complicated bounds are given by Lempriere [29] for orthotropic materials). The influence of the material constants B_i and C_i and their allowable range of magnitude is less obvious. Values of the material property constants used for Young's moduli for ATJ-S graphite and 7075-T6 aluminum are given in Table 2. In general, the values of the material property constants B_i and C_i each range between .05 and .5 for both the Young's moduli and Poisson's ratios of ATJ-S graphite. A short study was made to evaluate the effects of B_i and C_i on the shape of the material property-versus-strain energy density curve and consequently on the implied stress-strain behavior. Hereafter, B_i and C_i are abbreviated as B and C , respectively.

Table 2 Material Property Constants for the Young's Moduli
of ATJ-S Graphite and 7075-T6 Aluminum

MATERIAL	A	B	C	U_0
ATJ-S Graphite (E_z)	1.235×10^6 psi	.204557	.293684	1 psi
7075-T6 Aluminum (E)	10.5×10^6 psi	2.20069×10^{-4}	1.20274	1 psi

Before the detailed results of the study of the material property constants B and C are discussed, several general comments are appropriate. Only positive values of C are considered to be significant for describing material property behavior. A negative or zero value of C would not yield an "elastic" value of material property when the strain energy density approaches zero. Although negative values of B have not been used for ATJ-S graphite, they can be used in the description of Young's moduli for strain-hardening materials, i.e., concave upward stress-strain curves as in Fig. 10. Negative values of B can also be used in the approximation of Poisson's ratios for engineering metals such as aluminum and steel. For these metals, Poisson's ratios increases as the strain energy density increases.

The schematic behavior of material property-versus-strain energy density curves for various values of the material property constants A, B, C, and U_0 is shown in Fig. 11. As seen in Fig. 11 and demonstrated from the equations, the family of curves is coincident at a strain energy density value of U_0 ($U/U_0 = 1$). The magnitude of B determines the ordinate of this intersection. In the schematic, the curves drawn are typical of those for values $0 \leq B < 1$ (also shown in Fig. 11 is the straight line corresponding to the trivial case of $B=0$ and $0 < C < \infty$). The material property - strain energy relationship is linear for $C=1$. For positive values of C less than unity, all curves are concave downward. Specific examples of material property-versus-strain energy density curves for values of B of .05 and .5 are given in Figs. 12 and 13, respectively. The curves in both figures are $A = 1$ and $U_0 = 1$. At each B value, curves are given for four values of C: .1, .5, 1, and 1.25. Although no specific dimensions are associated with the material property constants in this study, several comments concerning their usual dimensions are appropriate.

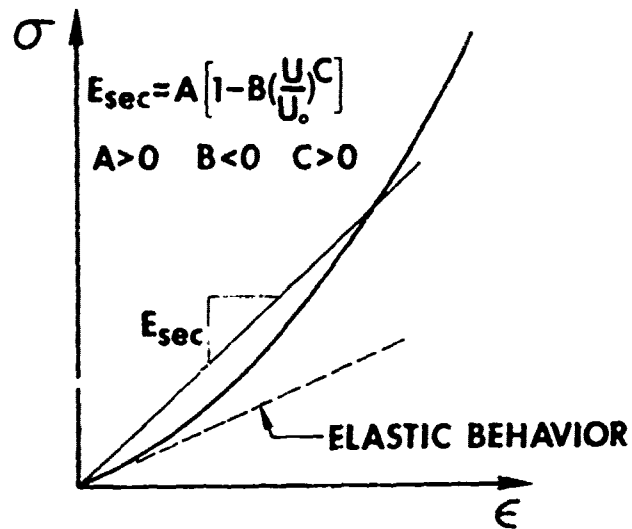


FIGURE 10 STRESS-STRAIN BEHAVIOR OF STRAIN-HARDENING MATERIALS WITH NEGATIVE B

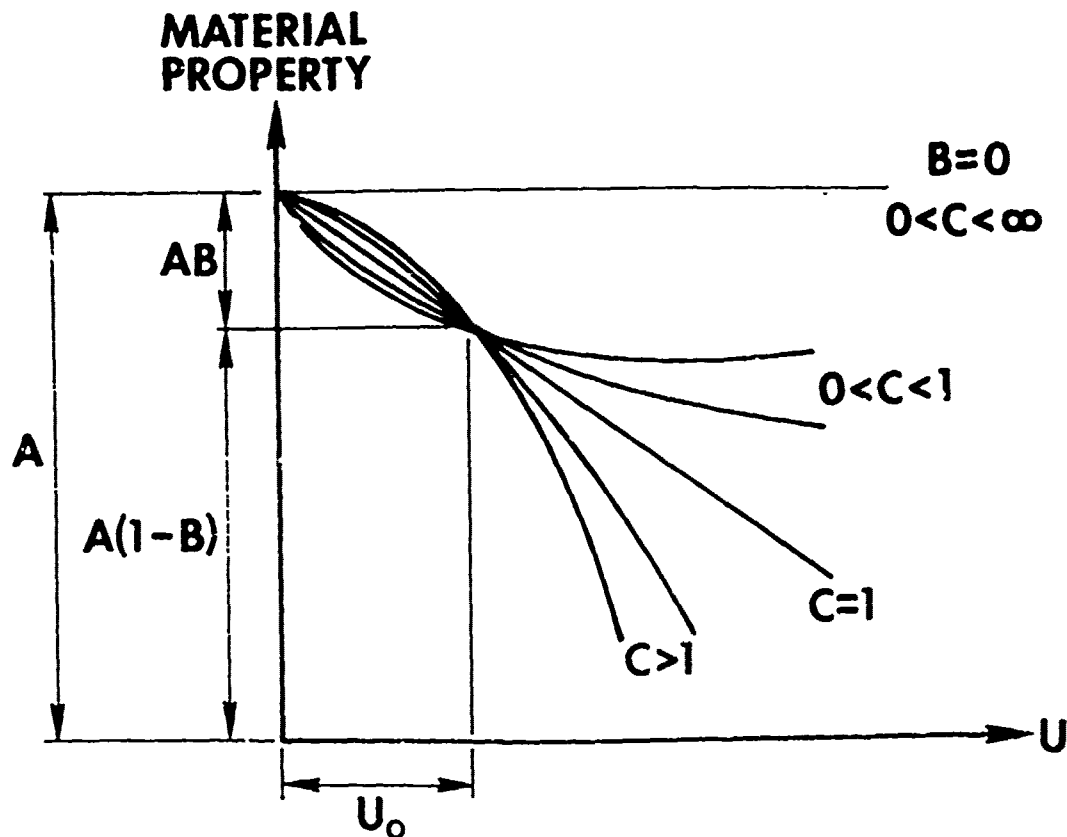


FIGURE 11 SCHEMATIC BEHAVIOR OF MATERIAL PROPERTY VERSUS STRAIN ENERGY CURVES FOR VARIOUS VALUES OF A, B, C, AND U_0

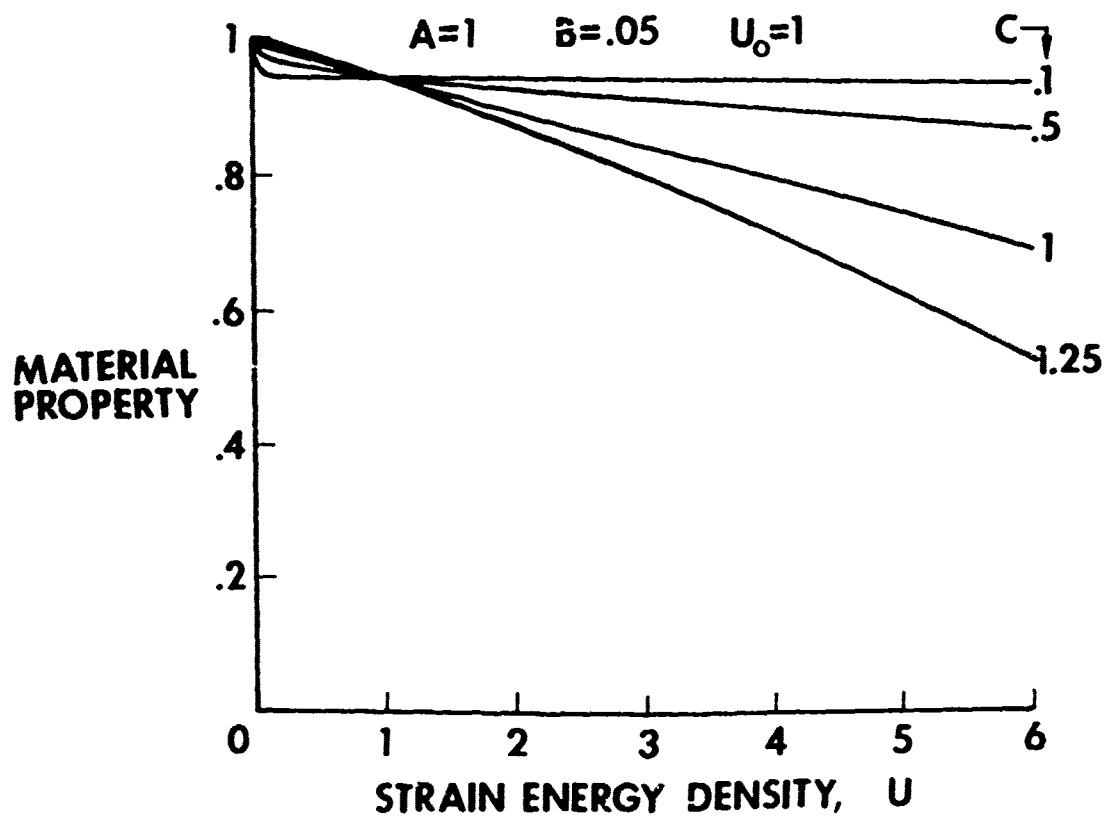


FIGURE 12 MATERIAL PROPERTY VERSUS STRAIN ENERGY CURVES FOR $A=1$, $B=.05$, $U_0=1$, AND $C=.1, .5, 1$, AND 1.25

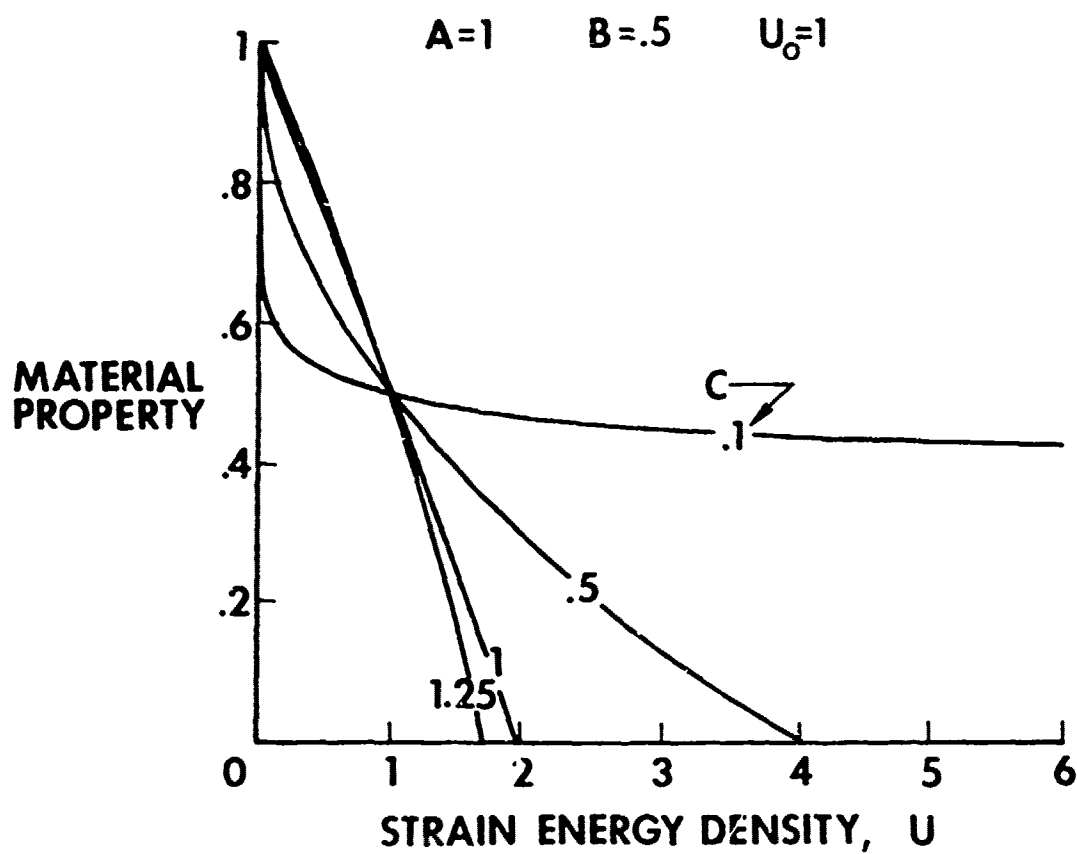


FIGURE 13 MATERIAL PROPERTY VERSUS STRAIN ENERGY CURVES
FOR $A=1$, $B=.5$, $U_0=1$, AND $C=1, .5, 1$, AND 1.25

The dimensions of the material property are reflected in the dimensions of A . For example, for Young's moduli, A could have dimensions of pounds per square inch (psi) or Newtons per square meter (N/m^2). For Poisson's ratios, A is dimensionless. The constant U_0 is included in Eq. 5 to establish a dimensionless ratio and, thus, a dimensionally correct equation independent of the value of C . Both U_0 and U have the dimensions of energy density (stress). Constants B and C are always dimensionless.

For a given direct modulus equation, the shape of the corresponding stress-strain curve can be determined. The results for $C = .1, .5, 1$ and 1.25 are presented in Fig. 14 for $B = .05$ and in Fig. 15 for $B = .5$. These curves are in a normalized form ($A = 1$ and $U_0 = 1$). The curves in Figs. 14 and 15 are coincident at the point corresponding to a strain energy density of U_0 ($U/U_0 = 1$). Also demonstrated in the figures, especially in Fig. 15, is the tendency for the stress-strain curves to approach a straight line with slope $A(1-B)$ as C approaches zero from the positive side. When C is large, the implied stress may not be monotonically increasing as a function of strain as in Fig. 16(a). Instead, the stress level may decrease with increasing strain after attaining a maximum value as in Fig. 16(b) or the curve for $C = 1.25$ in Fig. 15. The present material model cannot be used to represent the stress-strain curve in Fig. 16(b) if the value of U is the same at any two (different) stress levels, i.e., the material property-strain energy density curve must be unique. The present material model is therefore not suitable for large strain applications where the material property- U relationship is not unique. As will be discussed later, large value of C may also lead to convergence difficulties in the material model.

The direct modulus case is examined to evaluate the effects of the relative magnitudes of material property constants B and C on the general shape of

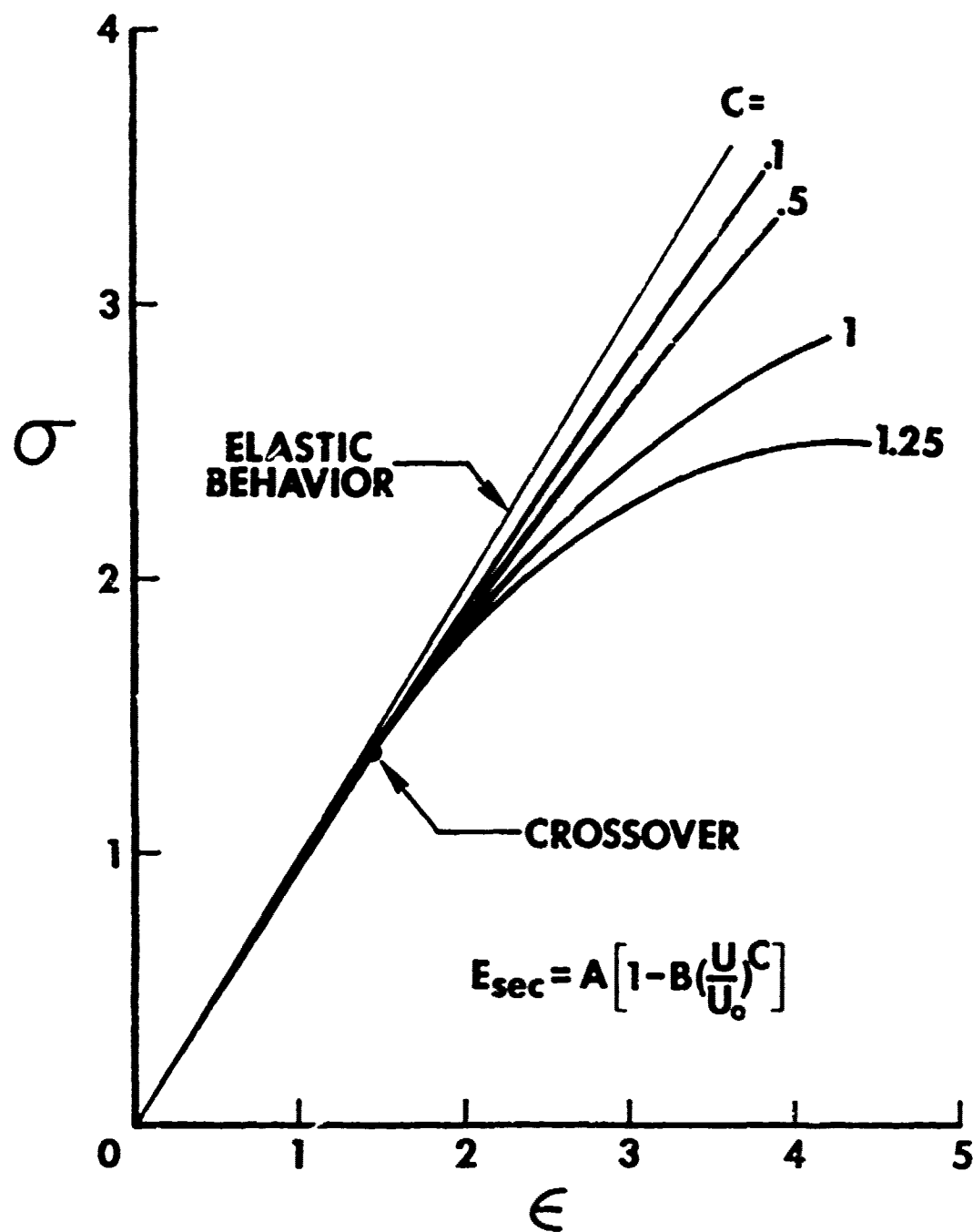


FIGURE 14 NORMALIZED STRESS-STRAIN CURVES FOR $B=.05$ AND $C=.1, .5, 1$, AND 1.25

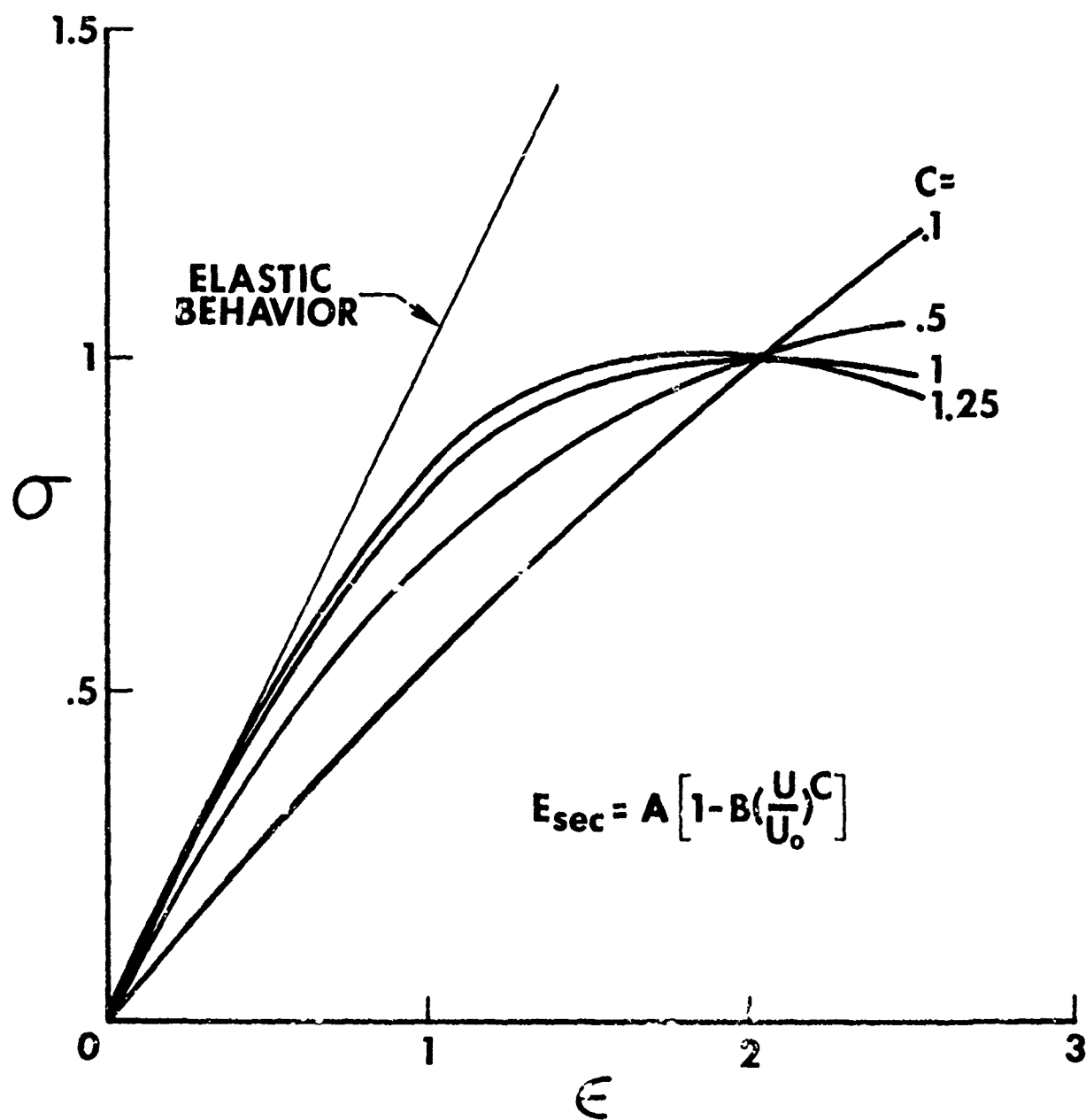


FIGURE 15 NORMALIZED STRESS-STRAIN CURVES FOR $B=.5$ AND $C=.1, .5, 1$, AND 1.25

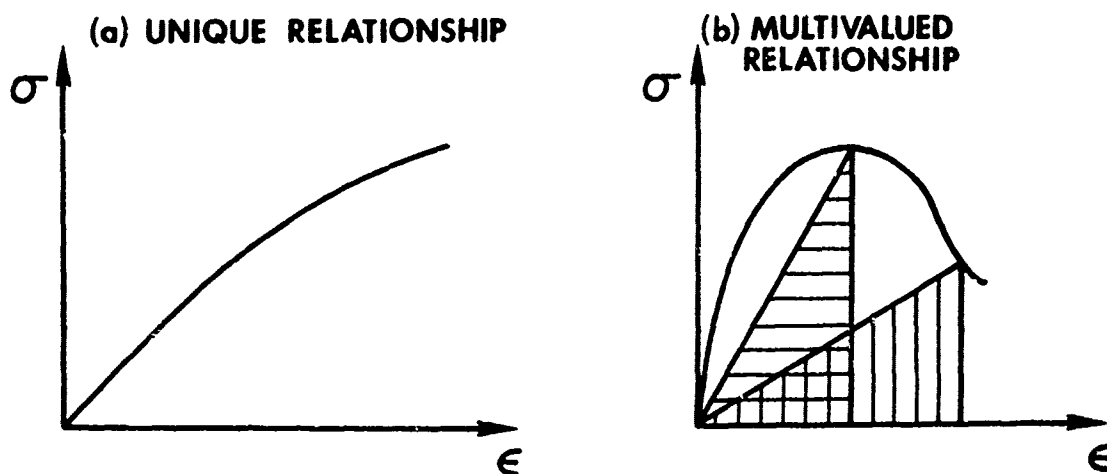


FIGURE 16 UNIQUENESS VERSUS NONUNIQUENESS OF THE MATERIAL PROPERTY-ENERGY RELATIONSHIP

the implied stress-strain curve. If the material property being described with Eq. 5 is a secant modulus, the stress-strain curves in Fig. 17 are representative of curves for two values of B which differ by an order of magnitude, e.g., curves for corresponding values of C in Figs. 14 and 15. The only variable in this schematic is B , i.e., the material property constants A , C , and U_0 are fixed. The points shown on the curves correspond to the implied stress and strain values for the condition $U = U_0$. As can be seen in Fig. 17, increasing B leads to a stress-strain curve with more curvature. Thus, the value of B is associated with the curvature of the stress-strain curve. On the other hand, increasing the value of C in Figs. 14 and 15 leads to an increased rate of change of curvature for a fixed value of B . Thus, the value of C is associated with the rate of change of curvature of the stress-strain curve.

The stress-strain curves in Fig. 18 are representative of all combinations of high and low values of B and C . The four combinations displayed in Fig. 18 can be characterized as follows:

- (a) Low B , Low C - small initial curvature with slow curvature growth
- (b) High B , Low C - larger initial curvature than (a) with slow curvature growth
- (c) Low B , High C - small initial curvature with rapid curvature growth
- (d) High B , High C - larger initial curvature than (c) with rapid curvature growth

In conclusion, the initial value of the material property is reflected by the positive material property constant A . If the material property being approximated is a direct modulus, the value of B is associated with the curvature of the stress-strain curve. The value of C , which is positive, is associated with the rate of change of curvature of the stress-strain curve.

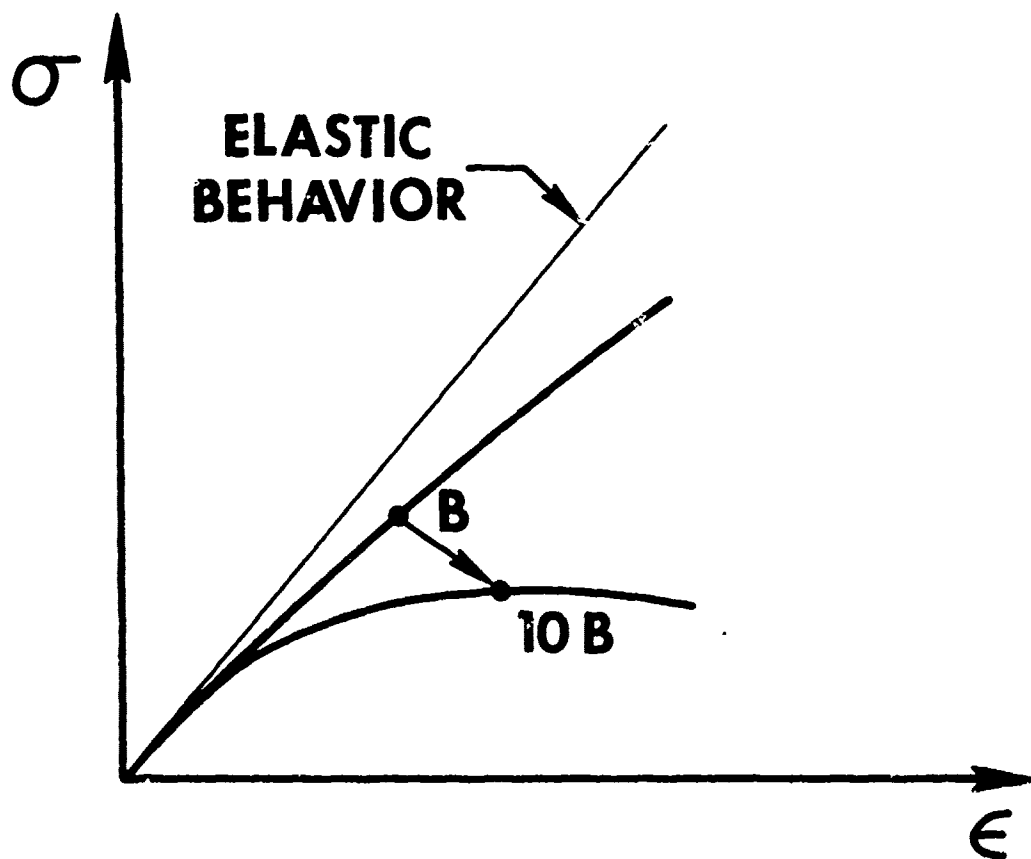


FIGURE 17 EFFECT OF MATERIAL CONSTANTS B ON THE STRESS-STRAIN CURVE

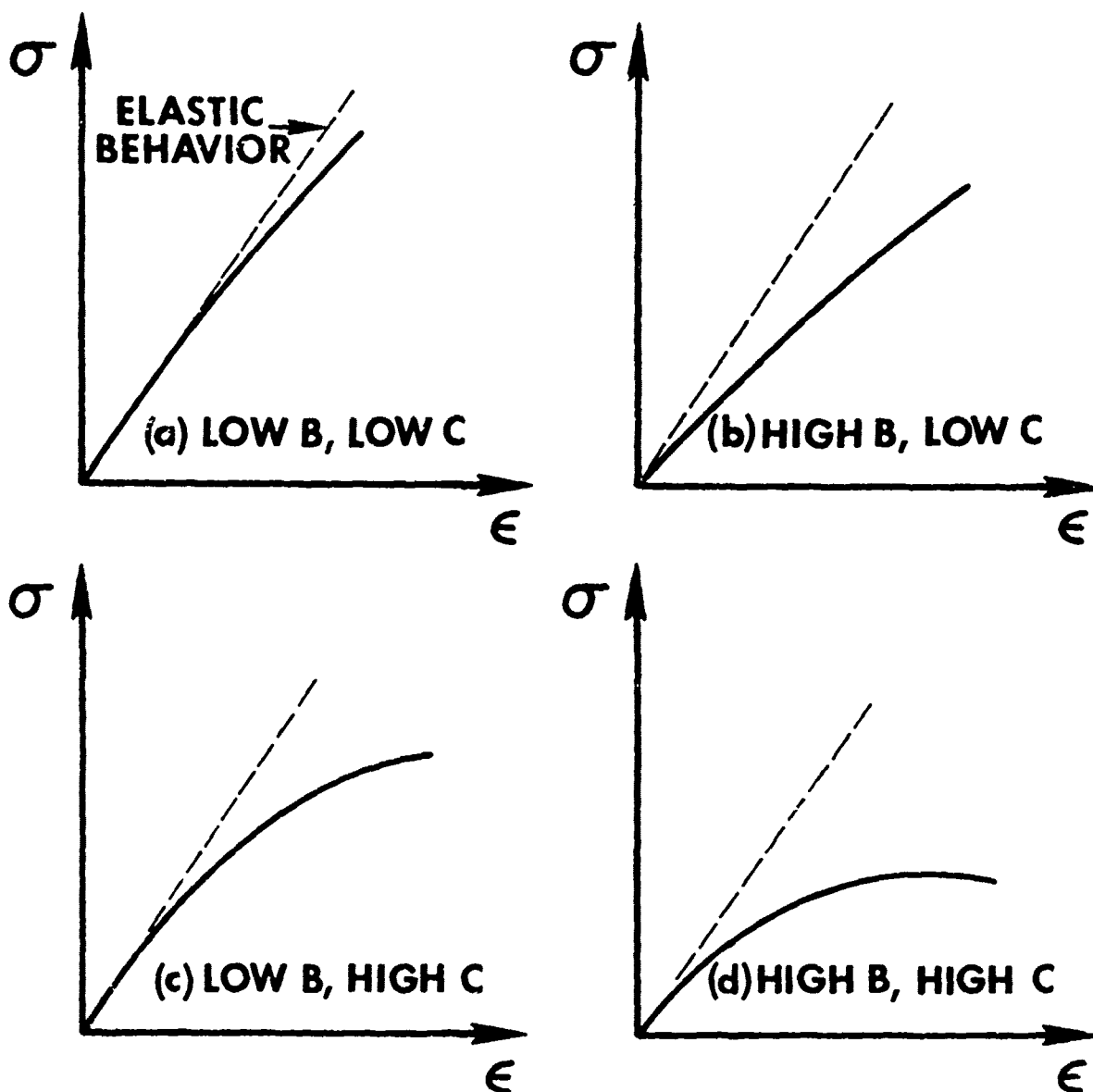


FIGURE 18 STRESS-STRAIN RESPONSE FOR VARIOUS RELATIVE MAGNITUDES OF B AND C

2.3 ITERATION AND CONVERGENCE STUDIES

The stresses, strains, and material properties are no longer constants but are highly interdependent functions of U . Thus, an iterative procedure was devised to simultaneously satisfy, within some small error, the nonlinear stress-strain relations and the material property strain energy equations. This procedure is schematically shown in Fig. 19. The first step is to determine the material property-versus-strain energy equations from available uniaxial data. In order to start the iterative procedure, initial values for the material properties are necessary. The most logical choice is the elastic or linear components of the material properties. The next step is to solve for the stresses and strains using these initial values of material properties in Eq. (5). Next, the strain energy, U , is found, and new material properties are determined for that value of U . Then, the stresses and strains are reevaluated for the revised material properties. The material properties, stresses and strains are modified until some convergence criterion for the relative change in the strain energy is satisfied.

A short computer program was developed to assess the feasibility of the iterative approach. Some results obtained in the uniaxial loading of a one-element plane stress model are shown in Fig. 20. The element in Fig. 21 was loaded with a stress of σ_z of 3513 psi. The predictions for the first five iterations of the procedure are shown in Fig. 20. For this problem, the procedure converges rapidly, a necessity for a procedure that is an integral part of a large finite element program. In such a program, a problem with a large number of elements can use a substantial amount of computer time for each iteration. Convergence is defined to occur for a multi-element problem only when all elements simultaneously satisfy the convergence criterion.

Because the present procedure does not contain any criterion on which to base failure of a material, a material property equation can be used far be-

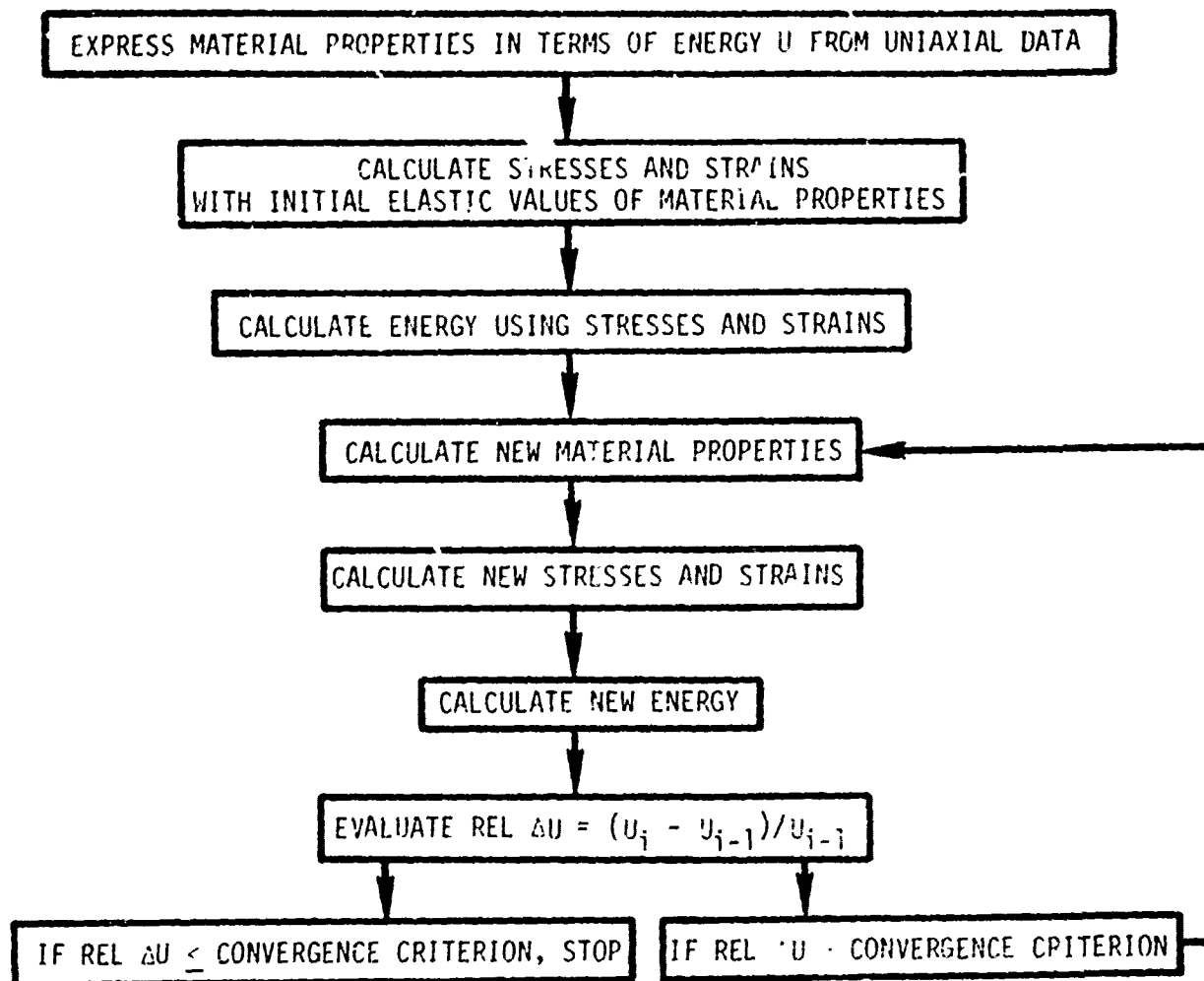


FIGURE 19 ITERATION PROCEDURE

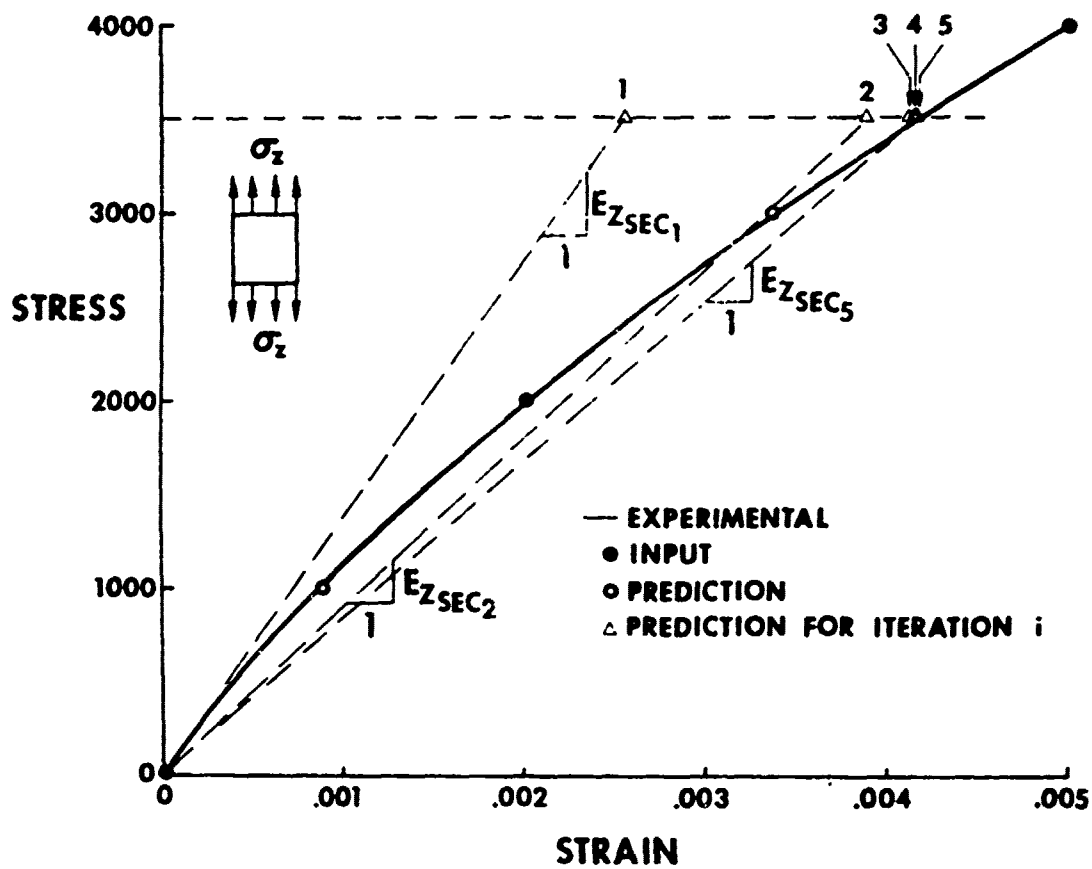


FIGURE 20 CONVERGENCE OF ITERATION PROCEDURE

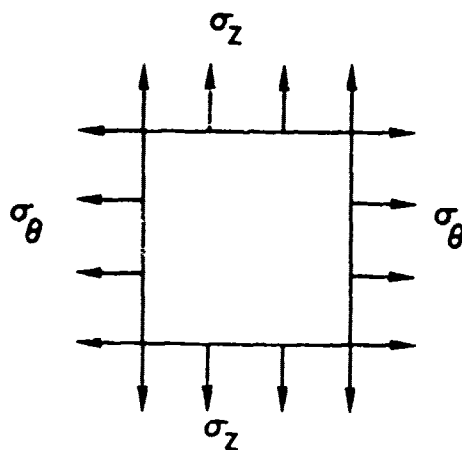


FIGURE 21 ONE-ELEMENT PLANE STRESS MODEL

yond its meaningful range. Two definitions of "meaningful range" exist:

1. The model representation of the material property versus strain energy curve might go to zero as the energy increases such as do the curves for $C > 1$ in Fig. 11. That is, we may have a bad curve fit of the material property-versus-strain energy relation as will be discussed in Section 2.4.2. The computational consequence of the material property-versus-strain energy curve touching or going below zero is a zero or negative element on the diagonal of the compliance matrix. This possibility is countered by users of the model by the methods discussed in Section 2.4.2.
2. The predicted energy may be greater than that required to fracture the material. We have not included a failure criterion as a termination of the present procedure. That is, we predict strains which could be above failure and hence beyond the meaningful range. However, the natural use of the material model in a design environment is in conjunction with a failure criterion. That coupling of procedures will not be discussed in this report.

This effect of the magnitude of the material constants on the convergence of the iterative procedure was studied by use of a brief computer program for a "one-element" uniform stress model. Convergence of the procedure is influenced by variables such as the loading, the material properties, how the material properties are approximated, and the convergence criterion. Thus, due to the number of variables, the results of this study are somewhat limited. For this investigation, the material is considered to be elastically isotropic. A constant Poisson's ratio of .32 is used along with a constant shear modulus of 4×10^6 psi. The convergence criterion is fixed to yield three significant figure accuracy for the strain energy density. The value of the nonlinear Young's modulus (E) is varied to evaluate its effect on the convergence of the iterative procedure. The material property constants A and U_0 are fixed at 10.5×10^6 psi and 1 psi, respectively. The modulus variations are induced by varying the material property constants B and C as shown in Table 3. For each case, a uniaxial tension, biaxial tension,

and triaxial tension loading condition with equal normal stresses of 72 ksi is investigated.

For each set of B and C values for the three loading conditions, the following results are presented in Table 3; an indication of the convergence of the procedure, the number of iterations required for convergence, and the strain energy density at convergence. For the divergent cases, the number of iterations is the number before a change in sign of the modulus occurred (a definite indication of divergence). Obviously, a strain energy density value for a divergent case would not be meaningful.

Table 3 EFFECT OF LOADING AND MATERIAL CONSTANTS B AND C ON CONVERGENCE OF ITERATION PROCEDURE

CASE	B	C	LOADING								
			UNIAXIAL			BIAXIAL			TRIAXIAL		
			CONVERGE?	NUMBER OF ITERATIONS	U	CONVERGE?	NUMBER OF ITERATIONS	U	CONVERGE?	NUMBER OF ITERATIONS	U
1	.0001	.5	Yes	2	247	Yes	2	337	Yes	2	267
2	↓	1.	Yes	3	260	Yes	4	362	Yes	3	283
3		1.15	Yes	4	290	Yes	6	445	Yes	5	321
4		1.2	Yes	6	322	No	8	-	Yes	7	367
5		1.25	No	10	-	No	3	-	No	6	-
6	.000001	1.	Yes	2	247	Yes	2	336	Yes	2	267
7	↓	1.8	Yes	4	269	Yes	5	405	Yes	4	295
8		1.85	Yes	5	281	No	12	-	Yes	5	313
9		1.9	Yes	6	308	No	4	-	Yes	10	372
10		1.95	No	7	-	No	3	-	No	5	-

Three general conclusions can be reached from the parametric study:

1. If only C changes in the material property equation for Young's modulus, the greater the value of C , the slower the convergence and the greater the likelihood of divergence.
2. Similarly, if only B changes in the material property equation for Young's modulus, the greater the value of B , the slower the convergence and the greater the likelihood of divergence.
3. If only the loading conditions vary, the uniaxial tension case is most likely to converge and will converge most rapidly of the three cases (uniaxial, biaxial, and triaxial) examined. At the same time, the biaxial tension case is the least likely to converge or will converge the slowest. Thus, biaxial stress states are the most crucial test of the convergence of the material model.

Thus, from conclusions 1 and 2, the greater the nonlinearity and the more rapidly it grows, the greater the possibility of divergence. The third conclusion may not seem palatable at first glance. Instead, the triaxial loading condition might be suspected to represent the most severe test of convergence. However, analysis of the energy conditions in uniaxial, biaxial, and triaxial loading states leads to a rational explanation of the situation.

Consider a linear elastic body composed of an isotropic material with a Poisson's ratio of .32 and loaded uniaxially, biaxially, and triaxially at the same stress level. The strain energy density is $.50\sigma\epsilon$ for the uniaxial stress state, $.68\sigma\epsilon$ for the biaxial stress state, and $.54\sigma\epsilon$ for the triaxial stress state. Thus, 36% greater strain energy density exists in the biaxial stress state than in the uniaxial stress state. Also, 8% greater strain energy density exists in the triaxial stress state than in the uniaxial stress state. These energy differences are larger for nonlinear elastic bodies because the higher the energy level, the greater the strain nonlinearity. However, the biaxial stress state obviously has the largest strain energy density. Therefore, it should not be surprising that the biaxial stress state converges slower and is more likely to diverge than the triaxial or the uniaxial stress states.

2.4 MATERIAL MODEL SENSITIVITY STUDIES

Three distinct sensitivity studies are discussed. First, the symmetry or nonsymmetry of the compliance matrix is investigated. Second, different approaches are examined for finding the constants in the material property equations [Eq. (5)]. Finally, the deviations in predicted strains resulting from $\pm 10\%$ variations in uniaxial strain data are determined.

2.4.1 Symmetry of the Compliance Matrix

In the formulation of the material model, deformations are assumed not to alter the degree or direction of the anisotropy of the material. This assumption is reflected in the symmetry of the compliance matrix and its similar form at all deformation levels. Since the material model can be generalized to different degrees of anisotropy, some of the implications of this assumption for ATJ-S graphite can be evaluated.

The computer program used to assess the feasibility of the iterative approach was used in this study. In the program, a one-element plane stress model is subjected to constant normal stresses as in Fig. 21. No displacement boundary conditions are imposed on the model. The stress-strain relations for the case under consideration degenerate to

$$\begin{Bmatrix} \epsilon_z \\ \epsilon_\theta \end{Bmatrix} = \begin{bmatrix} 1/E_z & -\nu_{\theta z}/E_\theta \\ -\nu_{z\theta}/E_z & 1/E_\theta \end{bmatrix} \begin{Bmatrix} \sigma_z \\ \sigma_\theta \end{Bmatrix} \quad (6)$$

Material property versus U equations for the four material properties (E_z , E_θ , $\nu_{z\theta}$, and $\nu_{\theta z}$) in Eq. (6) were determined from Jortner's tension tests on uniaxial specimens [30]. The numerical values of the constants in the material property equations used in this study are shown in Table 4.

TABLE 4: BASELINE VALUES OF CONSTANTS IN MATERIAL PROPERTY EQUATIONS*
FOR NONSYMMETRIC COMPLIANCE MATRIX STUDY

PROPERTY	A	B	C	U_0
E_z	1.370×10^6	.2318	.2551	1.
E_θ	1.720×10^6	.1016	.4458	1.
$\nu_{z\theta}$.1607	.4456	.1578	1.
$\nu_{\theta z}$.2018	.4401	.1470	1.

* A, B, C, and U_0 are defined in Eq. (5).

TABLE 5: STRAIN RESULTS FOR NONSYMMETRIC COMPLIANCE MATRIX STUDY

Case	σ_z	σ_θ	Unsymmetric		Symmetric with $-\nu_{z\theta}/E_z$		Symmetric with $-\nu_{\theta z}/E_\theta$	
			ϵ_z	ϵ_θ	ϵ_z	ϵ_θ	ϵ_z	ϵ_θ
1	1000	0	.000900	-.000088	.000900	-.000088	.000900	-.000077
2	2000	0	.002019	-.000163	.002019	-.000163	.002019	-.000140
3	3000	0	.003371	-.000230	.003371	-.000230	.003371	-.000197
4	4000	0	.005007	-.000289	.005007	-.000289	.005007	-.000251
5	1000	1000	.000851	.000550	.000839	.000550	.000852	.000562
6	2000	2000	.001987	.001244	.001962	.001234	.001989	.001269
7	3000	3000	.003450	.002143	.003416	.002140	.003455	.002176
8	4000	4000	.005382	.003385	.005348	.003381	.005388	.003417
9	0	1000	-.000079	.000619	-.000089	.000619	-.000079	.000619
10	0	2000	-.000144	.001313	-.000167	.001313	-.000144	.001313
11	0	3000	-.000203	.002100	-.000238	.002100	-.000203	.002100
12	0	4000	-.000259	.003003	-.000303	.003003	-.000259	.003003

Three different forms of the compliance matrix,

$$\begin{bmatrix} 1/E_z & -\nu_{\theta z}/E_\theta \\ -\nu_{z\theta}/E_z & 1/E_\theta \end{bmatrix} \begin{bmatrix} 1/E_z & -\nu_{z\theta}/E_z \\ -\nu_{z\theta}/E_z & 1/E_\theta \end{bmatrix} \begin{bmatrix} 1/E_z & -\nu_{\theta z}/E_\theta \\ -\nu_{\theta z}/E_\theta & 1/E_\theta \end{bmatrix}$$

were used in strain predictions for twelve different loading conditions.

Strain predictions for each of the cases analyzed are given in Table 5.

The nonsymmetry of the compliance matrix about the main diagonal has an almost negligible effect on the strain predictions for the present cases. Thus, the increased complexity created by the assumption of an unsymmetric compliance matrix may not be justified for ATJ-S graphite.

2.4.2 Evaluation of Material Constants

The second sensitivity study was performed to establish guidelines for evaluation of the constants appearing in the material property equations. A typical material property versus U curve for a direct modulus is shown as the solid curve in Fig. 22. The open circles are the actual data points used to define the curve. Beside each circle is the uniaxial stress level for that point. Also shown are three different numerical fits of Eq. (5) to the uniaxial test data. These three fits were obtained by simultaneously solving for the constants B and C of Eq. (5) using different data points. For all three cases, the same initial value was used for the constant A and a value of unity was assigned to U_0 . The data points used to define each curve are

<u>Type of Fit</u>	<u>Data Points Used</u>
Low	0, 2000, 3000
Standard	0, 3000, 5000
High	0, 4000, 5000

Three sets of material property equations for E_z , E_θ , and $\nu_{z\theta}$ were found in the manner just outlined. The stress levels of the data points were not

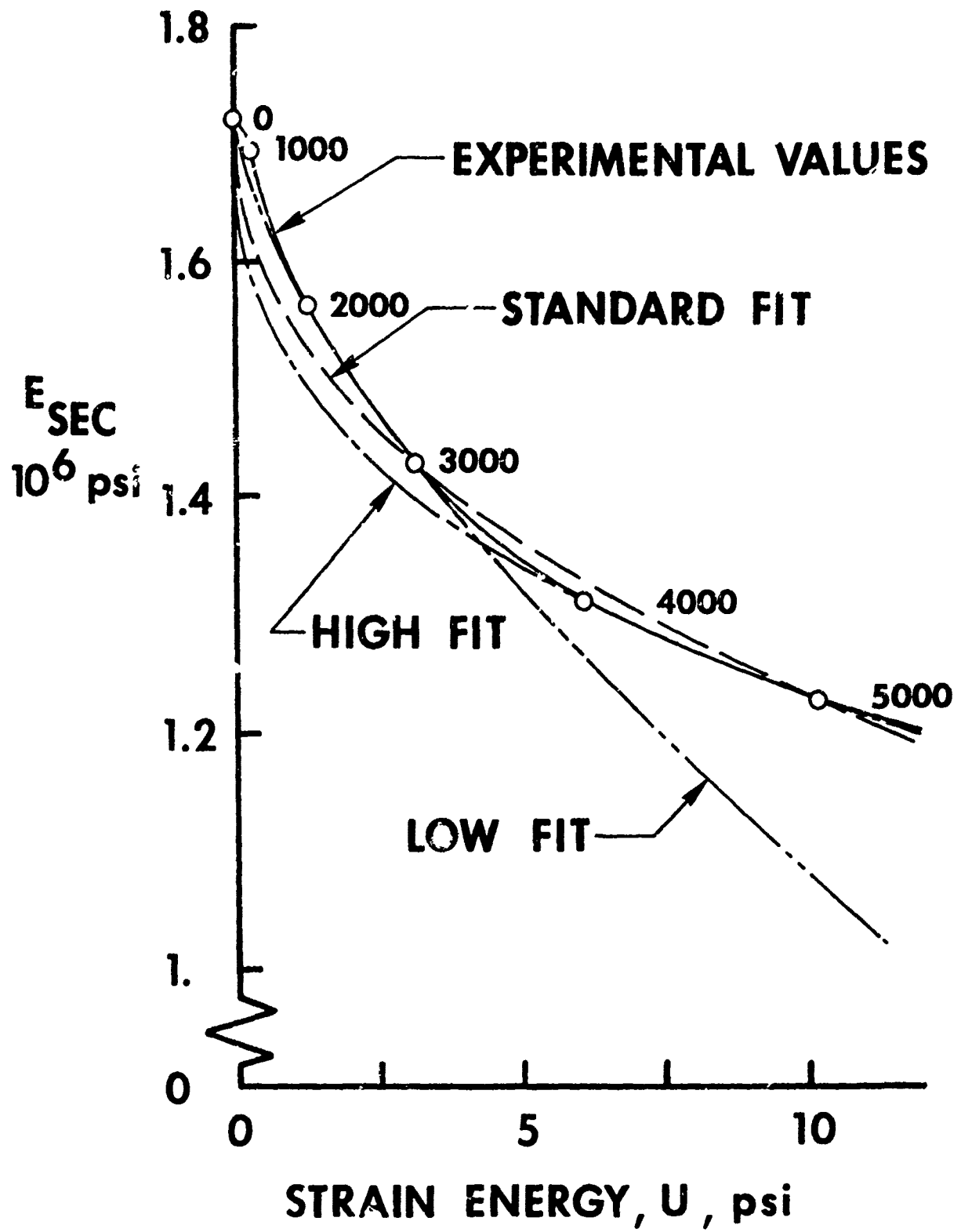


FIGURE 22 APPROXIMATION OF MODULUS-ENERGY DATA WITH MATERIAL PROPERTY EQUATIONS

identical for all properties. Each set of material property equations was analyzed at a number of loading conditions using the computer program for the one-element model previously described. The compliance matrix was assumed to be symmetric with the terms off the main diagonal being $-\nu_{z0}/E_z$. The constants in the material property equations were determined from Jortner's experimental results for the uniaxial test specimens [30].

Strain results are presented in Table 6 in the form of percentage deviations from strains obtained with the so-called standard fit of the material property equations to the data. These percentage deviations, which are a measure of error, are the difference between a ray from the origin of a biaxial strain plot as in Fig. 23 to the predicted values and a ray from the origin to the baseline values. The differences between the three types of material property equation fits are more pronounced as the energy level increases. In fact, for loading condition 8, the procedure is divergent for the low fit (this procedure apparently can diverge if the material properties change rapidly with U). The correlation between the three different data fits is relatively good at low energy levels. Perhaps the best approach to establish the constants in the material property equations is to use the standard fit or high fit approach in which the approximate energy for convergence is determined. Then, the constants in material property equations are adjusted to better fit the material properties in that region.

2.4.3 Variation in Material Properties

The third sensitivity study was undertaken to establish the deviations in predicted strain results introduced by $\pm 10\%$ variations in the input uniaxial stress-strain data [30]. At all stress levels, the strains are incremented by 10% as shown in Fig. 24. For the Poisson's ratio, only the transverse strains

TABLE 6: DEVIATIONS IN STRAINS FROM DIFFERENT PROCEDURES FOR DETERMINING MATERIAL CONSTANTS

CASE	σ_z psi	σ_θ psi	PERCENT DEVIATION FROM STANDARD FIT	
			HIGH FIT	LOW FIT
1	1000	0	1.48	- 4.41
2	2000	0	1.34	0.05
3	3000	0	0.81	10.65
4	4000	0	0.02	46.35
5	1000	1000	3.09	- 3.90
6	2000	2000	2.20	2.82
7	3000	3000	0.57	27.01
8	4000	4000	-2.35	*
9	0	1000	2.09	- 2.71
10	0	2000	2.53	- 2.48
11	0	3000	2.25	- 0.03
12	0	4000	1.49	6.73

* Procedure diverges for this case.

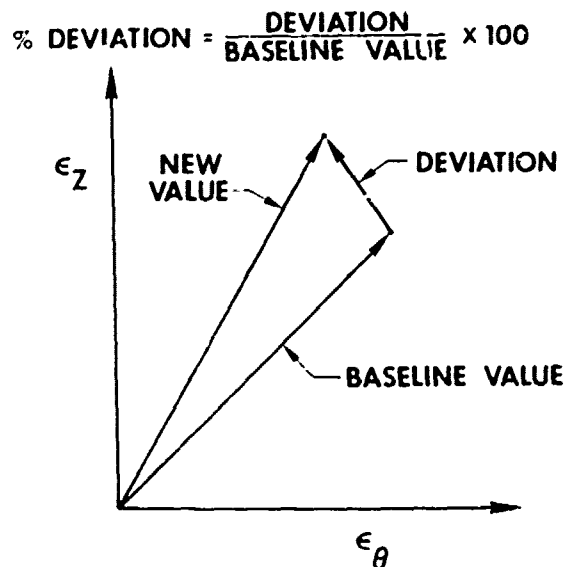


FIGURE 23 INTERPRETATION OF PERCENTAGE DEVIATIONS IN STRAINS

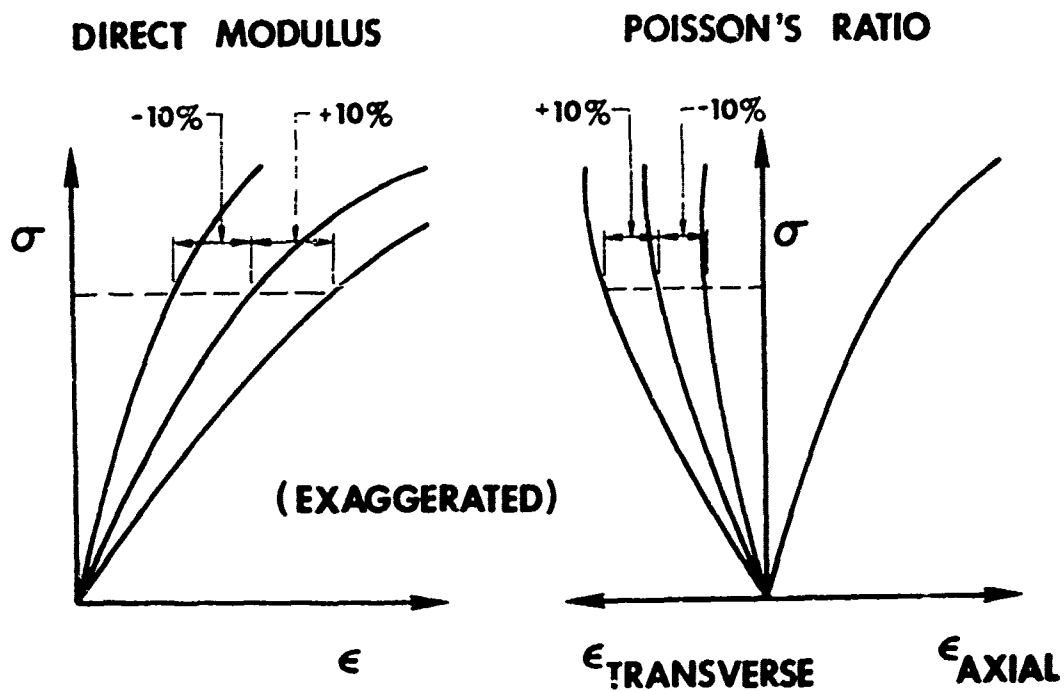


FIGURE 24 VARIATION OF MATERIAL PROPERTIES

are altered from the baseline values. New constants are determined for the material property equations from the artificially incremented strains. Note that all properties are simultaneously incremented.

Predicted strain results obtained using the program for the one-element model are given in Table 7. The loading conditions and compliance matrix symmetry are that used in the Evaluation of Material Constants study. The percentage deviations are interpreted as before (see Fig. 23). A 10% variation in the uniaxial strain data used to define the material property equations leads to approximately the same numerical variation in the predicted strain results. Thus, the material model is obviously very stable.

TABLE 7: DEVIATIONS IN STRAINS FOR ±10% VARIATIONS IN MATERIAL PROPERTIES

CASE	σ_z psi	σ_θ psi	PERCENT DEVIATIONS FROM STANDARD FIT	
			+10%	-10%
1	1000	0	10.09	-10.07
2	2000	0	10.07	-10.05
3	3000	0	10.04	-10.03
4	4000	0	10.03	-10.01
5	1000	1000	8.77	- 8.96
6	2000	2000	9.12	- 9.18
7	3000	3000	9.25	- 9.35
8	4000	4000	9.45	- 9.53
9	0	1000	10.07	-10.17
10	0	2000	10.20	-10.10
11	0	3000	10.12	-10.09
12	0	4000	10.08	-10.06

3. ELASTIC MODELS FOR DIFFERENT MODULI IN TENSION AND COMPRESSION

3.1 INTRODUCTION

The elastic behavior of materials with different moduli under tensile loading than under compressive loading is described briefly in Section 1.2. Two material models for this behavior will be described in this section.

In both models, the compliances, S_{ij} , in the strain-stress relations for axisymmetric bodies under axisymmetric loading

$$\begin{Bmatrix} \epsilon_r \\ \epsilon_z \\ \epsilon_\theta \\ \gamma_{rz} \end{Bmatrix} = \begin{bmatrix} s_{11}^{rz} & s_{12}^{rz} & s_{13}^{rz} & s_{16}^{rz} \\ s_{12}^{rz} & s_{22}^{rz} & s_{23}^{rz} & s_{26}^{rz} \\ s_{13}^{rz} & s_{23}^{rz} & s_{33}^{rz} & s_{36}^{rz} \\ s_{16}^{rz} & s_{26}^{rz} & s_{36}^{rz} & s_{66}^{rz} \end{bmatrix} \begin{Bmatrix} \sigma_r \\ \sigma_z \\ \sigma_\theta \\ \tau_{rz} \end{Bmatrix} \quad (7)$$

are determined based on the principal stress state. In principal stress coordinates, the strain stress relations are

$$\begin{Bmatrix} \epsilon_p \\ \epsilon_q \\ \epsilon_\theta \\ \gamma_{pq} \end{Bmatrix} = \begin{bmatrix} s_{11}^{pq} & s_{12}^{pq} & s_{13}^{pq} & s_{16}^{pq} \\ s_{12}^{pq} & s_{22}^{pq} & s_{23}^{pq} & s_{26}^{pq} \\ s_{13}^{pq} & s_{23}^{pq} & s_{33}^{pq} & s_{36}^{pq} \\ s_{16}^{pq} & s_{26}^{pq} & s_{36}^{pq} & s_{66}^{pq} \end{bmatrix} \begin{Bmatrix} \sigma_p \\ \sigma_q \\ \sigma_\theta \\ 0 \end{Bmatrix} \quad (8)$$

Note that (1) the θ -direction is always a principal stress direction because of the axisymmetric loading and (2) principal stress directions and principal strain coordinates do not coincide for orthotropic materials as they do for isotropic materials. The relation between the principal stress (p-q- θ) coordinates and the body (r-z- θ) coordinates is shown in Fig. 25. The θ -direction is toward the reader out of Fig. 25. Note that, by definition, the body coordinates coincide with the principal material coordinates for graphite. Transformation of stresses, strains, and material properties between these coordinate systems will be necessary.

The objective in both material models is to define a rational procedure

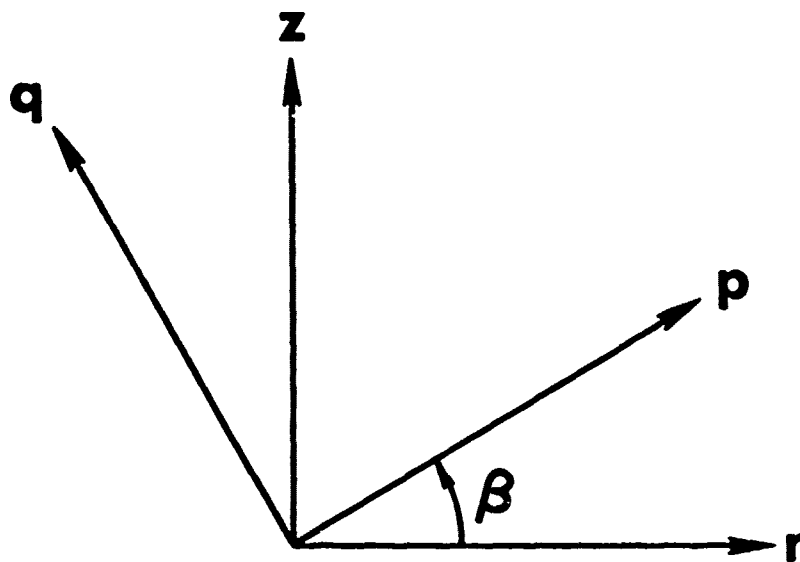


FIGURE 25 RELATION OF PRINCIPAL STRESS (p-q- θ) COORDINATES
TO BODY AND PRINCIPAL MATERIAL (r-z- θ) COORDINATES

for assigning the S_{ij}^{pq} on the basis of the principal stress state and the values of the S_{ij}^{pq} under tensile loading and those values under compressive loading. Because the material properties depend on the stress state and vice versa, the basic problem is statically indeterminate. However, the indeterminacy can be resolved by an apparently convergent iterative procedure consisting of four steps. First, displacement and stress calculations are performed based on an initial assumption of stress signs with an implied initial choice of material properties. Second, the appropriate material properties are selected based on the principal stresses calculated in the previous step. Third, displacements and stresses including the new principal stresses are recalculated. Fourth, steps two and three are repeated until convergence to the desired accuracy is achieved.

The first model, called the Weighted Compliance Model, is due to Jones [22, 24]. This model consists basically of adding the tensile and compressive compliances in proportion to the presence of the respective tensile and compressive principal stresses; hence, the name Weighted Compliance Model is used. No theoretical basis exists for the Weighted Compliance Model; it is an engineering approach, rather than a scientific approach, to a very difficult problem.

The second model, called the Restricted Compliance Model, is due mainly to Isabekian and Khachatrian [23] (modifications necessary to extend Isabekian and Khachatrian's model from a plane stress state to an axisymmetric stress state are described in Section 3.3). This model has a more scientific basis than the Weighted Compliance Model. Specifically, the compliance matrix is made symmetric by prescribing certain relations between the tensile and compressive properties so that they satisfy the known transformations of anisotropic elasticity. However, by enforcing these relations between tensile and compressive properties, we limit our ability to treat real engineering materials.

That is, some materials with different moduli in tension and compression do not have properties that satisfy the Isabekian and Khachatrian restrictions.

Both models are attempts to treat materials with different moduli in tension and compression as special anisotropic elastic materials with the compliance matrix symmetry characteristics of ordinary elastic materials (for which a potential function exists). This compliance matrix symmetry is a correction to the basic Ambartsumyan model with a nonsymmetric compliance matrix [21]. This correction is necessary if anisotropic elasticity theory is to be used once the compliances are determined. Both material models are described in the following sections and are contrasted in Section 3.4.

3.2 WEIGHTED COMPLIANCE MODEL

For an axisymmetric body under axisymmetric load, the following strain-stress relations in principal stress (p-q- θ) coordinates were proposed by Jones [24] for orthotropic materials that exhibit different moduli in tension and compression:

$$\begin{Bmatrix} \epsilon_p \\ \epsilon_q \\ \epsilon_\theta \\ \gamma_{pq} \end{Bmatrix} = \begin{bmatrix} S_{11}^{pq} & S_{12}^{pq} & S_{13}^{pq} & S_{16}^{pq} \\ S_{12}^{pq} & S_{22}^{pq} & S_{23}^{pq} & S_{26}^{pq} \\ S_{13}^{pq} & S_{23}^{pq} & S_{33}^{pq} & S_{36}^{pq} \\ S_{16}^{pq} & S_{26}^{pq} & S_{36}^{pq} & S_{66}^{pq} \end{bmatrix} \begin{Bmatrix} \sigma_p \\ \sigma_q \\ \sigma_\theta \\ 0 \end{Bmatrix} \quad (9)$$

Note again that the principal stress directions do not coincide with the principal strain directions. The compliances, S_{ij}^{pq} , are assigned according to the signs and magnitudes of the principal stresses:

$$\left. \begin{aligned} \text{if } \sigma_p > 0; S_{11}^{pq} &= S_{11}^{pq_t} \\ \text{if } \sigma_p < 0; S_{11}^{pq} &= S_{11}^{pq_c} \\ \text{if } \sigma_q > 0; S_{22}^{pq} &= S_{22}^{pq_t} \\ \text{if } \sigma_q < 0; S_{22}^{pq} &= S_{22}^{pq_c} \end{aligned} \right\} \quad \begin{array}{l} (10) \\ \text{(cont'd.} \\ \text{next} \\ \text{page)} \end{array}$$

$$\text{if } \sigma_\theta > 0; S_{33}^{pq} = S_{33t}^{pq}$$

$$\text{if } \sigma_\theta < 0; S_{33}^{pq} = S_{33c}^{pq}$$

$$\text{if } \sigma_p > 0 \text{ and } \sigma_q > 0; S_{12}^{pq} = S_{12t}^{pq}$$

$$\text{if } \sigma_p < 0 \text{ and } \sigma_q < 0; S_{12}^{pq} = S_{12c}^{pq}$$

$$\text{if } \sigma_p > 0 \text{ and } \sigma_q < 0; S_{12}^{pq} = k_{ppq} S_{12t}^{pq} + k_{qpq} S_{12c}^{pq}$$

$$\text{if } \sigma_p < 0 \text{ and } \sigma_q > 0; S_{12}^{pq} = k_{ppq} S_{12c}^{pq} + k_{qpq} S_{12t}^{pq}$$

$$\text{if } \sigma_p > 0 \text{ and } \sigma_\theta > 0; S_{13}^{pq} = S_{13t}^{pq}$$

$$\text{if } \sigma_p < 0 \text{ and } \sigma_\theta < 0; S_{13}^{pq} = S_{13c}^{pq}$$

$$\text{if } \sigma_p > 0 \text{ and } \sigma_\theta < 0; S_{13}^{pq} = k_{ppt} S_{13t}^{pq} + k_{tpt} S_{13c}^{pq}$$

$$\text{if } \sigma_p < 0 \text{ and } \sigma_\theta > 0; S_{13}^{pq} = k_{ppt} S_{13c}^{pq} + k_{tpt} S_{13t}^{pq}$$

$$\text{if } \sigma_q > 0 \text{ and } \sigma_\theta < 0; S_{23}^{pq} = S_{23t}^{pq}$$

$$\text{if } \sigma_q < 0 \text{ and } \sigma_\theta < 0; S_{23}^{pq} = S_{23c}^{pq}$$

$$\text{if } \sigma_q > 0 \text{ and } \sigma_\theta < 0; S_{23}^{pq} = k_{qqt} S_{23t}^{pq} + k_{tqt} S_{23c}^{pq}$$

$$\text{if } \sigma_q < 0 \text{ and } \sigma_\theta > 0; S_{23}^{pq} = k_{qqt} S_{23c}^{pq} + k_{tqt} S_{23t}^{pq}$$

$$\text{if } \sigma_p > 0; S_{16}^{pq} = S_{16t}^{pq}$$

$$\text{if } \sigma_p < 0; S_{16}^{pq} = S_{16c}^{pq}$$

$$\text{if } \sigma_q > 0; S_{26}^{pq} = S_{26t}^{pq}$$

$$\text{if } \sigma_q < 0; S_{26}^{pq} = S_{26c}^{pq}$$

$$\text{if } \sigma_\theta > 0; S_{36}^{pq} = S_{36t}^{pq}$$

$$\text{if } \sigma_\theta < 0; S_{36}^{pq} = S_{36c}^{pq}$$

where

$$k_{ppq} = -\frac{|\sigma_p|}{|\sigma_p| + |\sigma_q|}$$

$$k_{ppt} = \frac{|\sigma_p|}{|\sigma_p| + |\sigma_\theta|}$$

$$k_{qqt} = \frac{|\sigma_q|}{|\sigma_q| + |\sigma_\theta|}$$

$$k_{qpq} = \frac{|\sigma_q|}{|\sigma_p| + |\sigma_p|}$$

$$k_{tpt} = \frac{|\sigma_\theta|}{|\sigma_p| + |\sigma_\theta|}$$

$$k_{tqt} = \frac{|\sigma_\theta|}{|\sigma_q| + |\sigma_\theta|}$$

(10)

(cont'd.)

(11)

The weighting factors, k_{ppq} , etc., are used to make the compliance matrix symmetric. Some other function of the principal stresses could be used to define the weighting factors. Full qualification of the form of the weighting factors awaits definitive experimental work. Note that only two of the three principal stresses are used to determine each of the cross-compliances S_{12}^{pq} , S_{13}^{pq} , and S_{23}^{pq} . Furthermore, a single principal stress is used to determine each of the cross-compliances S_{16}^{pq} , S_{26}^{pq} , and S_{36}^{pq} . The compliance S_{66}^{pq} cannot be rationally defined nor is S_{66}^{pq} necessary for transformation to any other coordinate system. The reason for the perhaps surprising lack of importance of S_{66}^{pq} is that it vanishes identically from all transformation relations from principal stress coordinates to any other coordinates.

The compliance S_{ij}^{pq} and S_{ij}^{pq} in the principal stress (p-o) coordinates are related to the compliances S_{ij}^{rz} and S_{ij}^{rz} in the principal material and body (r-z) coordinates by the usual transformations of anisotropic elasticity:

$$S_{11tc}^{pq} = S_{11tc}^{rz} \cos^4 \beta + (2S_{12tc}^{rz} + S_{66tc}^{rz}) \sin^2 \beta \cos^2 \beta + S_{22tc}^{rz} \sin^4 \beta$$

$$S_{12tc}^{pq} = S_{12tc}^{rz} + (S_{11tc}^{rz} + S_{22tc}^{rz} - 2S_{12tc}^{rz} - S_{66tc}^{rz}) \sin^2 \beta \cos^2 \beta$$

$$S_{13tc}^{pq} = S_{13tc}^{rz} \cos^2 \beta + S_{23tc}^{rz} \sin^2 \beta$$

$$S_{16tc}^{pq} = (S_{66tc}^{rz} - 2S_{11tc}^{rz} + 2S_{12tc}^{rz}) \cos^3 \beta \sin \beta - (S_{66tc}^{rz} - 2S_{22tc}^{rz} + 2S_{12tc}^{rz}) \sin^3 \beta \cos \beta$$

$$S_{22tc}^{pq} = S_{11tc}^{rz} \sin^4 \beta + (2S_{12tc}^{rz} + S_{66tc}^{rz}) \sin^2 \beta \cos^2 \beta + S_{22tc}^{rz} \cos^4 \beta$$

$$S_{23tc}^{pq} = S_{13tc}^{rz} \sin^2 \beta + S_{23tc}^{rz} \cos^2 \beta$$

$$S_{26tc}^{pq} = (S_{66tc}^{rz} - 2S_{11tc}^{rz} + 2S_{12tc}^{rz}) \sin^3 \beta \cos \beta - (S_{66tc}^{rz} - 2S_{22tc}^{rz} + 2S_{12tc}^{rz}) \sin \beta \cos^3 \beta$$

(12)
(cont'd.
next
page)

$$\left. \begin{aligned} S_{33tc}^{pq} &= S_{33tc}^{rz} \\ S_{36tc}^{pq} &= 2(S_{23tc}^{rz} - S_{13tc}^{rz}) \sin\beta \cos\beta \end{aligned} \right\} \begin{array}{l} (12) \\ (\text{cont'd.}) \end{array}$$

where the subscript t or c is taken as appropriate, and β is the angle between the body (r-z- θ) and principal material coordinates and the principal stress (p-q- θ) coordinates as defined in Fig. 25.

The compliances in principal material coordinates, S_{ijtc}^{rz} , are related to the engineering constants (direct moduli, Poisson's ratios, and shear moduli) by:

$$\left. \begin{aligned} S_{11tc}^{rz} &= 1/E_{rtc} \\ S_{12tc}^{rz} &= -\nu_{rztc}/E_{rtc} = -\nu_{zrtc}/E_{ztc} \\ S_{13tc}^{rz} &= -\nu_{retc}/E_{rtc} = -\nu_{\theta rtc}/E_{\theta tc} \\ S_{22tc}^{rz} &= 1/E_{ztc} \\ S_{23tc}^{rz} &= -\nu_{z\theta tc}/E_{ztc} = -\nu_{\theta ztc}/E_{\theta tc} \\ S_{33tc}^{rz} &= 1/E_{\theta tc} \\ S_{66tc}^{rz} &= 1/G_{rztc} \end{aligned} \right\} (13)$$

where $\nu_{rzt} = -\epsilon_z/\epsilon_r$ for $\sigma_r = \sigma_t$ and all other stresses are zero. There are apparently seven independent material properties in tension in Eq. (13) and the same number in compression. However, the compliances S_{66t}^{rz} and S_{66c}^{rz} ($1/G_{rzt}$ and $1/G_{rzc}$, respectively) cannot be measured in a shear test on an orthotropic material with different moduli in tension and compression since one principal stress is tension and the other is compression. Instead, in accordance with a suggestion by Tsai [31], the tension modulus at 45 degrees

to the principal material axes, E'_t , is measured and S_{66t}^{rz} is obtained from

$$S_{66t}^{rz} = \frac{1}{G_{rzt}} = \frac{4}{E'_t} - \frac{1}{E_{rt}} + \frac{1}{E_{zt}} - \frac{2\nu_{rzt}}{E_{rt}} \quad (14)$$

A similar relation is used to define S_{66c}^{rz} in terms of E'_c .

For axisymmetrically loaded axisymmetric transversely isotropic bodies, $E_{rtc} = E_{etc}$ and $\nu_{rztc} = \nu_{etzc}$ so the remaining independent properties are

$$E_{rtc}, \nu_{rztc}, \nu_{retc}, E_{ztc}, E'_{tc} \quad (15)$$

i.e., five properties in tension and five in compression for a total of ten independent properties.

3.3 RESTRICTED COMPLIANCE MODEL

Isabekian and Khachatrian [23] define a symmetric compliance matrix for orthotropic materials with different moduli in tension and compression. They require the material properties in principal material directions to have inter-relationships such that the compliances are symmetric in any coordinate system. These relationships are obtained in addition to the usual Ambartsumyan approach of superposing stress states of uniaxial tension in one direction and uniaxial compression in the other direction.

For example, if $\sigma_p > 0$ and $\sigma_q < 0$, then the strain-stress relations are

$$\left. \begin{aligned} \epsilon_p &= S_{11t}^{pq} \sigma_p + S_{12c}^{pq} \sigma_q \\ \epsilon_q &= S_{12t}^{pq} \sigma_p + S_{22c}^{pq} \sigma_q \\ \gamma_{pq} &= S_{16t}^{pq} \sigma_p + S_{26c}^{pq} \sigma_q \end{aligned} \right\} \quad (16)$$

For these relations to be symmetric,

$$S_{12t}^{pq} = S_{12c}^{pq} \quad (17)$$

If the compliance matrix is to be symmetric in principal material (r-z) directions, then

$$\frac{\nu_{rzt}}{E_{rt}} = \frac{\nu_{rzc}}{E_{rc}} = \frac{\nu_{zrt}}{E_{zt}} = \frac{\nu_{zrc}}{E_{zc}} \quad (18)$$

If, moreover, Eq. (17) is to be valid in all coordinate system, then

$$\frac{1}{E_{rt}} - \frac{1}{E_{rc}} = \frac{1}{E_{zt}} - \frac{1}{E_{zc}} = \frac{1}{E'_t} - \frac{1}{E'_c} \quad (19)$$

in which E'_t and E'_c are the tensile and compressive moduli, respectively, at 45° to the principal material directions. Note that E'_t and E'_c are related to the shear moduli in all tension or all compression stress states by Eq. (14) and its compression equivalent. Accordingly, the five independent material properties are

$$E_{rt}, E_{zt}, \nu_{rzt}, E'_t, E_{rc} \quad (20)$$

or

$$E_{rc}, E_{zc}, \nu_{rzc}, E'_c, E_{rt} \quad (21)$$

or other appropriate combinations of the foregoing relations.

For axisymmetric bodies under axisymmetric loads, the foregoing properties for the plane stress case must be supplemented by additional material properties. Because of the two kinds of axisymmetry, no additional shear modulus - related properties are necessary. However, the direct moduli $E_{\theta tc}$ must be defined in addition to the Poisson's ratios $\nu_{r\theta tc}$ and $\nu_{z\theta tc}$. The θ -direction is automatically a principal stress direction. Thus, σ_{33} in any coordinate system is affected only by $E_{\theta tc}$ and no other moduli because of the simplicity of the transformation relation. The cross-compliances S_{13} and S_{23} are symmetric under mixed tensile and compressive loading in principal material coordinates if

$$\nu_{r\theta t}/E_{zt} = \nu_{r\theta c}/E_{zc} \quad (22)$$

$$\frac{\nu_{z\theta t}}{E_{zt}} = \frac{\nu_{z\theta c}}{E_{zc}} \quad (23)$$

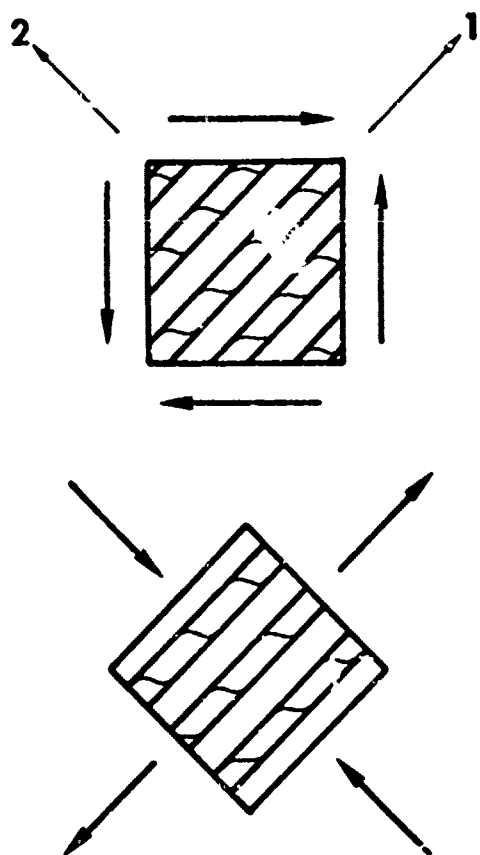
However, E_{rt} , E_{rc} , E_{zt} , and E_{zc} are either independent properties or dependent and determined from Eq. (19). Thus, only two Poisson's ratios are independent, say ν_{rt} and ν_{rc} . All transformations of stresses to obtain principal stresses are rotations about the θ -direction. Hence, no conditions are imposed on $E_{\theta t}$ and $E_{\theta c}$. That is, no relation like Eq. (19) exists between $E_{\theta t}$ and $E_{\theta c}$. Accordingly, nine independent material properties are required for analyses of axisymmetrically loaded axisymmetric solids made of orthotropic multimodulus materials. Five of these properties come from the plane stress model and four are from the extension to axisymmetric solids. For transversely isotropic materials like ATJ-S graphite with the plane of isotropy in the r - θ plane, $E_{\theta} = E_r$ and $\nu_{rz} = \nu_{\theta z}$, etc. With these reductions, the six independent material properties are

$$E_{rt}, E_{zt}, \nu_{rt}, \nu_{rc}, E'_t, E_{rc} \quad (24)$$

or appropriate equivalents through the foregoing relations.

As one consequence of the Restricted Compliance Model, the shear modulus for pure shear in coordinates 45° from the principal material coordinates can be shown to be independent of the sign of the shear stress. Consider, for example, the elements from a unidirectionally reinforced composite material shown in Fig. 26. There, the positive shear stress leads to tensile principal stress in the fiber direction and compressive principal stress in the direction transverse to the fibers. Similarly, the negative shear stress leads to compressive stress in the fiber direction and tensile stress in the transverse direction. Because the tensile and compressive moduli are different in the fiber and transverse directions, the shear moduli at 45° would seem to be different on purely rational grounds. However, because of the relations between tensile and compressive moduli in Eq. (19), the expressions for the shear modulus at 45° under positive

POSITIVE SHEAR STRESS



NEGATIVE SHEAR STRESS

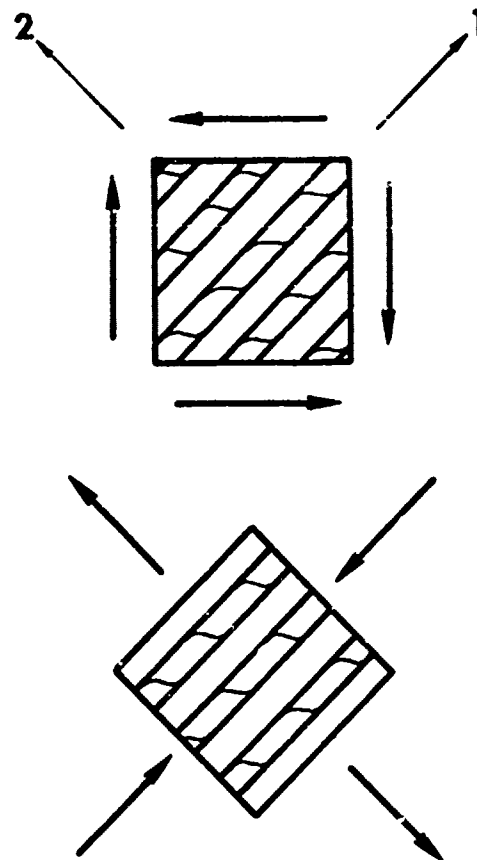


FIGURE 26 POSITIVE AND NEGATIVE SHEAR STRESS
AT 45° TO PRINCIPAL MATERIAL DIRECTIONS

shear stress can be shown to be identical to the expression for the shear modulus at 45° under negative shear stress.

3.4 SUMMARY

Irrespective of the material model used, the strain-stress relations in principal stress coordinates must be transformed to the body (r-z- θ) coordinates for solution of equilibrium problems. Those transformations take place according to the usual transformation relations of anisotropic elasticity:

$$\left. \begin{aligned}
 s_{11}^{rz} &= s_{11}^{pq} \cos^4 \beta + 2s_{12}^{pq} \sin^2 \beta \cos^2 \beta \\
 &\quad + s_{22}^{pq} \sin^4 \beta - (s_{16}^{pq} \cos^2 \beta + s_{26}^{pq} \sin^2 \beta) \sin 2\beta \\
 s_{12}^{rz} &= s_{12}^{pq} + (s_{11}^{pq} + s_{22}^{pq} - 2s_{12}^{pq}) \sin^2 \beta \cos^2 \beta \\
 &\quad - \frac{1}{2}(s_{26}^{pq} - s_{16}^{pq}) \sin 2\beta \cos 2\beta \\
 s_{16}^{rz} &= -[s_{22}^{pq} \sin^2 \beta - s_{11}^{pq} \cos^2 \beta + s_{12}^{pq} \cos 2\beta] \sin 2\beta \\
 &\quad + s_{16}^{pq} \cos^2 \beta (\cos^2 \beta - 3 \sin^2 \beta) + s_{26}^{pq} \sin^2 \beta (3 \cos^2 \beta - \sin^2 \beta) \\
 s_{22}^{rz} &= s_{11}^{pq} \sin^4 \beta + 2s_{12}^{pq} \sin^2 \beta \cos^2 \beta \\
 &\quad + s_{22}^{pq} \cos^4 \beta + (s_{16}^{pq} \sin^2 \beta + s_{26}^{pq} \cos^2 \beta) \sin 2\beta \\
 s_{26}^{rz} &= -[s_{22}^{pq} \cos^2 \beta - s_{11}^{pq} \sin^2 \beta - 2s_{12}^{pq} \cos 2\beta] \sin 2\beta \\
 &\quad + s_{16}^{pq} \sin^2 \beta (3 \cos^2 \beta - \sin^2 \beta) + s_{26}^{pq} \cos^2 \beta (\cos^2 \beta - 3 \sin^2 \beta) \\
 s_{66}^{rz} &= -(s_{11}^{pq} + s_{22}^{pq} - 2s_{12}^{pq}) \sin^2 \beta \cos^2 \beta \\
 &\quad - 2(s_{26}^{pq} - s_{16}^{pq}) \sin 2\beta \cos 2\beta
 \end{aligned} \right\} \quad (25)$$

Moreover, stresses and displacements from both models for two distinct problems cannot be superimposed as can solutions for linear elastic problems.

Superposition is invalid because the principal stress directions for two sets of stresses on the same body are generally different. However, if the principal stress directions are identical in both solutions, then the solutions can be superimposed. Ambartsumyan [21] terms this general invalidity of superposition a form of nonlinearity. In practical terms, each problem must be separately solved, and no building up of many solutions by superposition of simple solutions should be expected.

The two material models described in this section have different numbers of independent material properties. The Restricted Compliance Model has six independent properties for an axisymmetrically loaded axisymmetric transversely isotropic body. For the same body, the Weighted Compliance Model has ten independent properties. Both models have advantages (and disadvantages). The Restricted Compliance Model is derivable on a rational scientific basis; however, the compliance restrictions, as will be seen in Section 4, are too stringent for many real materials. On the other hand, the Weighted Compliance Model is not derivable because the weighting factors are somewhat arbitrary; however, this model has the flexibility in "acceptable" compliances to be applicable to many real materials. Thus, the Weighted Compliance Model is an engineering approximation whereas the Restricted Compliance Model is a more scientific description of the basic phenomenon, but is restricted to a more limited class of materials.

4. NONLINEAR DEFORMATION MODELS FOR DIFFERENT MODULI IN TENSION AND COMPRESSION

4.1 INTRODUCTION

The objective of this section is to simultaneously model the tensile and compressive stress-strain behavior of graphite shown in Figs. 27 and 28, respectively. The tensile behavior is typical of a material that softens under increasing stress. That is, among other characteristics, the Poisson's ratios decrease as the stress increases leading to the softening behavior illustrated in Fig. 3. On the other hand, the compressive behavior is more nearly characteristic of a hardening material. That is, the Poisson's ratios are constant or increase as the stress increases. Thus, we might expect the hardening behavior (although certainly not hardening in the sense of a concave upward stress-strain curve as in Fig. 10) illustrated in Fig. 3. Accordingly, strain profiles for various increasing stress levels might exist as schematically shown in Fig. 29 with biaxial tension in the upper right-hand quadrant and biaxial compression in the lower left-hand quadrant. However, no biaxial compression data exist to verify this speculation. Moreover, the behavior is not well-defined, although some measurements have been made and will be discussed in Section 6.

The contrasting tensile and compressive behavior illustrated in Fig. 29 may be perfectly realistic when the deformation mechanisms in tension are compared with the mechanisms in compression. Specifically, microcracking in tension leads to an apparent increase in volume (decreasing Poisson's ratios). However, in compression, microcracking may not occur. The microcracking phenomenon may be related to the porous nature of graphite. The pores have a tendency to open and perhaps tear under tensile stress. On the other hand, the pores would have a tendency to close and perhaps collapse under compression. Because

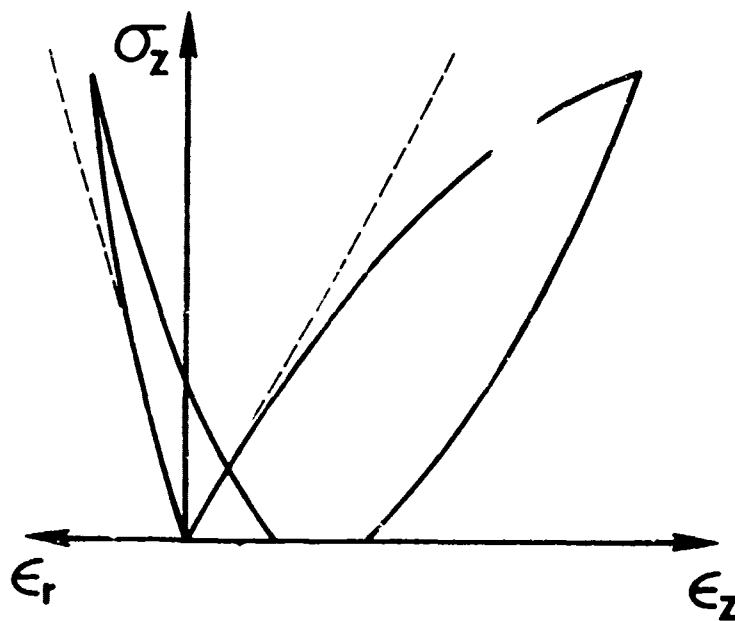


FIGURE 27 TENSILE STRESS-STRAIN BEHAVIOR OF GRAPHITE

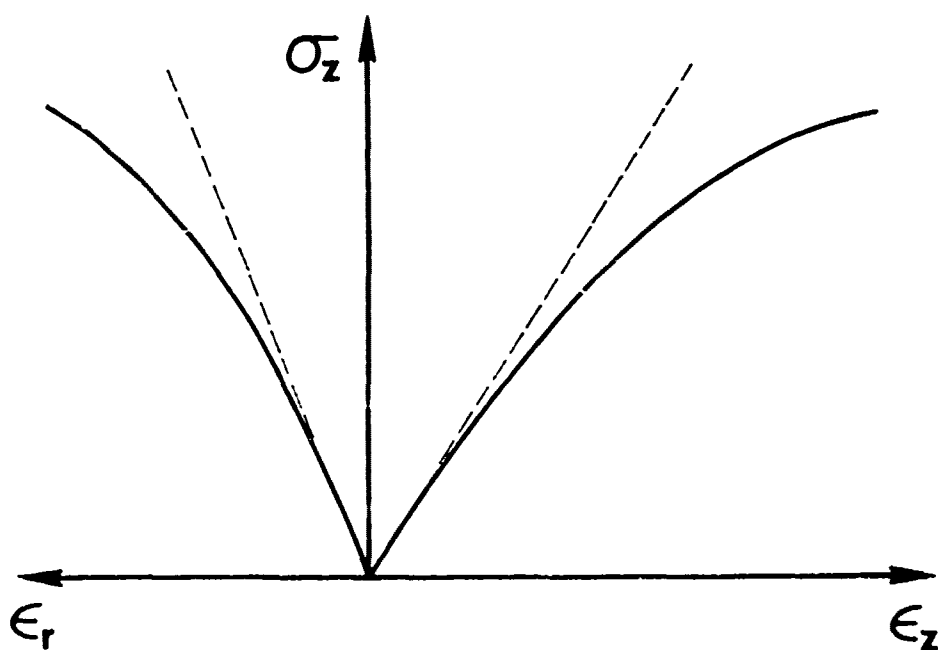


FIGURE 28 COMPRESSIVE STRESS-STRAIN BEHAVIOR OF GRAPHITE

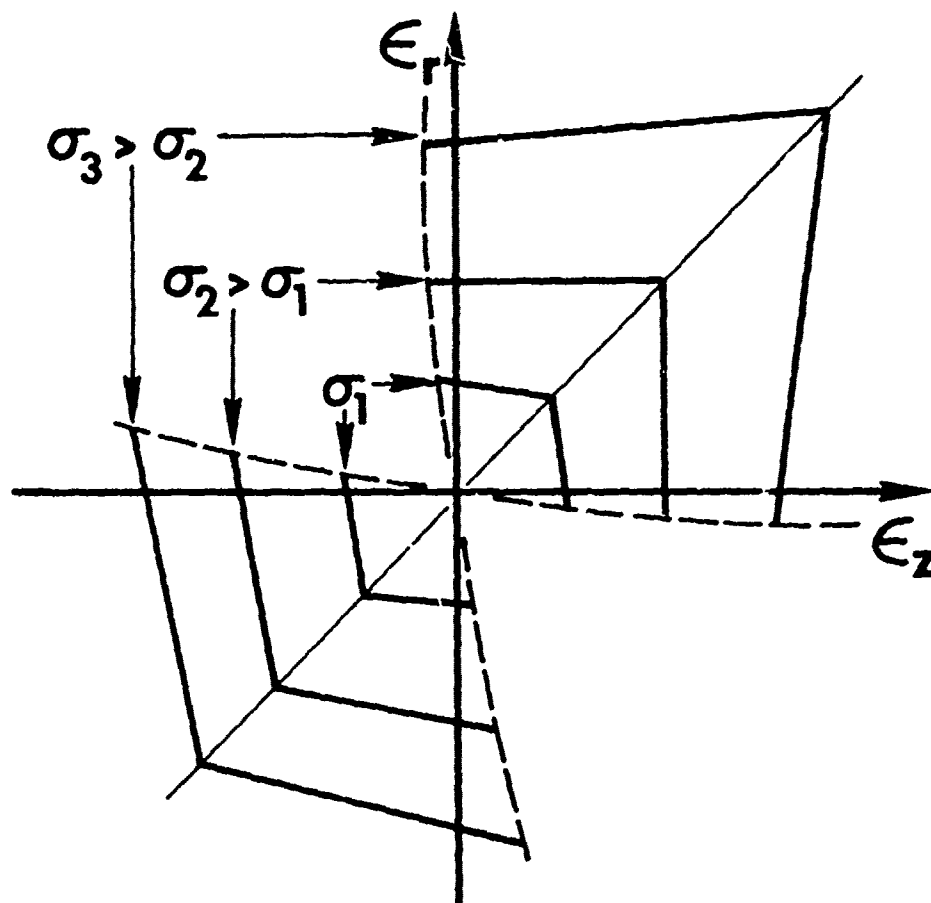


FIGURE 29 STRAIN PROFILES UNDER INCREASING STRESS LEVELS FOR A MATERIAL THAT SOFTENS UNDER TENSION AND HARDENS UNDER COMPRESSION

of the pores, graphite and other porous nonmetallic materials can have plastic volume changes when subjected to tensile or compressive stresses. Under compression, porous materials can compact (decrease in volume) whereas, under tension, they can dilate (increase in volume). Thus, classical plasticity theories with the usual zero plastic volume change hypothesis are not applicable to porous materials.

The nonlinear material model described in Section 2 is combined in this section with the linear multimodulus material models of Section 3 to obtain nonlinear multimodulus material models. With the material models of this section, both the nonlinear and multimodulus deformation behavior of an orthotropic material can be modeled simultaneously, a necessity for description of the behavior of ATJ-S graphite.

Two nonlinear multimodulus models with the same basic approach to nonlinear behavior are considered. Thus, the distinction between the models is based solely on the multimodulus formulations or, more specifically, on the determination of the compliance matrix. Isabekian and Khachatrian's extension [23] of Ambartsumyan's linear multimodulus approach [21] is used in what is called the "nonlinear restricted compliance model" (RCM). The linear multimodulus compliance approach of the RCM model is discussed in Section 3.2. In the other material model, called the "nonlinear weighted compliance model" (WCM), the linear multimodulus approach developed by Jones [22, 24] (which has been described in Section 3.3) is combined with the nonlinear approach described in Section 2.

The discussion of the nonlinear multimodulus material models is divided into five major sections. The general characteristics of the iteration procedure common to both material models are discussed in Section 4.2. The energy functions used to relate the multiaxial stress state to the material properties

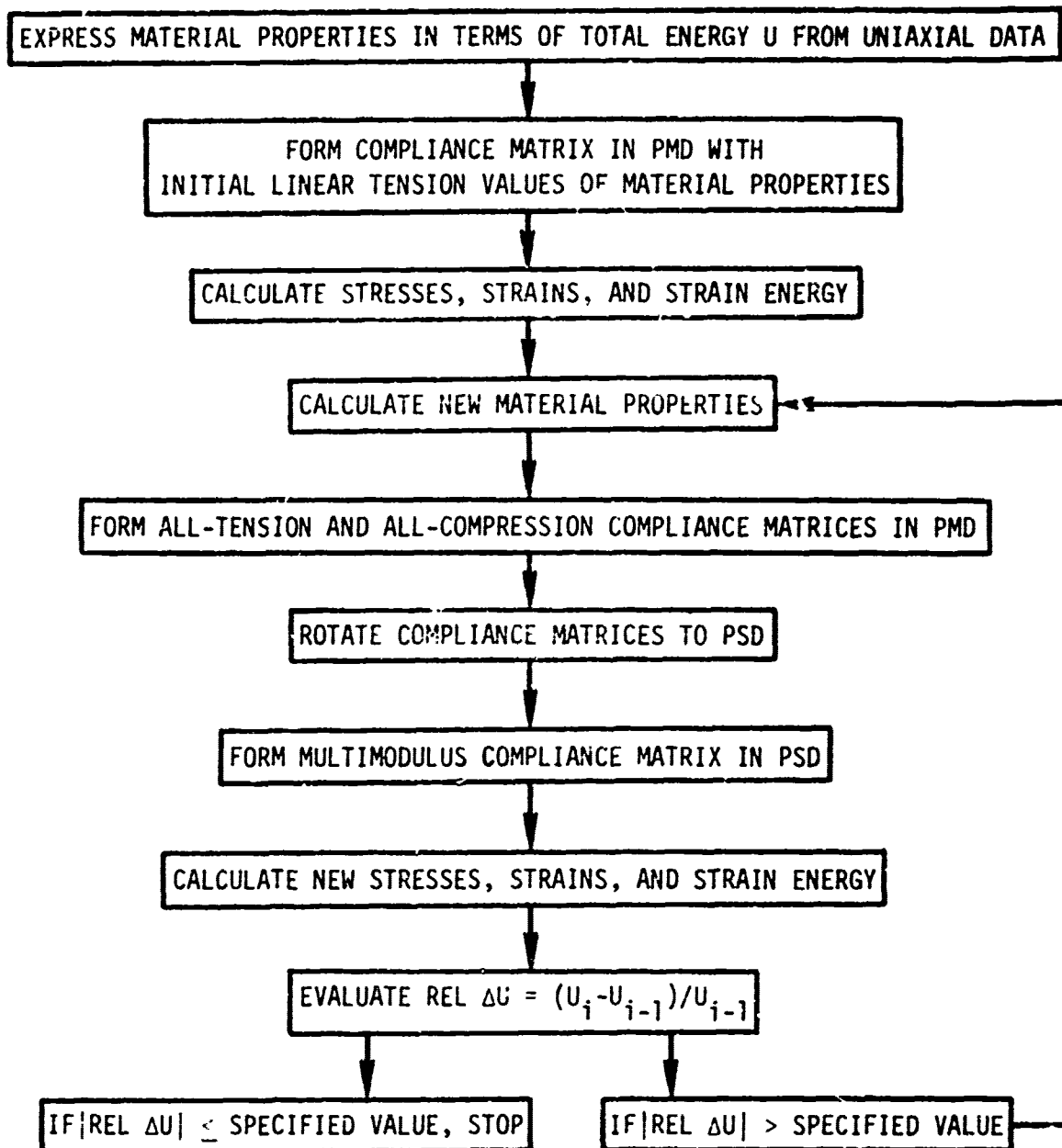
are described in Section 4.3. The distinctive characteristics of the nonlinear restricted compliance material model and the nonlinear weighted compliance model are discussed in Section 4.4 and 4.5, respectively. Some summary remarks on the two nonlinear multimodulus models are given in Section 4.6.

4.2 ITERATION PROCEDURE FOR MATERIAL MODELS

The overall iteration procedure common to both the nonlinear multimodulus material models will be described. In both the nonlinear model and the multimodulus models previously discussed, an indeterminate system is solved with an iterative approach. The stresses and strains are dependent on the material properties, and they, in turn, are dependent on the stresses and strains. In the nonlinear approach of Section 2, the material properties are related to the strain energy (density), which is found from the product of the stresses and the respective strains. In the linear multimodulus models, the composition of the compliance matrix, hence the material properties, is determined from the signs of the principal stresses. In the nonlinear multimodulus material models, the selection of material properties and, consequently, the stress-strain relationships is based on both the signs of the principal stresses and the magnitude of an energy function.

The iteration procedure devised to simultaneously satisfy the constraints of both the nonlinear and multimodulus problems is illustrated schematically in Fig. 30. Each step in the procedure is described in the following paragraphs.

The first step in the iteration procedure is to determine the material property-versus-strain energy relationships independently in tension and in compression from available uniaxial data. For ATJ-S graphite, the general form of Eq. (5) is suitable for representing the material property variations with strain energy. Thus, sets of constants A , B , C and U_0 are determined for each independent material property. Separate sets of constants are determined



PMD = PRINCIPAL MATERIAL DIRECTIONS

PSD = PRINCIPAL STRESS DIRECTIONS

FIGURE 30 ITERATION PROCEDURE FOR NONLINEAR MULTIMODULUS MATERIALS

for the tension and compression representation of a material property variation with strain energy if both sets are input to the procedure as independent material properties. The number of independent properties required for an analysis is dependent on the symmetry of the body and loading, the material model used, and, of course, the degree of anisotropy of the material. For an axisymmetric body under axisymmetric load, the number of independent material properties for three levels of anisotropy (i.e., isotropic, transversely isotropic, and orthotropic) is defined in the discussions of the multimodulus models.

To initiate the iteration procedure, the linear or "elastic" components of the tensile material properties are used. The desired stresses and strains (including the principal stresses and strains) can be computed. The principal stresses and their orientation are required for the multimodulus formulations. The strain energies are calculated from the stresses and strains by use of one of three strain energy approaches discussed in the next section. The strains in principal stress directions need be computed only if the separate contributions to the total energy of the tensile and compressive stresses are used.

After the strain energies are evaluated, new independent material properties are found. This revised set of material properties is used to formulate new all-tension and all-compression compliance matrices. How these matrices are found is determined by which multimodulus approach is used. For the same material, fewer material properties are required in the RCM than in the WCM because relationships exist in the RCM between the all-tension and the all-compression compliances. The compliance matrices for the tensile and compressive stress states are then transformed to principal stress directions. Next, the composition of the multimodulus compliance matrix is determined by use of the signs of the principal stresses. The multimodulus compliance matrix is obtained from the transformed tensile and compressive compliance matrices by

either the weighted compliance or restricted compliance approach. Upon definition of a multimodulus compliance matrix, the stresses, strains, and strain energies are reevaluated. The loop from the calculation of new material properties to the computation of stresses, strains, and strain energies is repeated until the convergence criterion is satisfied.

Convergence is achieved in the linear multimodulus model developed by Jones [22, 24] when, on successive iterations, the absolute value of the relative change in magnitude of each significant stress is less than or equal to a specified value. The word "significant" denotes that the absolute value of the stress is large compared to the summation of the absolute values of all the stresses. For example, consider the axisymmetric loading of an axisymmetric body. The stress σ_r is "significant" if

$$\left| \frac{\sigma_r}{\sigma_a} \right| > .0001 \quad (26)$$

where

$$\sigma_a = |\sigma_r| + |\sigma_z| + |\sigma_\theta| + |\tau_{rz}| \quad (27)$$

Although such a convergence criterion has been demonstrated to be suitable for the linear multimodulus procedure, it would be ineffective as a convergence indicator of the present nonlinear procedure. Consider the example of Fig. 20 in which the stress is constant and only the strain varies on successive iterations. Convergence would be incorrectly indicated on the second iteration with the stress-based criterion since the stress is unchanged.

A convergence criterion based on the relative change in total strain energy is compatible with both a nonlinear and a multimodulus material model and, therefore, is used in nonlinear multimodulus material models. Whenever the absolute value of the relative change in total strain energy, $|\text{REL } \Delta U|$, between two iterations $i-1$ and i

$$|RFL \Delta U| = |(U_i - U_{i-1})/U_{i-1}| \quad (28)$$

becomes sufficiently small, then the iterative procedure terminates and convergence is assumed.

When the nonlinear multimodulus material models are used in finite element computer programs, convergence is defined in this report to occur when the convergence criterion is simultaneously satisfied by each element. A finite element problem with a large number of elements can require a substantial amount of computer time for each iteration. Thus, the nonlinear multimodulus procedures were specifically devised to obtain rapid convergence by considering both the nonlinear and multimodulus characters of the problem on the same iteration.

4.3 STRAIN ENERGY FUNCTIONS

For the nonlinear multimodulus material models, three different energy functions are investigated: total strain energy, divided strain energy, and weighted strain energy. Each of these functions will be discussed briefly. The strain energies used in the material models are actually strain energy densities. Although the word density is frequently omitted, the strain energies are always understood to be on a unit volume basis.

The total strain energy defined in Eq. (4) can be used to determine all material properties in each iteration as is done in the nonlinear model of Section 2. Thus, application of the total energy function is the same for both the nonlinear material model and the nonlinear multimodulus material models.

In the divided energy approach, the total strain energy is separated into two components: (1) the contribution from the tensile principal stresses and (2) the contribution from the compressive principal stresses. These two components are not invariant under rotation of coordinates and are defined only in principal stress coordinates. However, their sum, the total strain energy,

is invariant with respect to coordinate transformations. In the divided energy approach, the tensile component of strain energy is used to determine the tensile material properties, and the compressive component of strain energy is used to determine the compressive material properties.

Different nonlinear stress-strain response in uniaxial tension and in uniaxial compression for ATJ-S graphite was found by Jortner [30]. The different deformation behavior under tensile and compressive loads might be related, at least in part, to a microcracking phenomenon (to which plastic volume changes have also been attributed). In the nonlinear multimodulus material models, multiaxial stress states are related to the material properties defined in uniaxial stress states by a strain energy function. The relationship between strain energy and material properties might be expected to be dependent on the signs of the multiaxial principal stresses. The division of energy is a mechanism used to investigate such a dependency.

In the weighted energy approach, the effective energy level in terms of the tensile and compressive components of the total strain energy density is

$$U_w = \left(\frac{U_c}{U} \right)^n U_c + \left[1 - \left(\frac{U_c}{U} \right)^n \right] U_t \quad (29)$$

where

n = a positive integer constant

U = total strain energy

U_c = strain energy of compressive stresses

U_t = strain energy of tensile stresses

U_w = weighted energy

This energy level, U_w , is used to find both the tensile and the compressive material properties. Thus, this approach is more desirable than the divided energy method from the standpoint that a consistent energy level is used to determine the current values of all material properties. When $n=1$ in Eq. (29),

the weighted energy density varies between the average and the sum of U_t and U_c as a function of the ratio U_c/U . This variation is shown in Fig. 31 along with the variation for $n=2$. When $n=1$, the variation is symmetrical about $U_c/U=.5$. On the other hand, for $n=2$, the weighted energy density is larger when $(U_c:U_t) = (1:9)$ than when $(U_c:U_t) = (9:1)$. When the weighted energy is used in the comparisons between predicted and measured strains, n is always unity.

4.4 NONLINEAR WEIGHTED COMPLIANCE MATERIAL MODEL

Three aspects of the nonlinear weighted compliance material model (WCM) are discussed: (1) the distinctive features of the iteration approach, (2) the restrictions imposed on the stress-strain behavior that can be treated with the model, and (3) the computerized application of the material model.

Two steps in the general nonlinear multimodulus procedure outlined in Fig. 30 are dependent on which multimodulus procedure is used. The first step is the evaluation of the all-tension and all-compression compliance matrices. The elements of these matrices are determined from the material properties by the same expressions in both the linear and nonlinear multimodulus approaches. In the linear approach of Section 3.2, the material properties are constant. However, in the nonlinear approach, the material properties are functions of the strain energy. The second step which depends on the multimodulus procedure is the computation of the multimodulus compliance matrix. This step is identical in both the linear and the nonlinear weighted compliance material models.

When the linear multimodulus approach of Section 3.2 is combined with the nonlinear approach of Section 2, restrictions are placed on the deformation behavior of the material that can be treated. As with the nonlinear material model of Section 2, the reciprocal relations, Eq. (3), between material properties are assumed to be valid when all material properties are evaluated at the

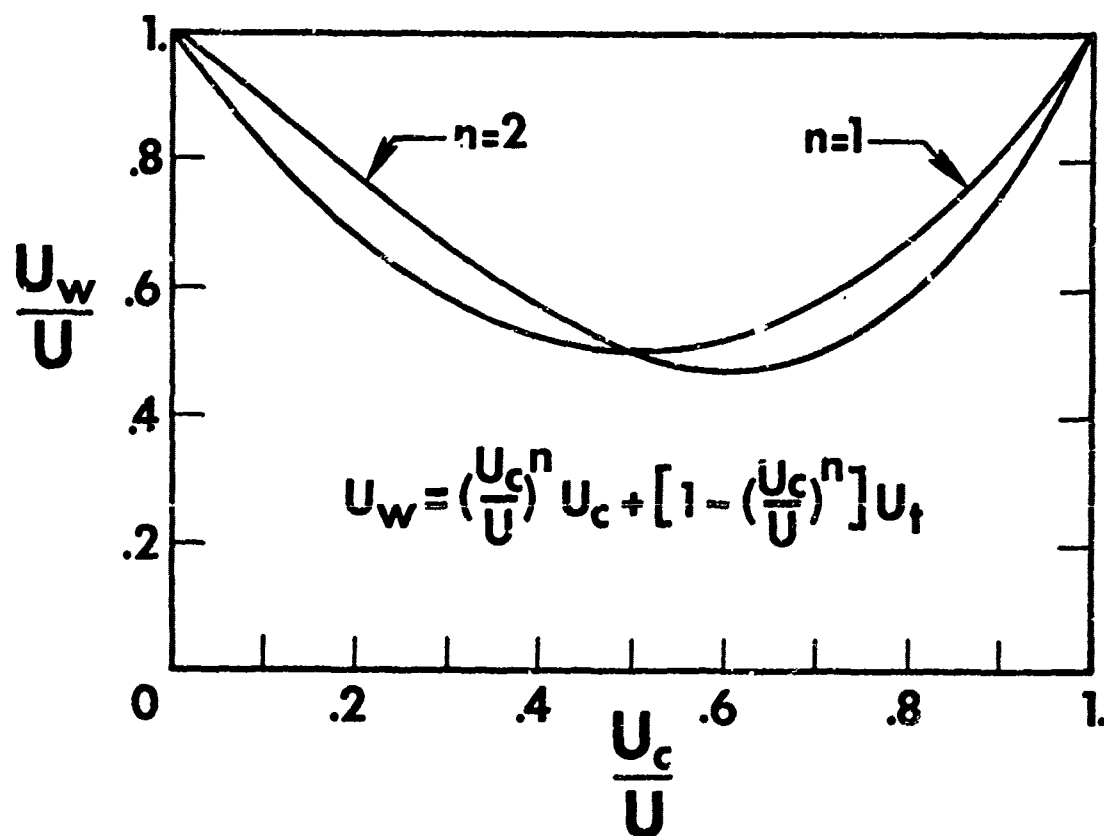


FIGURE 31 VARIATION OF WEIGHTED STRAIN ENERGY

same energy level. Reciprocal relations exist for both tensile and compressive properties in the multimodulus problem. Symmetry of the multimodulus compliance matrix in each iteration is ensured in the nonlinear WCM by weighting factors used in the development of the multimodulus compliance matrix, not by relationships between tensile and compressive material properties as will be done in the RCM. Thus, with the nonlinear weighted compliance material model, fewer restrictions are placed on the stress-strain behavior that can be treated. However, in the application of the nonlinear WCM, a greater number of independent tensile and compressive material properties are required than for the nonlinear RCM. Also, due to the independence of tensile and compressive compliances, restriction on the material's behavior from the reciprocal relations are the same for all three energy functions.

A short computer program, MULTIW, was written to investigate the weighted compliance model for all three energy functions. MULTIW is limited in capability to the prediction of strains from an input uniform stress state. However, MULTIW has a degree of generality compatible with the material models in a modified version of the SAAS III finite element program. The stress-strain relations in MULTIW can be applied to an axisymmetric body under axisymmetric load as well as to more general stress states for isotropic, transversely isotropic, and orthotropic materials. For the latter two levels of anisotropy, the principal material (x, y, z) directions in Fig. 32 can exist at arbitrary orientations in the $y-z$ plane to the input stress (x', y', z') directions. Because the input stresses are constant, the principal stresses and their orientations do not vary from one iteration to the next. This program will be used in the off-axis strain response studies and the biaxial strain response studies of Sections 5 and 6, respectively.

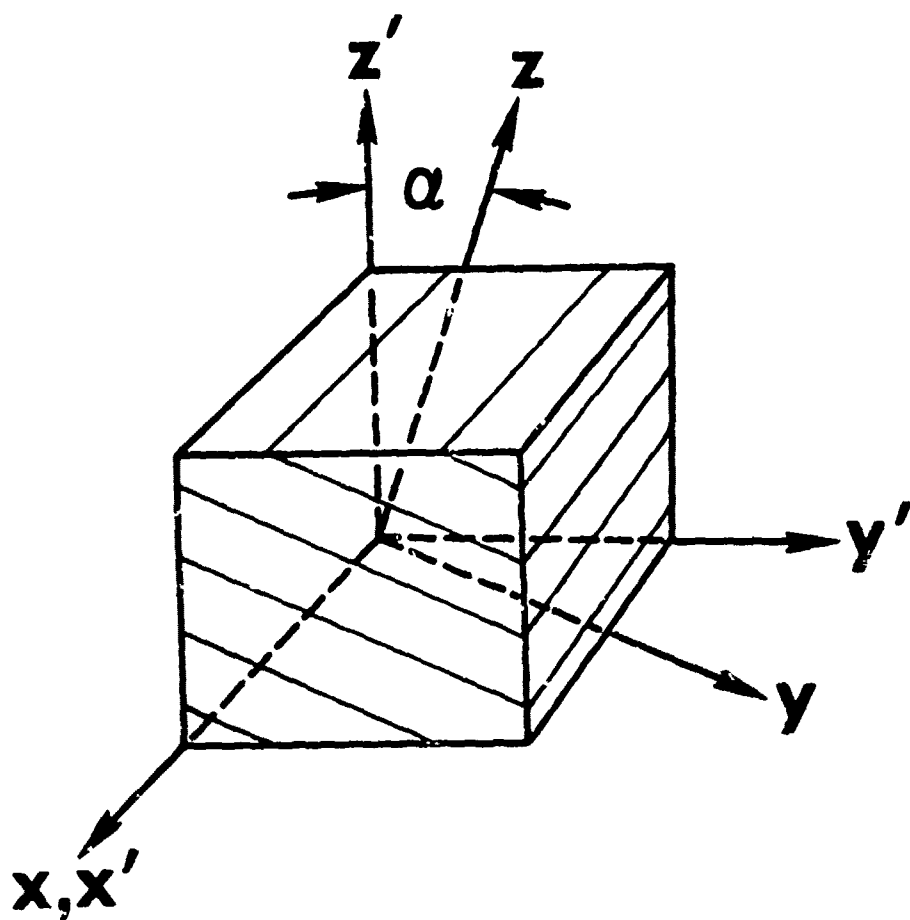


FIGURE 32 PRINCIPAL MATERIAL (x, y, z) DIRECTIONS
VERSUS LOAD (x', y', z') DIRECTIONS

4.5 NONLINEAR RESTRICTED COMPLIANCE MATERIAL MODEL

Three aspects of the nonlinear restricted compliance material model (RCM) are discussed: (1) the distinctive features of the iteration approach, (2) the restrictions imposed on the stress-strain behavior that can be treated with the model, and (3) the computerized application of the material model.

Only two steps in the general iteration procedure described in Section 4.2 are affected by which multimodulus procedure is used. These steps involve the evaluation of the all-tension and all-compression compliance matrices in principal material coordinates and the evaluation of the multimodulus compliance matrix in principal stress directions. The linear multimodulus approach outlined in Section 3.3 is used to develop these compliance matrices for the nonlinear restricted compliance material model. In this approach, the symmetry of the compliance matrices about the main diagonal in all coordinate systems is ensured by the relation between the material properties determined in uniaxial tension and uniaxial compression. On each iteration of the nonlinear procedure, an equivalent linear (elastic) system is considered. The requirement of symmetry of the compliance matrix is then related to the existence of a potential function for such a system.

The main difference between the linear and the nonlinear RCM is the variation of material properties with strain energy. For the linear material model, all the input tensile and compressive material properties are constant. Therefore, the multimodulus compliance matrix is affected only by the signs of the principal stresses, not their magnitudes. In the nonlinear multimodulus material model, the material properties used to define the all-tension and all-compression compliance matrices are functions of the strain energy. In the first iteration, the linear tensile material properties are used to predict the stresses and strains. However, in subsequent iterations, the current value of

the strain energy (or energies in the case of the divided energy) is used to determine the material properties in the stress-strain relationship.

For the total or weighted energy approaches, the relationships between material properties are implied to be valid when all the material properties are evaluated at the same strain energy. Thus, restrictions are placed on the uniaxial stress-strain behavior that can be treated with the models. That is, not all materials have properties for which the material model restrictions are satisfied.

Even more restrictions are imposed on the deformation behavior of the material being investigated if the divided energy approach is used. In the nonlinear RCM, the off-diagonal compliances in corresponding positions of the all-tension and all-compression compliance matrices are required to be identical at the same energy level. (This requirement may lead to limited applicability of the model.) If the divided energy approach were used, these off-diagonal compliances would have to be constant for all energy levels. A cube of an isotropic multimodulus material loaded only in two orthogonal directions by equal tensile forces can be used to illustrate the constancy requirement of the off-diagonal compliances. Suppose two of the three independent material properties for a nonlinear multimodulus isotropic material were determined in compression (despite the fact that we deal with an all-tension stress state). Then, the two compression properties would be used to evaluate all the nonzero off-diagonal compliances. The compression component of the total strain energy would be used to find the current value of the two compression properties. Because the compression component of total strain energy would always be zero, these compliances are constant. Thus, if the material is to satisfy the relation

$$\frac{\nu_t}{E_t} = \frac{\nu_c}{E_c} \quad (30)$$

at all energy levels, the material property expressions for the Young's modulus and Poisson's ratio in tension could differ at most in the constant A. Therefore, the applicability of the nonlinear RCM to actual deformation behavior must be assessed by examining whether (or how well) the relations between tensile and compressive compliances are satisfied.

A short computer program, MULTIR, was written to investigate the restricted compliance material model for all three energy functions. This program is identical in form to the MULTIW computer program described in Section 4.4 for the weighted compliance material model. All comments on the general character of the MULTIW program are also applicable to the MULTIR program. Both programs will be used in the off-axis strain response studies and the biaxial strain response studies of Sections 5 and 6, respectively.

4.6 SUMMARY

The nonlinear material model in Section 2 is combined with each of the linear multimodulus material models in Section 3 to obtain the two nonlinear multimodulus material models which are described in this Section. The use of three different energy functions is investigated for both of the two models. Restrictions on the stress-strain behavior that can be treated are discussed.

The actual stress-strain behavior of a nonlinear multimodulus material would probably have the general form of the dashed curve in Fig. 5. In the linear multimodulus models, a bilinear approximation of the actual stress-strain behavior is used. This bilinear approximation is represented by the solid lines in Fig. 5. The discontinuity in slope at the origin for the bilinear approximation would probably not occur for an actual material. Instead, a nonlinear transition region would be expected. This transition region can be represented with the nonlinear multimodulus material models by use of the

same value of the material property constant A , but different values of B and C , in the tension and compression equations for a material property. For problems in which the stress-strain behavior in the transition region is not important, a better representation of the actual material property-strain energy variations might be achieved with different values of A in the tension and compression equations for a material property.

The applicability and accuracy of the nonlinear multimodulus material models are investigated in the off-axis strain response and biaxial strain response studies of Sections 5 and 6, respectively.

5. COMPARISON OF PREDICTED AND MEASURED STRAIN RESPONSE UNDER UNIAXIAL OFF-AXIS LOADING

5.1 INTRODUCTION

The two nonlinear multimodulus material models described in Section 4 are used to predict the uniaxial deformation behavior of ATJ-S graphite when the load is applied at an angle α to the principal material directions (see Fig.32). These predictions are compared to the strain response measured by Jortner [30]. The comparisons between predicted and measured strains are used to evaluate how well the uniaxial deformation behavior can be predicted when (1) the load is applied in the principal material directions and (2) the load is applied in other than principal material directions. In addition, the application of the models and, to some extent, the contrast between them is demonstrated.

Before presentation and discussion of the predicted and measured strain results, the pertinent features of the test specimens and the test procedures are described.

5.2 DESCRIPTION OF TEST SPECIMENS AND PROCEDURES

The off-axis specimens were obtained from ATJ-S graphite billet 16K9-27 by the scheme shown in Figs. 33-35. The nominal directions of the planes of isotropy of the transversely isotropic material are identified with light lines. The billet cylindrical coordinate system, shown in Fig. 33, is nominally aligned with the principal material directions. That is, the principal material directions are not necessarily the same throughout the billet because of nonuniformities, e.g., nonuniform compaction or nonuniform particle-binder mixture, in the billet manufacturing process. The 6-in. long tension test specimens with a 1/4-in. square gage section were cut from two of the slabs from the billet as schematically shown in Fig. 34. The 2-in. long compression test specimens,

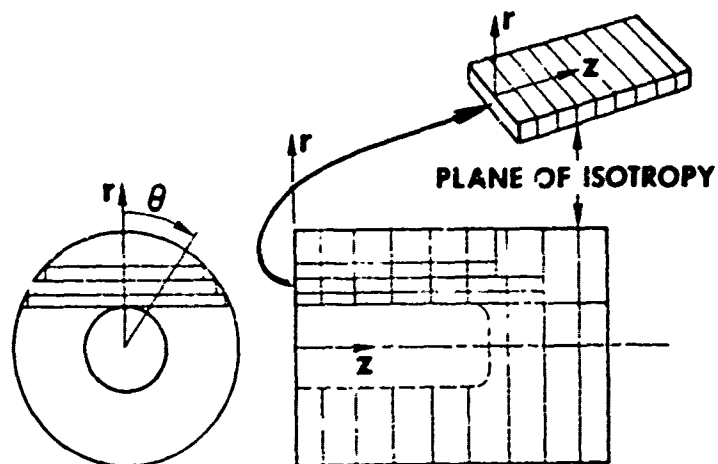


FIGURE 33 RELATION OF TEST SPECIMEN SLABS TO BILLET

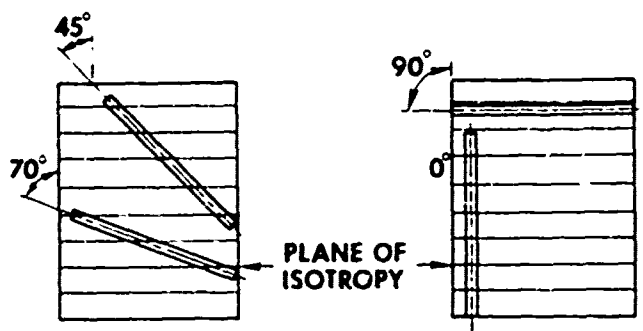


FIGURE 34 RELATION OF TENSION SPECIMENS TO SLAB

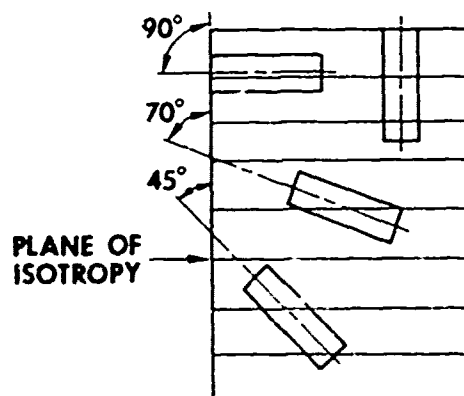


FIGURE 35 RELATION OF COMPRESSION SPECIMENS TO SLAB

which were of the characteristic dogbone shape, have a 1/2-inch diameter cylindrical gage section. These compression specimens were cut from a slab of the billet as schematically shown in Fig. 35. At least three tension and compression test specimens were cut from the slabs at each of four angular orientations, 0° , 45° , 70° , and 90° , from principal material directions.

The positions of the axial and transverse strain gages on the gage section of the tension and compression specimens are indicated in Figs. 36 and 37. The figures are not adequate for precise definition of the instrumentation of each specimen. (A detailed description of the strain gages on each specimen is given in Tables XIII and XIV of Ref. 1.) However, sufficient information is in Figs. 36 and 37 for consistent comparison of predicted and measured strains.

The (x' - y' - z') coordinate system used in the presentation of strain results is shown in Figs. 36 and 37. Note that the x - y - z coordinate system is aligned with the nominal principal material directions of the material and that the x and y coordinates are in the plane of isotropy of the material. The angle μ is the angle in the y - z plane between the load axis (z') and the across grain (z) principal material direction. For example, the specimen is loaded uniaxially in the across grain (z) direction when $\mu = 0^\circ$ and in the with grain (y) direction when $\mu = 90^\circ$. Strains were always measured in the x' - y' - z' coordinate directions.

Acoustic velocity measurements and shear coupling effects on the specimens are reported by Jortner [7]. Acoustic velocity measurements were made to determine variations between local and nominal principal material directions due to billet nonuniformities. As a result of this investigation, Jortner speculates that, for the 45° tension specimens and the 70° compression specimens, the angles between principal material and load directions may be closer to 40° and 80° , respectively. Analytical studies of shear coupling effects on the stress

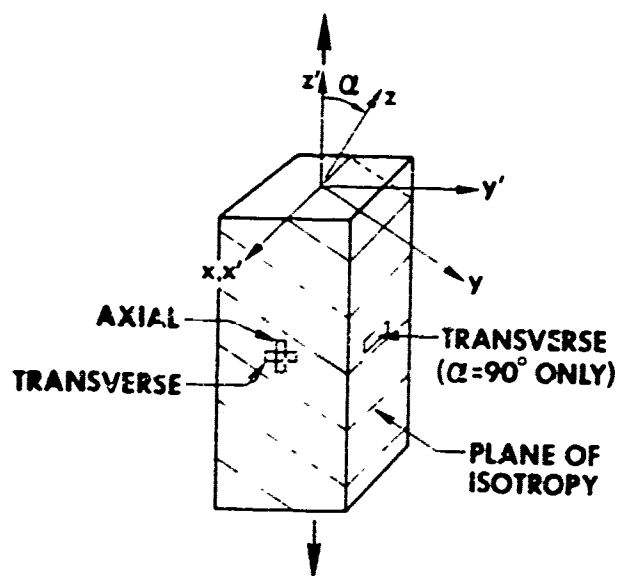


FIGURE 36 TENSION BAR GAGE SECTION

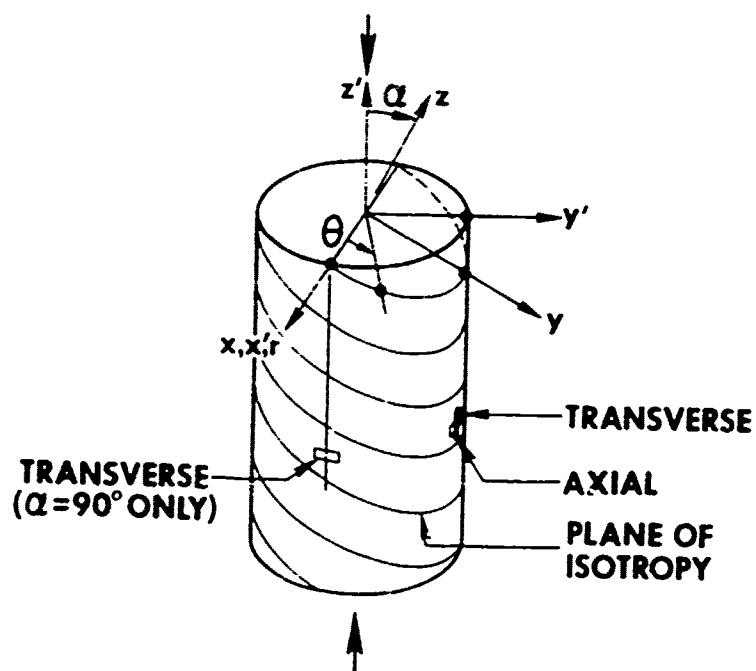


FIGURE 37 COMPRESSION ROD GAGE SECTION

distributions in the off-axis specimens are also presented in Ref. 7. For both the tension and compression specimens, the effect of shear coupling on the stress distribution across the width of the gage sections is estimated to be small.

The specimens were loaded on an Instron test machine. The load was introduced in the tension specimens with doublers bonded to the specimens. These doublers were loaded through pin attachments. The compression specimens were loaded in a test fixture with an estimated friction-induced error in the recorded load of less than 2% [30].

5.3 COMPARISONS OF PREDICTED AND MEASURED STRAIN RESPONSE

Discussion of correlation between predicted and measured strain response is divided into five sections. In Section 5.3.1, the data base material properties are discussed. The general method used to present and compare the predicted and measured strain response under tensile and compressive loads is described in Section 5.3.2. The tensile strain correlations, which are the same for both the nonlinear WCM and RCM, are presented in Section 5.3.3. The compressive strain correlations are discussed for the nonlinear WCM in Section 5.3.4. Finally, the compressive strain correlations for the nonlinear RCM are described in Section 5.3.5.

5.3.1 Material Properties

The first step in application of the new material models in strain correlation studies is to develop a set of material property constants for the material property-strain energy equations from appropriate uniaxial test results. The material property constants used in the present strain correlations were determined directly from Fortner's experimental results [30]. Thus, extraneous

variations between predicted and measured strains are not introduced because of billet-to-billet variations in material properties or differences in test procedures. The material property constants in the billet coordinate system (principal material coordinates) are given in Table 8.

Different independent material properties are required for each of the two nonlinear multimodulus material models. For a transversely isotropic multimodulus material, six independent material properties are needed to apply the restricted compliance material model. The predictions of the RCM are dependent on which material properties are selected for the uniaxial baseline values. Of course, any set of six material properties could be used and the same predictions would result if the restrictions of the material model were perfectly satisfied by the stress-strain behavior of the material. For transversely isotropic multimodulus materials, ten independent material properties are required to apply the weighted compliance material model. The input material property sets investigated are:

Weighted Compliance Material Model

$$E_{rt}, E_{zt}, \nu_{r\theta t}, \nu_{z\theta t}, E'_{rzt},$$

$$E_{rc}, E_{zc}, \nu_{r\theta c}, \nu_{z\theta c}, E'_{rzc}$$

Restricted Compliance Material Model

$$\text{Property Set } E_{zc}: E_{rt}, E_{zt}, \nu_{r\theta t}, \nu_{z\theta t}, E'_{rzt}, E_{zc}$$

$$\text{Property Set } E_{rc}: E_{rt}, E_{zt}, \nu_{r\theta t}, \nu_{r\theta t}, E'_{rzt}, E_{rc}$$

5.3.2 Method of Presentation of Results

Strain predictions with the new material models are shown in Figs. 38-53 as symbols next to the curves for experimental results. The experimental results were obtained from Jortner's Figs. 4 thru 7 and 9 thru 12 [30]. The predicted strains were obtained with the MULTIR and MULTIW computer programs.

TABLE 8 CONSTANTS IN MATERIAL PROPERTY EQUATIONS FOR
16K9 BILLET DATA BASE* AT 70°F

MATERIAL PROPERTY	A	B	C	U_0
E_{rt}	$1.72 \times 10^6 \text{ psi}$.101576	.445843	1 psi ↓
E_{zt}	$1.37 \times 10^6 \text{ psi}$.231769	.255095	
ν_{ret}	.1	.376247	.169649	
ν_{zet}	.1607	.445588	.157836	
E'_{rzt}	$1.385 \times 10^6 \text{ psi}$.132548	.365323	
E_{rc}	$1.5152 \times 10^6 \text{ psi}$.0609584	.646868	
E_{zc}	$1.1538 \times 10^6 \text{ psi}$.140150	.370244	
ν_{rec}	.09	0	1	
ν_{zec}	.1	0	1	
E'_{rzc}	$1.2626 \times 10^6 \text{ psi}$.122519	.394504	

*Experimental Data Due to Jortner [30], Figs. 4, 5, 7, 9, 10, and 12

Because a portion of the experimental results was used to develop the material property constants input to these computer programs, different categories of strain predictions must be discussed. The material property constants were determined by a simultaneous solution technique from data at three points on the experimental curves. Predictions of strains for these data base points are indicated with dots (filled-in circles), whereas other predictions of the material model are indicated with open circles. All the predictions along stress-strain curves used to define material property-strain energy relationships are distinguished from other predictions by the appearance of the material property designation next to its defining curve. For example, the experimental results in Fig. 38 were used to define the constants in the equation relating material properties E_{zt} and $\nu_{z\theta t}$ to the strain energy. Predictions for the actual points used in the derivation of the material property constants are indicated with dots.

In the discussion of results, approximate percentage differences between predicted and measured strains are computed from

$$\Delta\epsilon = \frac{\epsilon_{\text{Predicted}} - \epsilon_{\text{Measured}}}{\epsilon_{\text{Measured}}} \times 100\% \quad (31)$$

When more than one experimental curve is presented for stress-strain behavior other than data base behavior (curves used to compute the material property constants), the percentage differences are calculated between the predicted value and the closest experimental results (a minor bias). For example, the percentage difference for the transverse strain prediction in Fig. 39 at 4000 psi would be computed with the strain from the left-most experimental curve. When the prediction falls between experimental curves, the percentage differences are regarded as zero.

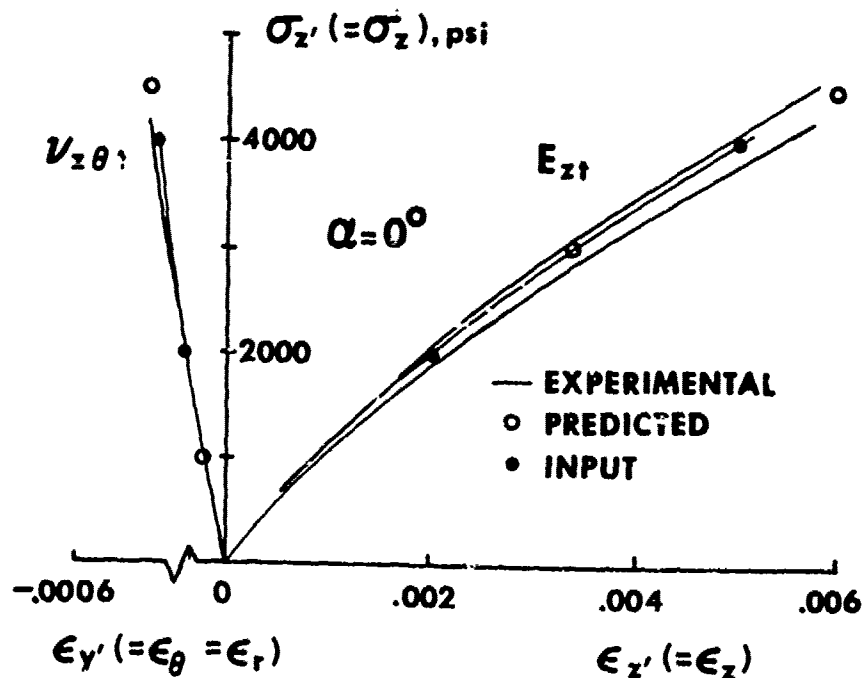


FIGURE 38 OFF-AXIS BEHAVIOR - TENSION, $\alpha=0^\circ$

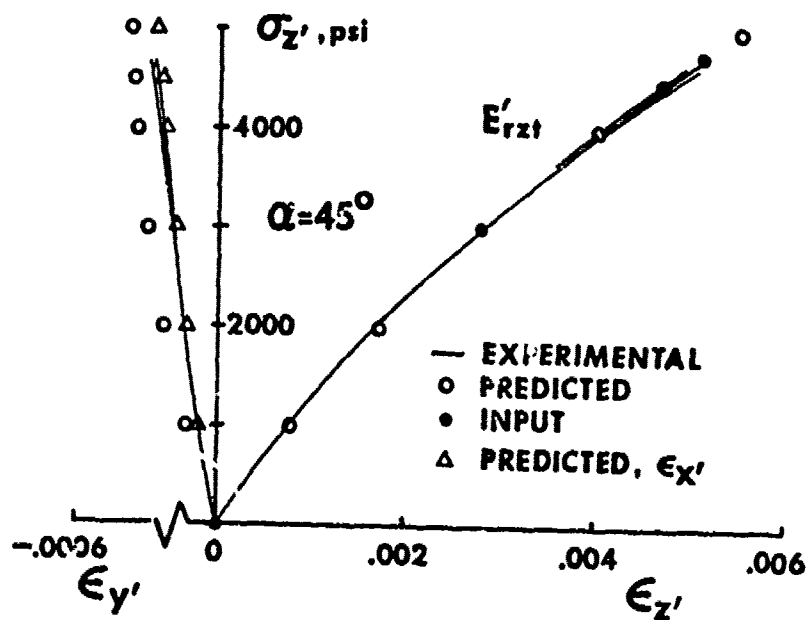


FIGURE 39 OFF-AXIS BEHAVIOR - TENSION, $\alpha=45^\circ$

5.3.3 Tensile Strain Correlations

The predictions with both material models for each of the three energy approaches are identical for the tension loading cases in Figs. 38-41. The predictions are identical because of the formulations of the two material models and the use of five tension properties in both property sets for the restricted compliance material model. The curves used to define the material property-strain energy relationships for the five tension properties common to all three property sets (WCM and both RCM) are shown in Figs. 38, 39, and 41. The largest variation between predicted and measured strains which occurs for a curve used to establish a direct moduli-strain energy relationship is 5%. The predictions for curves in Figs. 38 and 41 which were used to determine material property constants for ν_{zet} and ν_{ret} , respectively, show equally good (within about 5%) correlation except for the 1000 psi and 2000 psi stress level predictions in Fig. 41. The strains predicted for 1000 and 2000 psi stress levels differ from the measured strains for the ν_{ret} curve by -19% and -14%, respectively. These variations are not considered significant because they occur at low strain levels which are generally not critical in structural design analysis. Variations between predicted and measured strains for 1000 psi and 2000 psi stress states on the ν_{ret} curve might be attributed to a poor approximation of the material property-strain energy relationships at low energy levels. A low-fit approximation as shown in Fig. 22 might result in improved strain correlation for these low stress levels. A visual inspection of the strain correlations for the ν_{ret} curve in Fig. 41 reveals that the variations at 1000 psi and 2000 psi are not of practical importance because the strains themselves are quite small. The use of $|\text{REL } \Delta U| = .5\%$ as a convergence test value in the MULTIR and MULTIW computer programs is supported by the excellent strain correlations found for the input data points (filled-in circles) shown in Figs. 38, 39, and

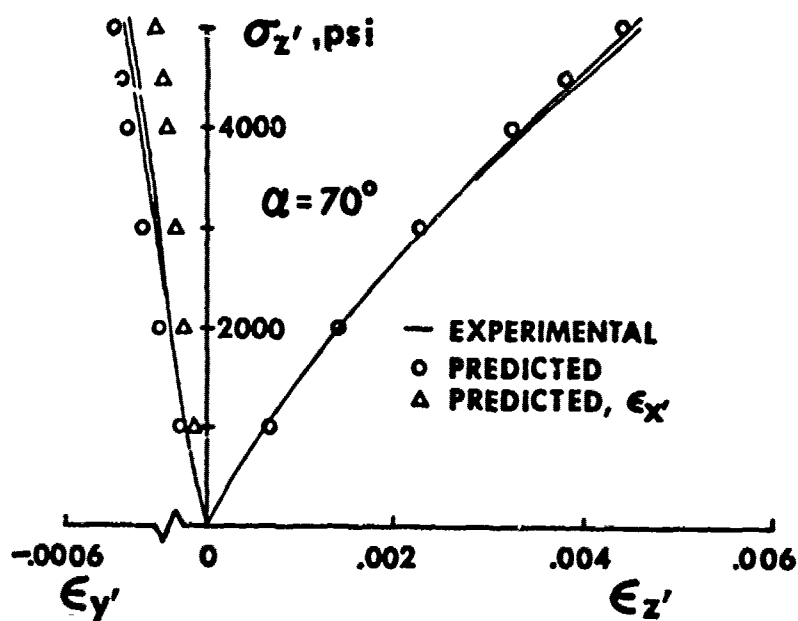


FIGURE 40 OFF-AXIS BEHAVIOR - TENSION, $\alpha=70^\circ$

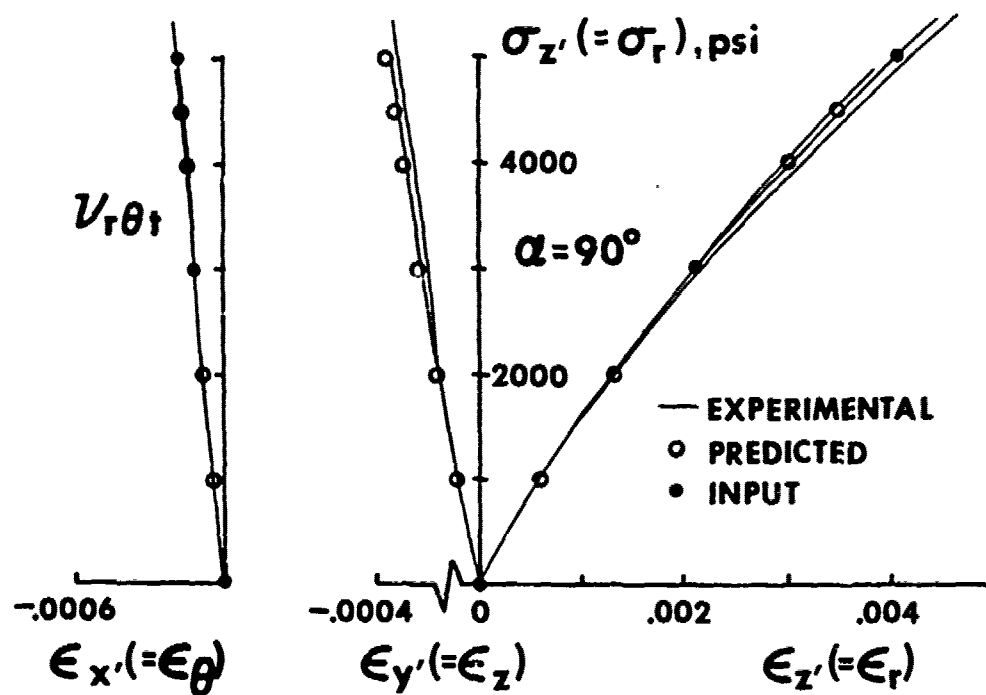


FIGURE 41 OFF-AXIS BEHAVIOR - TENSION, $\alpha=90^\circ$

41. Good strain correlations are found for the predictions (open circles) of points on the curves used to evaluate the material property constants for the five tension properties. Thus, the general material property equation, Eq. (5), can be used to represent the material property-strain energy variations for the tension material properties of ATJ-S graphite at 70°F. The simultaneous solution procedure used to evaluate the material property constants B and C is also generally substantiated by the comparisons.

Four sets of strain correlations for the tensile loads are not directly associated with input material properties: (1) transverse strain ϵ_y , at $\alpha=45^\circ$ (Fig. 39), (2) axial strain ϵ_z , at $\alpha=70^\circ$ (Fig. 40), (3) transverse strain ϵ_y , at $\alpha=70^\circ$ (Fig. 40), and (4) transverse strain ϵ_y , at $\alpha=90^\circ$ (Fig. 41). Good strain correlation was found for ϵ_z , at $\alpha=70^\circ$ and ϵ_y , at $\alpha=90^\circ$, whereas poor agreement between predicted and measured strains exists for ϵ_y , at $\alpha=45^\circ$ and 70° . Specifically, at 3000 psi, the predicted axial stress at $\alpha=70^\circ$ differs from the measured results by approximately 2%. The estimated percentage difference for the transverse strain ϵ_y , at $\alpha=90^\circ$ is 6%. The good agreement between the predicted and measured transverse strains ϵ_y , in Fig. 41 is an indication that the linear reciprocal relations between compliances are applicable to the nonlinear case. At a stress of 3000 psi, transverse strain predictions at $\alpha=45^\circ$ (Fig. 39) and $\alpha=70^\circ$ (Fig. 40) differ from the measured results by approximately 54% and 22%, respectively. No suitable explanation exists for the disparity between predicted and test values of the transverse strain at $\alpha=45^\circ$ and 70° . However, an anomalous feature of the $\alpha=45^\circ$ specimens, namely, a variation in orientation of the principal material directions, was uncovered in the acoustic velocity investigation. Also worthy of note is the fact that if the strain predictions for ϵ_x , are shown on Figs. 39 and 40, then the measured transverse strains are between the ϵ_x and ϵ_y predictions.

5.3.4 Compressive Strain Correlations for Nonlinear Weighted Compliance Model

The measured strains for specimens under uniaxial compression loads are shown with predictions from the nonlinear weighted compliance model in Figs. 42-45. For these loading conditions, the WCM predictions are identical for all energy approaches. In all instances, good correlation between predicted and measured strains is found. The largest percentage deviation at compressive stress levels with magnitudes greater than 3000 psi is 12% and occurs for the transverse strain at $\alpha=70^\circ$ (Fig. 44) at a stress of -5000 psi. This transverse strain correlation would be improved if α were regarded as 80° as found in the acoustic velocity investigation. The curves used to define the material property-strain energy relationships for the five independent compressive properties in the WCM data set are shown in Figs. 42, 43 and 45. The largest variation between predicted and measured strains which occurs for a curve used to find the material property constants is 8%. Thus, the general material property equation, Eq. (5), can be used to represent the material property-strain energy variations for the compression material properties of ATJ-S graphite at 70°F . The procedure used to evaluate the material property constants in the general equation is also substantiated by the results. Some of the deviation between the experimental axial strain curves in Fig. 42 (also Figs. 46 and 50) might be due to a calibration error for the lowest curve (Jortner [30] indicated a possible calibration error with a comment by the curve).

5.3.5 Compressive Strain Correlations for Nonlinear Restricted Compliance Model

The restricted compliance material model is applied for compressively loaded specimens to obtain the predicted results in Figs. 46-53. Results for material property sets E_{zc} and E_{rc} are displayed in Figs. 46-49 and Figs. 50-53, respectively. Recall that the two material property sets differ by only one

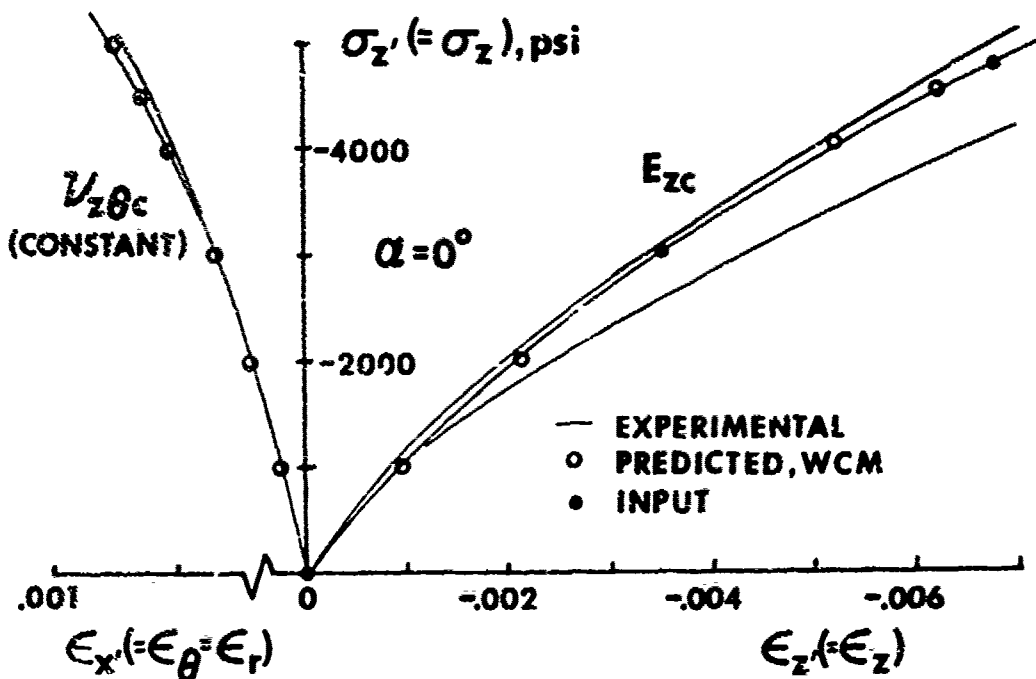


FIGURE 42 OFF-AXIS BEHAVIOR - COMPRESSION, $\alpha=0^\circ$, WCM

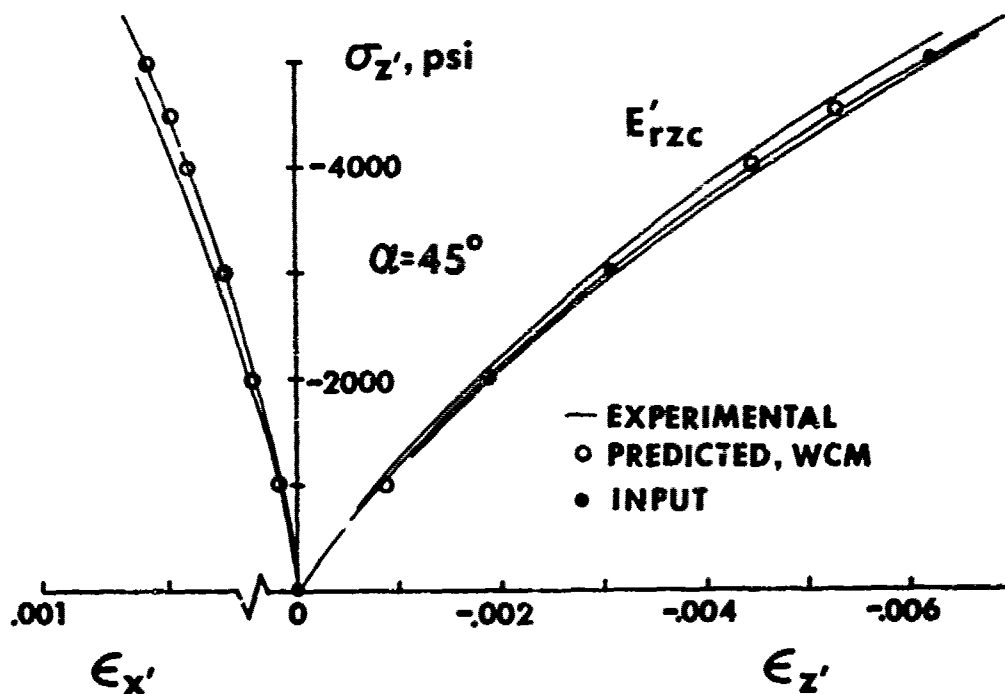


FIGURE 43 OFF-AXIS BEHAVIOR - COMPRESSION, $\alpha=45^\circ$, WCM

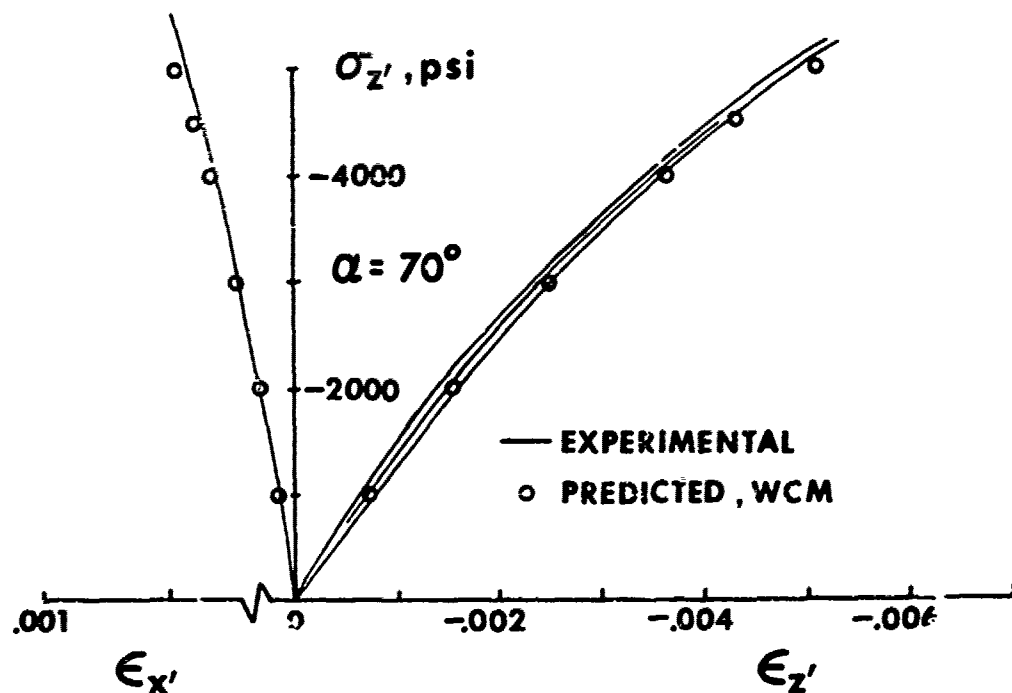


FIGURE 44 OFF-AXIS BEHAVIOR - COMPRESSION, $\alpha=70^\circ$, WCM

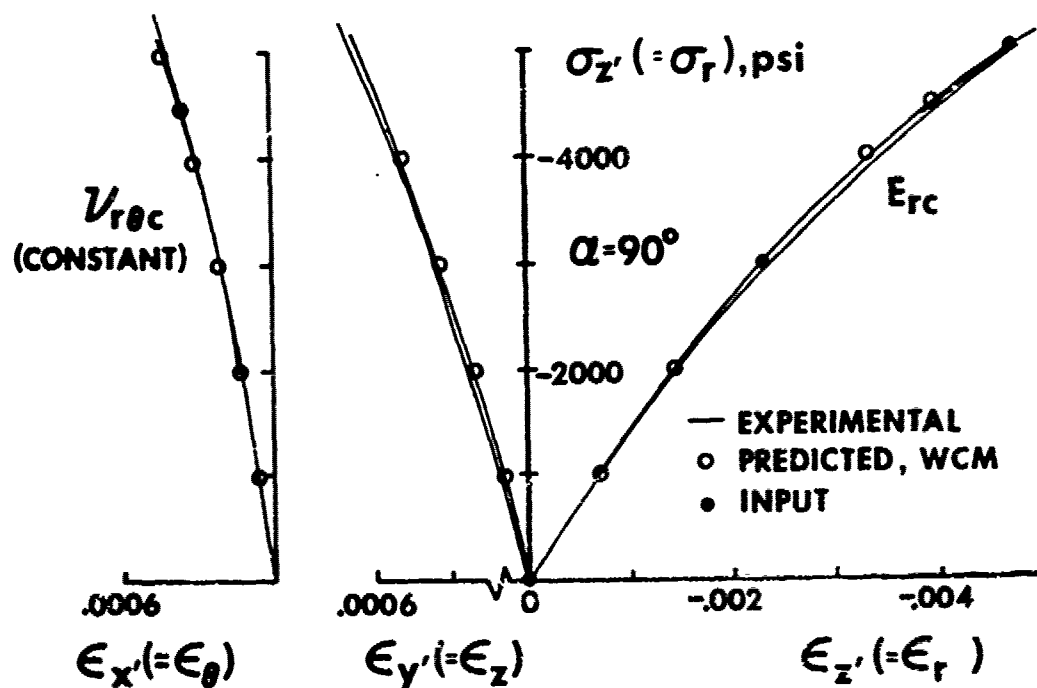


FIGURE 45 OFF-AXIS BEHAVIOR - COMPRESSION, $\alpha=90^\circ$, WCM

independent material property. The material property E_{zc} used in the first property set is replaced by E_{rc} in the second property set. All three energy approaches are investigated for material property set E_{zc} . Only the total energy approach is examined for the second property set E_{rc} . The dependence of the predictions of the RCM on the selection of the baseline material properties is demonstrated by the results. For example, at 5000 psi, the axial strain prediction for the total energy case in Fig. 46 is 12% smaller than the same prediction in Fig. 50. Similar deviations (8-10%) in axial strains occur when the predictions in Figs. 51, 52, and 53 are compared with the predictions in Figs. 47, 48, and 49, respectively. The differences in transverse strain predictions for the total energy approach with the two different property sets are small (less than 5%) because the off-diagonal compliances are determined from the same independent material properties (tension properties) in both cases. Differences in transverse strains predictions occur because the material properties are determined at different energy levels. Because the corresponding axial strain predictions with the different data sets are not the same, the relations between tension and compression compliances in the RCM may not be strictly applicable to ATJ-S graphite.

Although the axial strains in Figs. 46-49 agree relatively well (within 9%) with test results for the total and weighted energy approaches, the transverse strain correlation is generally poor. The largest deviation in axial strains, -9%, occurs for the $\alpha=90^\circ$ case (Fig. 49). At 5000 psi, all transverse strain predictions for the total and energy approaches in Figs. 46-49 differ from measured results by 44% to 55%. The relationships between diagonal compliances (direct moduli) for the all-tension and all-compression stress states in the nonlinear RCM might be applicable to ATJ-S graphite, but those between off-diagonal compliances (in which both direct moduli and Poisson's ratios

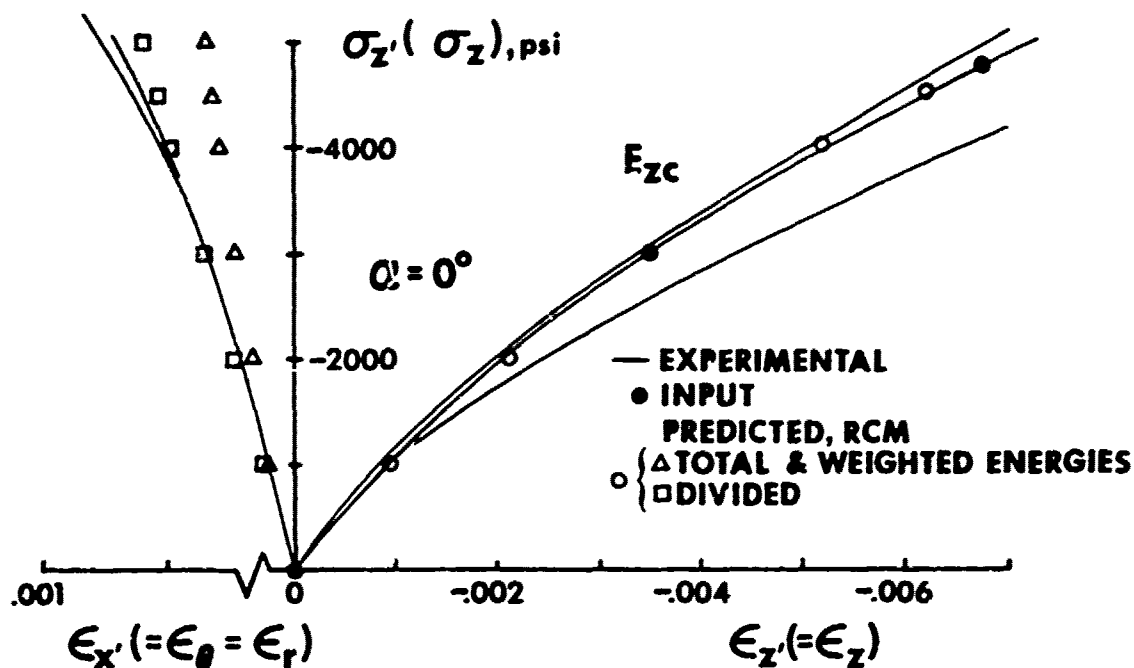


FIGURE 46 OFF-AXIS BEHAVIOR - COMPRESSION, $\alpha=0^\circ$, RCM, E_{zc}

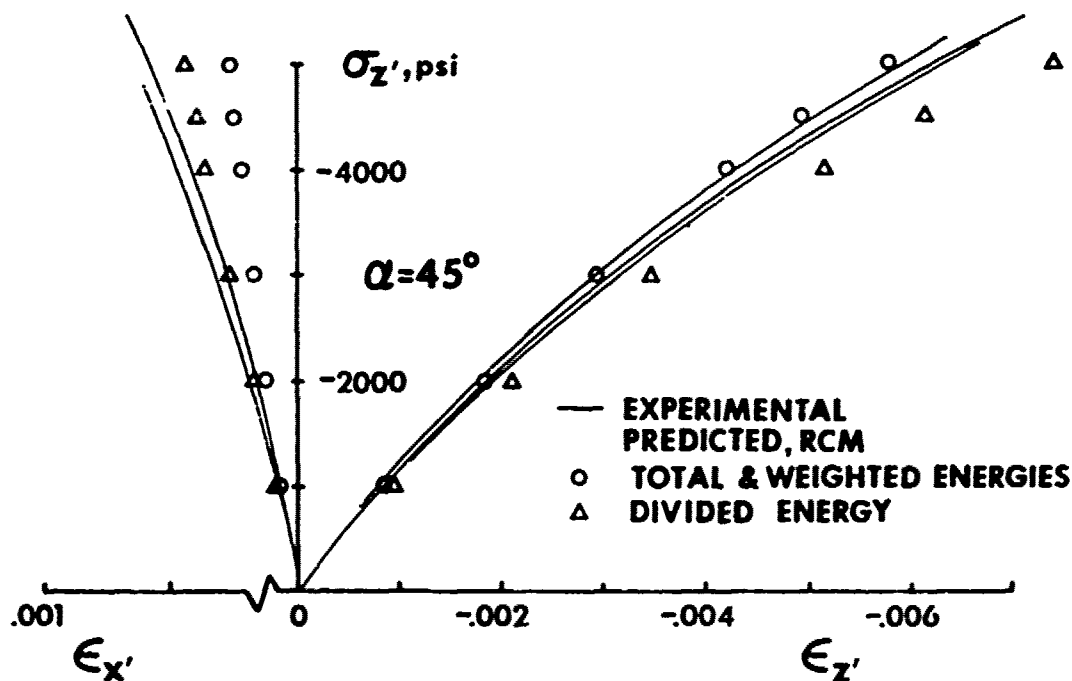


FIGURE 47 OFF-AXIS BEHAVIOR - COMPRESSION, $\alpha=45^\circ$, RCM, E_{zc}

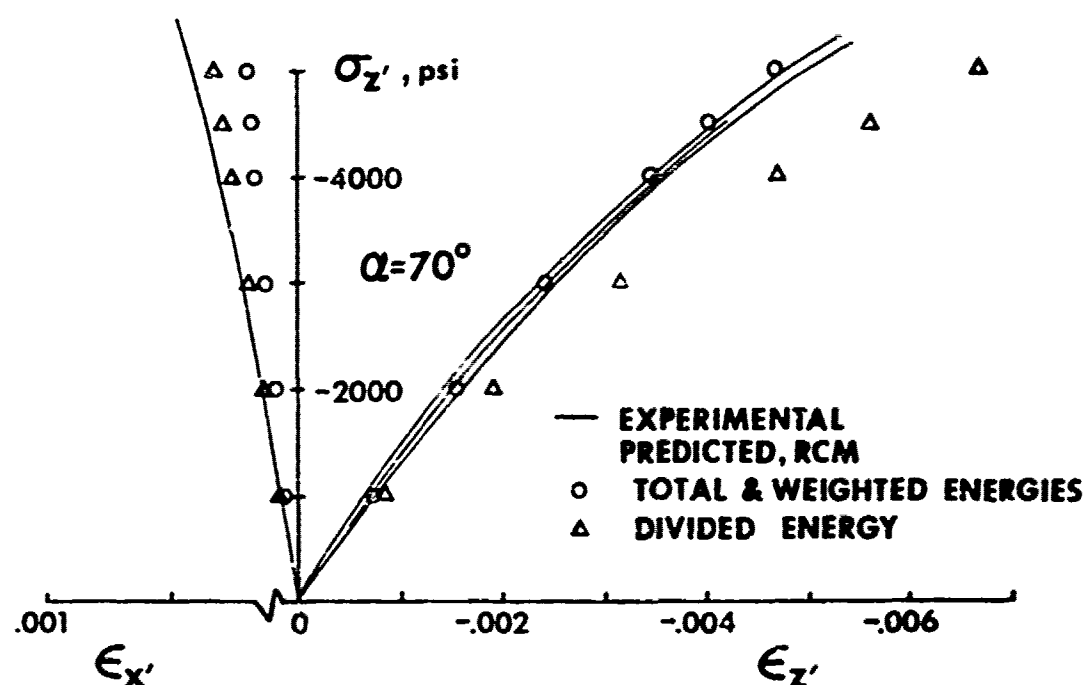


FIGURE 48 OFF-AXIS BEHAVIOR - COMPRESSION, $\alpha=70^\circ$, RCM, E_{zc}

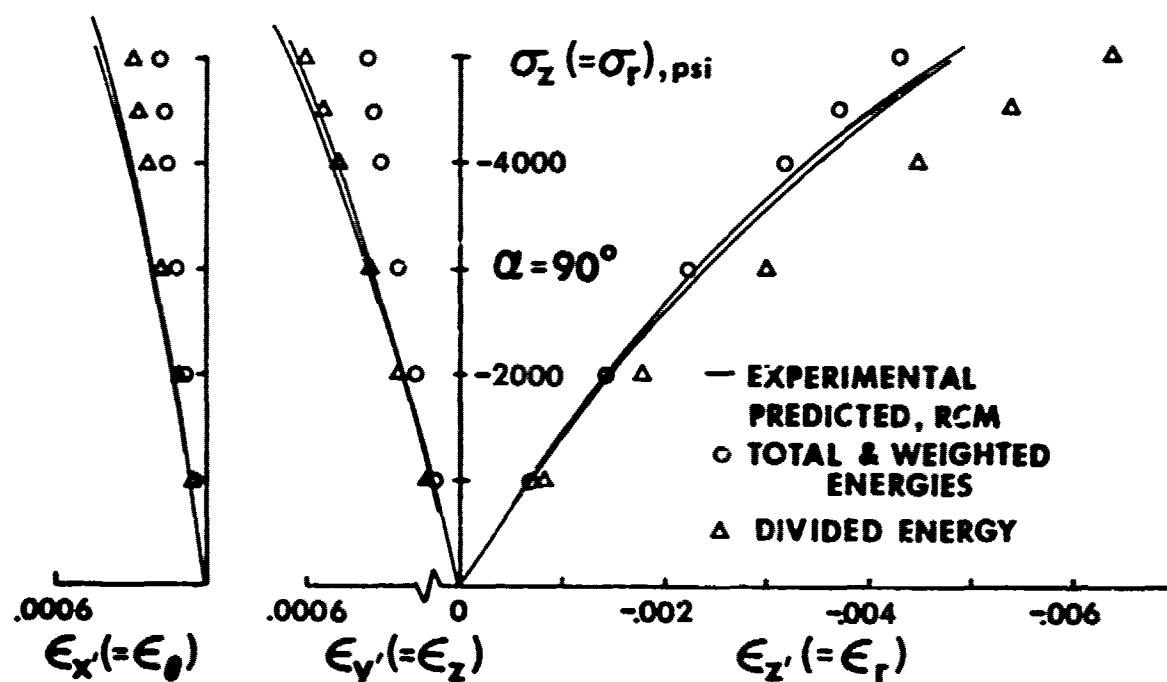


FIGURE 49 OFF-AXIS BEHAVIOR - COMPRESSION, $\alpha=90^\circ$, RCM, E_{zc}

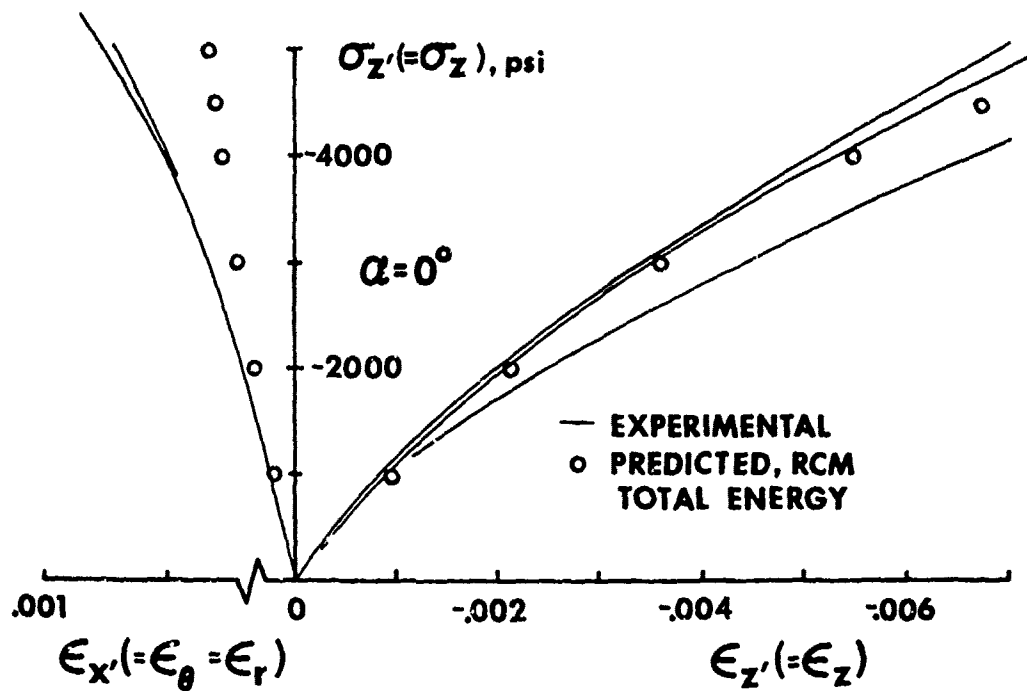


FIGURE 50 OFF-AXIS BEHAVIOR - COMPRESSION, $\alpha=0^\circ$, RCM, E_{rc}

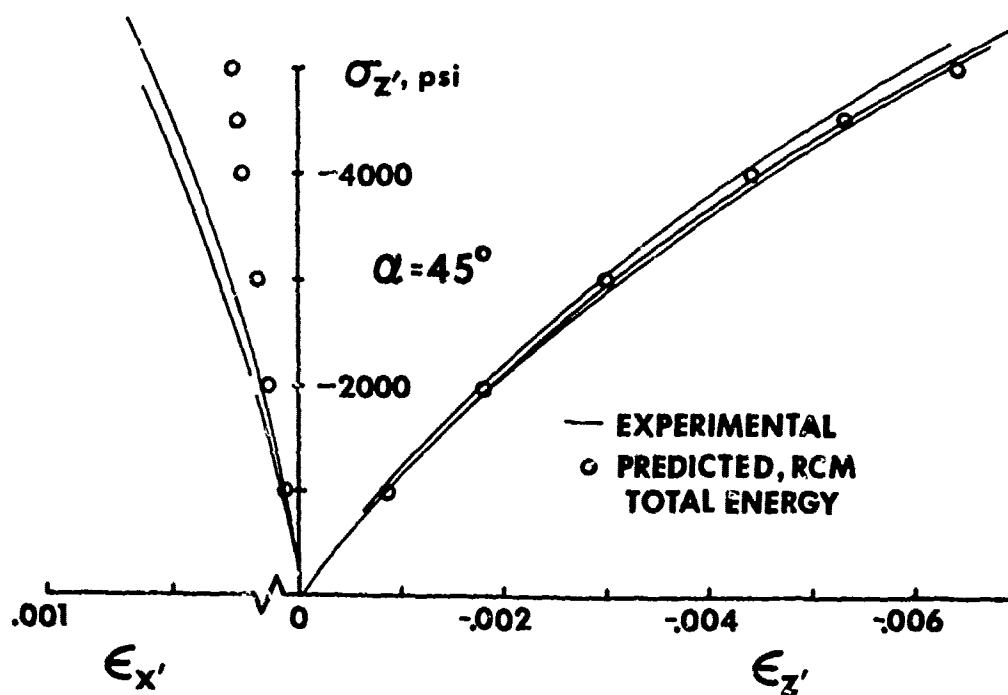


FIGURE 51 OFF-AXIS BEHAVIOR - COMPRESSION, $\alpha=45^\circ$, RCM, E_{rc}

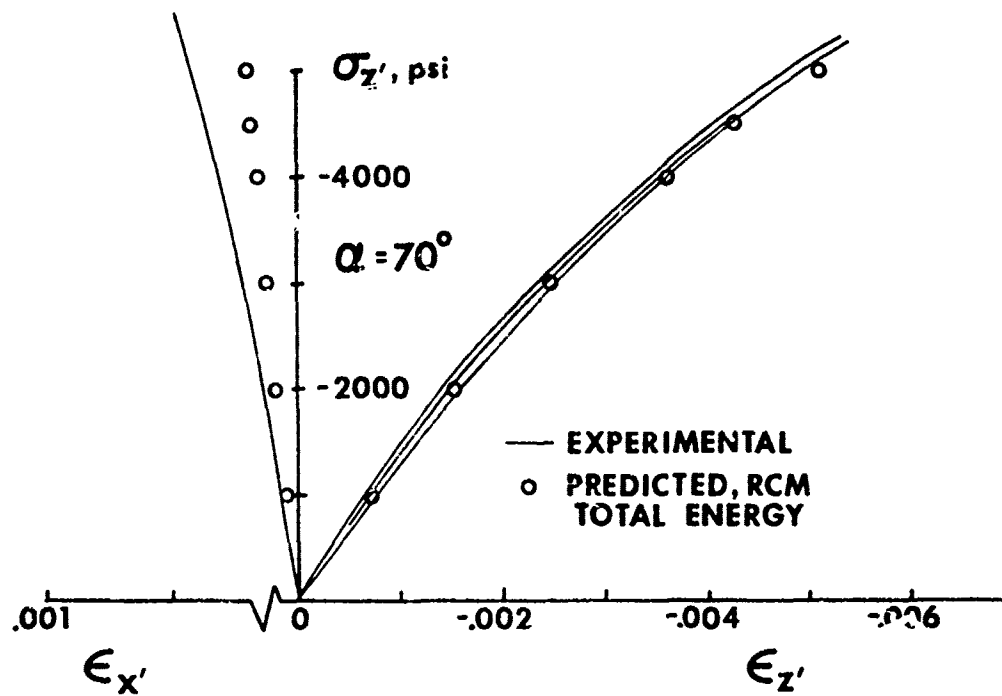


FIGURE 52 OFF-AXIS BEHAVIOR - COMPRESSION, $\alpha=70^\circ$, RCM, E_{rc}

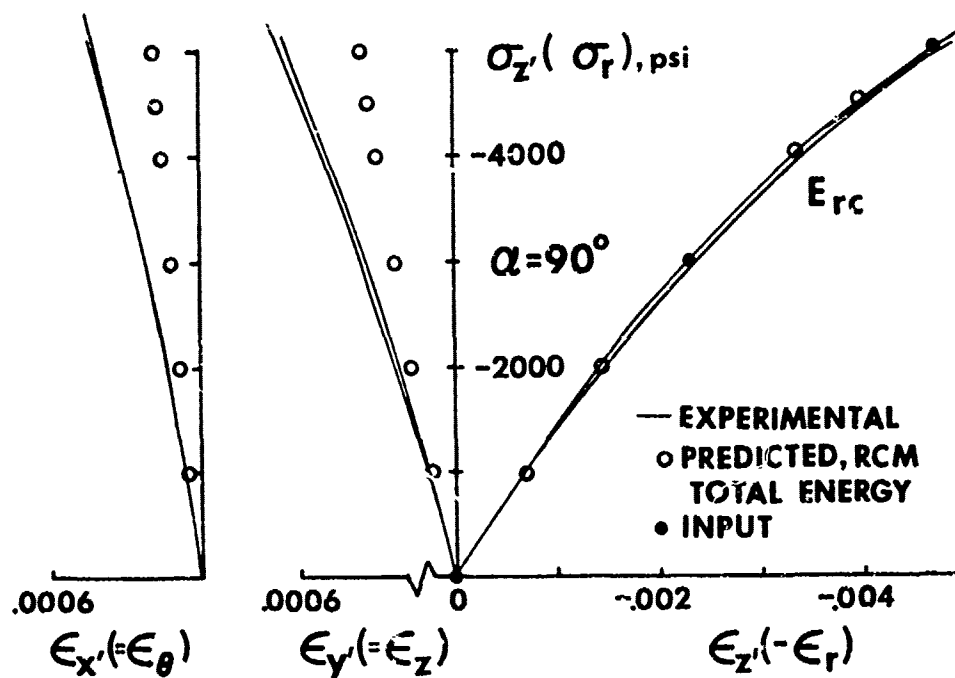


FIGURE 53 OFF-AXIS BEHAVIOR - COMPRESSION, $\alpha=90^\circ$, RCM, E_{rc}

appear) are not applicable. The restrictions on the off-diagonal compliances in the nonlinear RCM may be especially stringent for nonlinear stress-strain behavior of the material. When all material properties are evaluated at the same energy level, the compliance relationships should be valid. In the 70°F experimental results in Refs. 30 and 14, the tension Poisson's ratios generally decrease with increasing energy level, whereas Poisson's ratios in compression usually remain almost constant or increase. Thus, the variations for Poisson's ratios implied in the nonlinear RCM may not be representative of the actual variations. When the divided energy approach is used in the nonlinear RCM instead of the total or weighted energy approaches, the transverse strain correlation is somewhat improved (the largest deviation is about 28%), but the axial strain correlation is much poorer (the largest deviation is approximately 35%). With the divided energy approach, the implied off-diagonal compliances are constant on successive iterations for the loading and independent material properties investigated. The improved correlation for the transverse strain results from the larger strain predictions in the divided energy approach than in the total or weighted energy approaches. These predictions occur because the implied off-diagonal compliances remain constant instead of decreasing with increasing energy level. The implied diagonal compliances in the divided energy approach seem to be inappropriate because of the poor axial strain correlations.

5.4 SUMMARY

The strain predictions with both the nonlinear restricted compliance and weighted compliance material models are compared with the experimental strain response obtained from uniaxial loading of specimens with principal material directions at four different orientations with respect to the load axis. The best overall correlation between predicted and measured strains occurs for the

nonlinear weighted compliance material model. Note that the nonlinear weighted compliance material model results are the same for all energy approaches for these uniaxial stress conditions. That is, because the stresses are either all tension or all compression, the three energies used in each of the three energy approaches are identical. Moreover, the compliances are all determined at the same energy level. In contrast, for the nonlinear restricted compliance model, the total and weighted energies are the same but the divided energy approach leads to an undesirable consequence. Specifically, in an all-compression stress state, the compression energy is the total energy and the tension energy is zero; accordingly, the compliances are determined from a mixed set of nonlinear compression properties and linear (elastic) tension properties. Thus, differences between measured strains and strains predicted from the nonlinear restricted compliance material model are attributed mainly to the relations between tension and compression compliances used in the model. The stress-strain behavior of ATJ-S graphite evidently does not closely satisfy the restrictions between compliances in the nonlinear RCM.

For all direct comparisons between predicted and measured strains for the data base material properties, excellent correlation is obtained. Thus, the general material property equation, Eq. (5), can be used to represent the material property-strain energy variation for both tension and compression properties of ATJ-S graphite at 70°F. The procedure used to evaluate the material property constants B and C is also substantiated by the comparisons.

The applicability of the nonlinear multimodulus material models to the prediction of the biaxial strain response of ATJ-S graphite is investigated in Section 6.

6. COMPARISON OF PREDICTED AND MEASURED STRAIN RESPONSE

UNDER BIAXIAL LOADING

6.1 INTRODUCTION

The two nonlinear multimodulus material models discussed in Section 4 are used to predict the biaxial strain response of ATJ-S graphite in this section. Strain predictions of both material models are compared with strains measured by Jortner [6-9, 30] in room temperature tests. Strain predictions of the nonlinear material model of Section 2 are also compared with the biaxial tension strain response measured at room temperature. Thus, an assessment of the basic nonlinear approach without the complications of the multimodulus procedures can be made. Biaxial fracture investigations reported by Jortner [6-9] are another source of experimental data which can be used to assess the applicability of the nonlinear multimodulus material models to prediction of ATJ-S graphite stress-strain behavior. Strains at failure measured in at room temperature tests are compared with predicted strains. The correlation between the predicted strain response with the nonlinear restricted compliance material model and the experimental strain response at 2000°F determined by Jortner [7, 8] is also examined.

The predicted and measured strain results for the room temperature biaxial strain study, the room temperature fracture strain study, and the 2000°F biaxial strain study are presented in Sections 6.2, 6.3, and 6.4, respectively. The pertinent features of the test specimens, test procedures, and data base material properties are discussed in each section. Effects in the strain correlations from differences in specimen origin (different billets), friction on the measured axial loads, and circumferential stress gradients in the biaxial specimens are examined. Adjustments made for these factors are briefly described.

In the discussion of results in this section, percentage deviations between predicted and measured strains are frequently used. Recall from the discussion of Section 2 that percentage deviation is defined as the distance between the experimental (baseline) and predicted strains on the biaxial strain plot divided by the length of a ray from the origin to the experimental strain values. The percentage deviation is schematically depicted in Fig. 23 and is calculated from

$$\% \text{ Deviation} = \left[\frac{(\epsilon_{a_p} - \epsilon_{a_m})^2 + (\epsilon_{c_p} - \epsilon_{c_m})^2}{\epsilon_{a_m}^2 + \epsilon_{c_m}^2} \right]^{1/2} \times 100\% \quad (32)$$

where the subscripts have the following connotations:

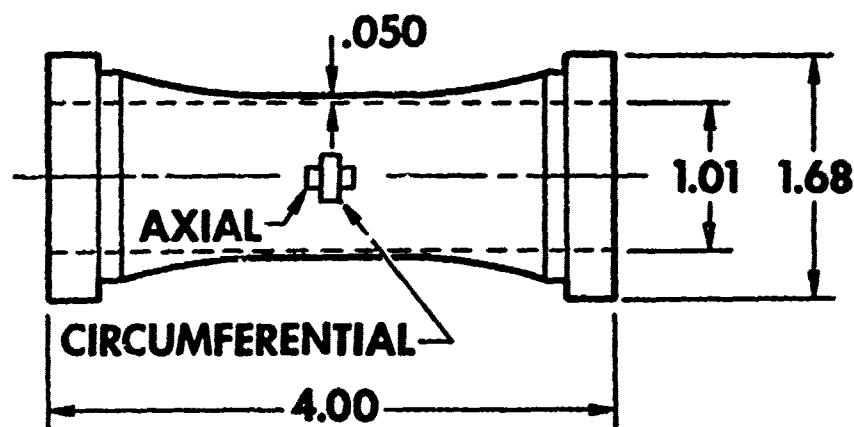
- a - axial direction
- c - circumferential direction
- m - measured values
- p - predicted values

The percentage deviation is often preceded by a + or - sign to denote whether the predicted strains are an overestimate (+) or an underestimate (-) of the measured strains. The measured strains are only approximate since most of the experimental results discussed in this section were obtained from graphical results instead of tabulated results. Therefore, the percentage deviation calculations are approximate.

6.2 ROOM TEMPERATURE STRAIN CORRELATIONS

Jortner's measured biaxial strain results at room temperature are compared with nonlinear WCM and nonlinear RCM predictions in this section. Biaxial tension strain response is also compared with nonlinear material model predictions to obtain an assessment of the nonlinear approach without the complications of the multimodulus models.

A typical hollow biaxial test specimen is shown in Fig. 54 (from Fig. 9, Ref. 7). Internal pressure is applied to the specimen by a pressurizing fluid contained in a thin rubber bladder. Axial loads (either tension or compression) are applied to the specimen at the lips on the specimen ends through a fixture designed to restrict bending. Thus, tests can be performed in two quadrants of biaxial loading. Specimens were loaded to several different ratios of axial stress to circumferential stress ($\sigma_a:\sigma_c$). These nominal stress ratios were approximately constant during loading to a maximum principal thin-wall stress of 3550 psi. Strains were measured with strain gages on the outer surface at the midlength of the specimens. The nominal principal material directions are aligned with the load axes for all specimens. The billet coordinate system is appropriate to use to describe material properties for the biaxial test specimens since the billet axes are also aligned with the nominal principal material directions. The specimen axis (axial load direction) is aligned with the billet axis (z - direction).



DIMENSIONS IN INCHES

FIGURE 54 HOLLOW GRAPHITE BIAxIAL TEST SPECIMEN WITH STRAIN GAGES

6.2.1 Strain Correlations for Nonlinear Material Model Predictions

Strain correlations are performed to determine the applicability of the nonlinear material model in Section 2 to prediction of biaxial stress-strain behavior of ATJ-S graphite. The nonlinear multimodulus material models in Section 4 effectively degenerate to the nonlinear material model either if the material property constants are identical for each independent tension and compression property and the total energy approach is used or if an all-compression or an all-tension stress state exists (with some obvious data input restrictions for the RCM model). In this section, biaxial tension stress states are examined which result from internal pressure and axial tension on the specimen in Fig. 54. Actually, the induced stresses are not all tension, but the radial compressive stress is very small in comparison to the circumferential and axial tensile stresses. Thus, the applicability of the nonlinear material model can be determined without the complications of the multimodulus features of the WCM and RCM models.

To evaluate the effects of stress gradients in the specimens on the theoretical-experimental comparisons, the grid with 355 finite elements (provided by Jortner) in Fig. 55 was used to model each of the specimens. Only half of an actual test specimen need be modeled because of the symmetry of the specimens and applied loads. This grid was used in a modified version of the SAAS III finite element computer program with the new nonlinear material model. The predicted stresses and strains are fairly uniform throughout the thinned down portion of the specimen. However, there is a detectable stress gradient through the specimen wall due to bending. Thus, the specimen in Fig. 54 is a reasonably good engineering test specimen.

The measured strains and the strains predicted with the new nonlinear material model in the SAAS III program are shown in Fig. 56. The measured strain values for a maximum principal thin-wall stress of 3550 psi are Jort-

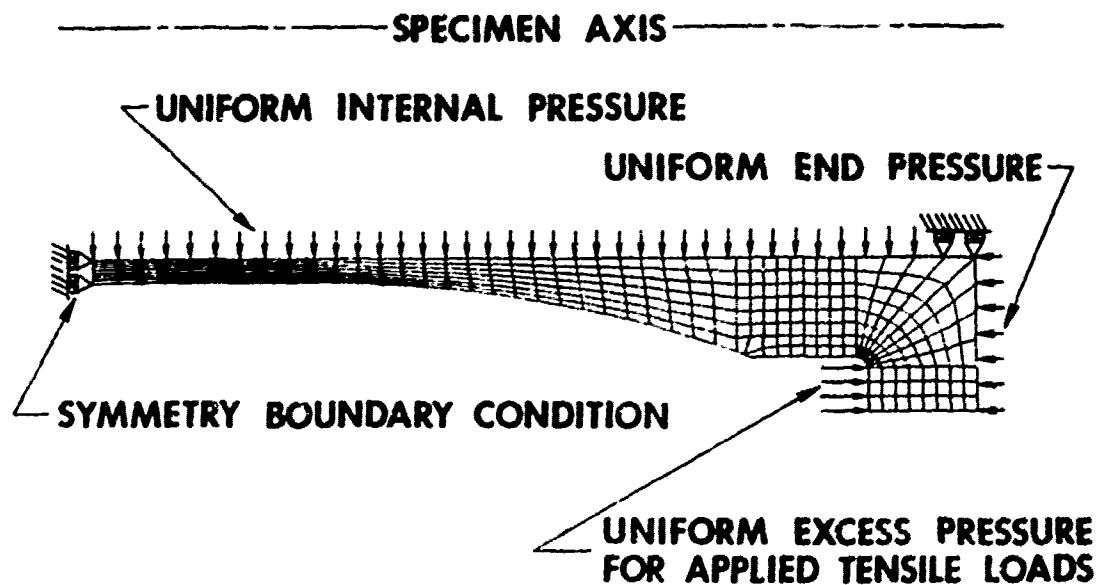


FIGURE 55 FINITE ELEMENT MODEL OF HOLLOW GRAPHITE BIAxIAL TEST SPECIMEN

ner's results [8, 30] on the outside of the specimen midlength. In all but one case, the experimental results shown in Fig. 56 are for specimens from a single billet (1C0-15). The measured strains for the equal biaxial tension stress state are from a billet 3R9-33 specimen. For the nominal stress ratios (1:1.26) and (-1:1), two data points with slightly different actual stress ratios are presented.

Strain predictions for the nominal stress ratios at a maximum principal thin-wall stress of 3550 psi are shown in Fig. 56 for the nonlinear material model. For the convergence criterion used (relative change in total strain energy $\leq .005$), the procedure converged in either five or six iterations. When the finite element procedure is used, stress and strain gradients can be estimated in the specimens. The strain predictions shown are extrapolated to the outer surface of the specimens (where the strains were measured) from the center of the element just inside the outer surface.

The SAAS II predictions in Ref. 8 for a maximum principal thin-wall stress of 3500 psi are repeated in Fig. 56 to allow comparison of the new nonlinear material model with the material model now used in reentry vehicle

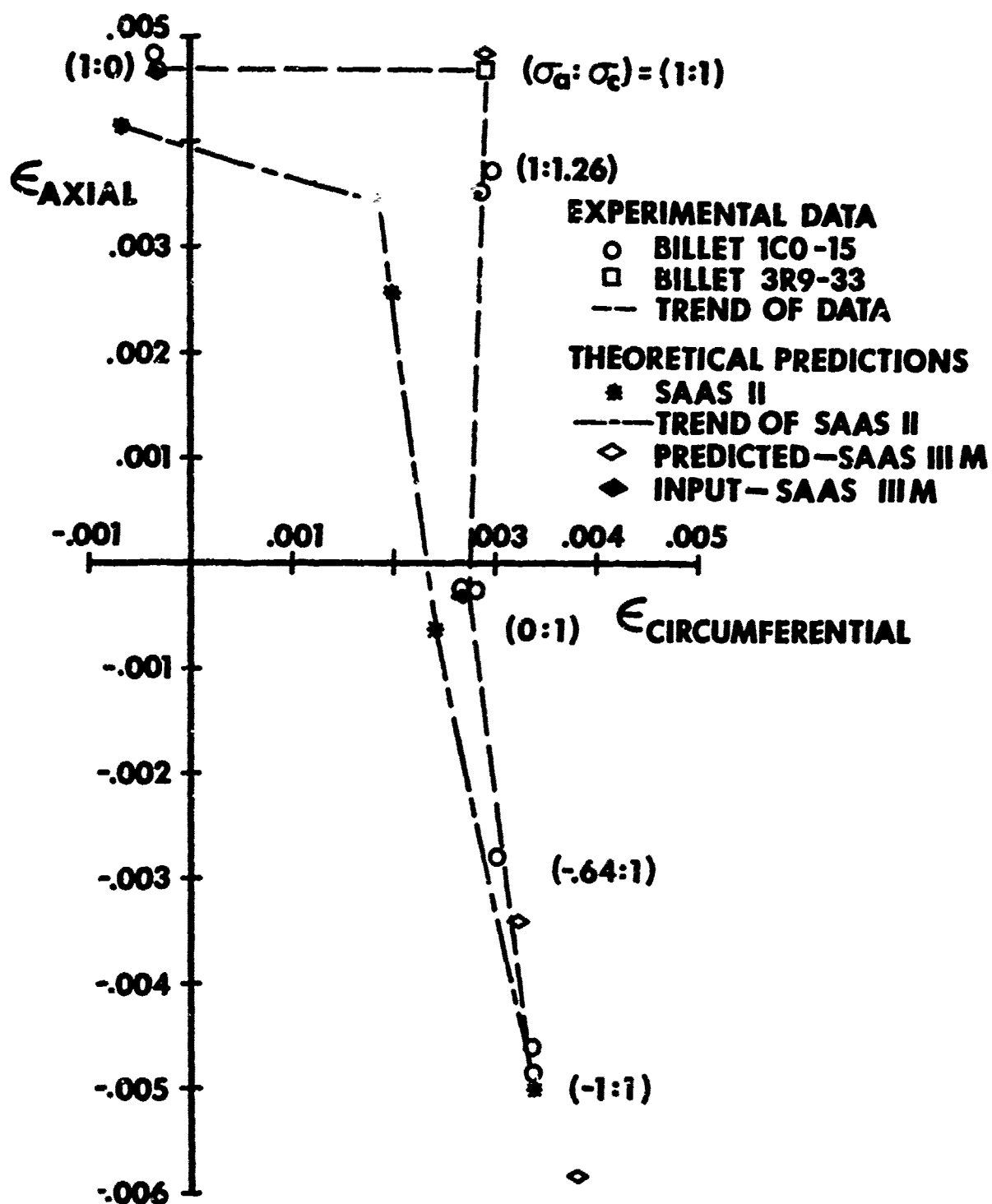


FIGURE 56 PREDICTED AND MEASURED STRAINS IN A HOLLOW GRAPHITE BIAXIAL TEST SPECIMEN - ROOM TEMPERATURE NONLINEAR MATERIAL MODEL

nosetip stress analysis (SAAS II and SAAS III). In the material model of SAAS II [32], a bilinear representation of the uniaxial stress-strain data is used in conjunction with a "normalized effective stress" function to describe nonlinear orthotropic deformation behavior. There is no explicit assumption of a zero plastic volume change in SAAS II. Instead, the stress function that is used in SAAS II and the unaltered version of SAAS III [24] reduces for isotropic materials to the von Mises distortional energy relation. However, that stress function is an arbitrary expression that cannot be derived (that is, it has no basis on theoretical grounds). Despite that necessary condition of reduction to a known relation (which is appropriate for isotropic metals but has not been shown to apply to granular materials), the sufficiency argument for orthotropic materials has not been satisfied. Thus, the applicability of the nonlinear material models in SAAS II and the SAAS III computer programs to prediction of stress-strain behavior for ATJ-S graphite is questionable. In addition, the multimodulus character of the material cannot be represented with SAAS II material model. The SAAS III program does have the linear WCM discussed in Section 3.2. However, the nonlinear and multimodulus material models cannot be used simultaneously in SAAS III. Accordingly, any agreement obtained between measured strains and strains predicted with the SAAS II (or SAAS III) material model is both coincidental and fortuitous.

To reduce effects caused by differences in billet stiffness, specimen design, and test procedures in the evaluation of the nonlinear material model, uniaxial tests of the tubular specimens from billet 1C0-15 were used, where possible, to establish the material property constants. The material property constants $[A, B, C \text{ and } U_0 \text{ of Eq. (5)}]$ for the five independent material properties are given in billet coordinates in Table 9. The following five independent tensile material properties are used as a data base for the nonlinear material model: E_{rt} , E_{zt} , $\nu_{r\theta t}$, $\nu_{z\theta t}$, and G_{rzt} . Differences between

TABLE 9

1C0 DATA BASE AT 70°F FOR NONLINEAR MATERIAL MODEL

MATERIAL PROPERTY	A	B	C	U_0	DATA SOURCE
E_{rt}	1.8519×10^6 psi	.191829	.314467	1 psi	Fig. 17, Ref. 30, 1C0 with circumferential stress gradient adjustment
E_{zt}	1.235×10^6 psi	.204557	.293684	↓	Fig. 14, Ref. 30, 1C0
ν_{ret}	.1	.376247	.169649		Fig. 7, Ref. 30, 16K9
ν_{zet}	.1383	.407264	.0879388		Fig. 14, Ref. 30, 1C0
G_{rz}	$.54 \times 10^6$ psi	0	1		Fig. 28, Ref. 14, Avg.

tensile and compressive material properties are not investigated with the nonlinear procedure. Jortner's across-grain tension results in Fig. 14 of Ref. 30 are used to determine the material property constants for E_{zt} and ν_{zet} . His with-grain tension results in Fig. 17 of Ref. 30 are used to establish the constants for $E_{rt}(=E_{\theta t})$. Values of the remaining two independent material properties are determined from results from billets other than 1C0-15. Material property constants for ν_{ret} are identical to those in the 16K9 data base in Table 8. The remaining material property, G_{rzt} , is assumed to have a constant value of $.54 \times 10^6$ psi. The value of G_{rzt} has a negligible effect on the predicted strain results in the gage sections of the test specimens.

A correction for the circumferential stress gradients is applied to the stress values in Fig. 17 of Ref. 30 before the material property constants for E_{rt} are evaluated. Jortner [9, 30] suggests that the circumferential stress at the outer surface of the specimens is approximately related to the mean stress used as the ordinate in Fig. 17 of Ref 30 by the expression

$$\sigma_{c \text{ outer surface}} \cong K \sigma_{c \text{ mean}} \quad (33)$$

where

$$K \cong .96 \pm .01$$

The mean (thin-wall) circumferential stresses are multiplied by .96 to obtain an estimate of the circumferential stresses in the specimen at the location where the strains were measured.

The new nonlinear material model is a significant improvement over the previously used material model for the two biaxial tension stress ratios investigated. The percentage deviation between test data and predictions for the (1:1) stress ratio is -29.4% for the SAAS II material model and +3.1% for the new nonlinear material model. Similar correlation is found for the (1:1.26) stress ratio; a -32.0% deviation is obtained for the SAAS II nonlinear model and a -2.6% deviation was obtained for the new nonlinear material model. The percentage deviations discussed in this section are based on the experimental point closest to the predicted point. For both biaxial tension stress ratios, the SAAS II material model predictions are a significant underestimate of the strain response. Based on the strain correlations, the new nonlinear material model has excellent potential for description of the biaxial softening phenomenon.

Strain predictions with the new nonlinear material model for the (-.64:1) and (-1:1) stress ratios are poorer than for the biaxial tension stress ratios. However, in those predictions, the multimodulus character of the material is ignored! The deviations between the strain predictions of the new nonlinear material model and the closest experimental results are +15.7% for the (-.64:1) stress ratio and +18.0% for the (-1:1) stress ratio. Obviously, the different moduli of ATJ-S graphite under tension and compression must be accounted for.

The apparently good agreement (2.7% deviation) for the SAAS II material

model is both coincidental and fortuitous as already discussed. That is, the SAAS II yield criterion is obviously crude and its stress-strain model is bilinear instead of having the actual nonlinear behavior. Those facts, coupled with the poor predictions for the SAAS II model in the biaxial tension quadrant, lead to a complete invalidation of the SAAS II (and the SAAS III) nonlinear material model for ATJ-S behavior. However, the new nonlinear material model has attractive characteristics in biaxial tension. The strain correlations for the nonlinear multimodulus procedures are examined next.

6.2.2 Strain Correlations for Nonlinear Multimodulus Material Model

Predictions with the 16K9 Data Base

The experimental strains obtained at room temperature and the strains predicted with the nonlinear weighted compliance material model for a maximum principal thin-wall stress of 3550 psi are shown in Fig. 57. Test data from four different billets are included on this figure. Because a data set for each billet complete enough to serve as a uniaxial data base for the nonlinear WCM is not available, the 16K9 data base in Table 8 is used. Recall that this data base is derived from a portion of the results of Jortner's uniaxial off-axis investigation of billet 16K9 described in Section 5. Therefore, the correlation between predicted and measured strains for the stress ratios (1:1.26) and (0:1) is not affected by billet-to-billet variations in material properties.

The experimental data in Fig. 57 are from Fig. 66 of Ref. 8 and Figs. 14-19 of Ref. 30. Because of friction in the loading apparatus for the biaxial tubular specimens, the measured axial load is in error by less than 1.5% [9, 30]. Therefore, the axial stress in the specimen is approximately

$$\sigma_{a_{\text{actual}}} \cong \sigma_{a_{\text{measured}}} \times 1.015 \quad (34)$$

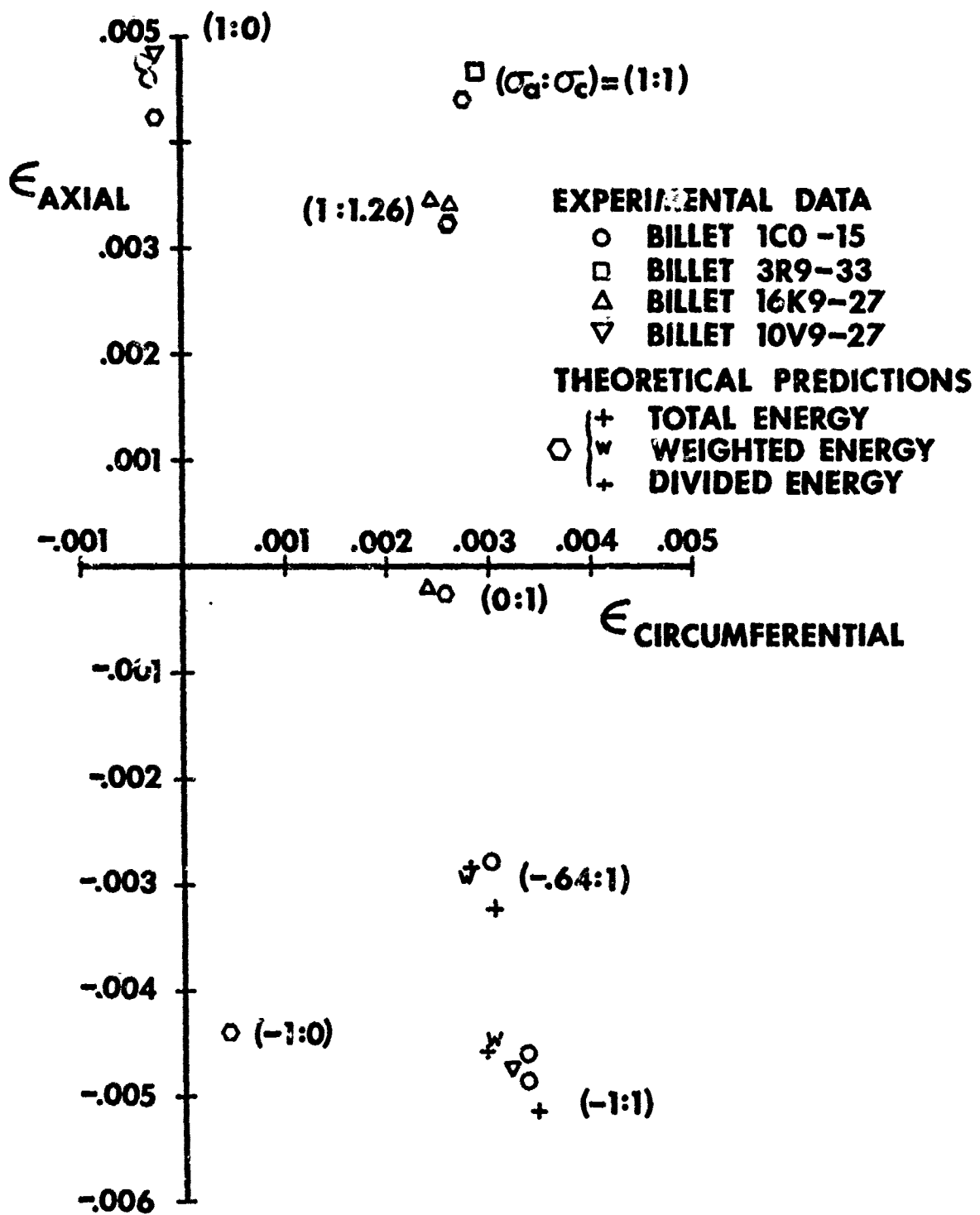


FIGURE 57 PREDICTED AND MEASURED STRAINS IN A HOLLOW GRAPHITE BIAxIAL TEST SPECIMEN - ROOM TEMPERATURE NONLINEAR WCM PREDICTIONS - 16K9 DATA SET

A similar friction effect is noted for the compression rod results in the data base of Table 8. Thus, a friction correction is appropriate for the axial stress components of the (1:0), (1:1), and (1:1.26) stress states. No friction correction need be applied to the axial compression - internal pressure biaxial stresses because the behavior of the biaxial specimens is similar to that of the uniaxial compression rods from which the stress-strain data are obtained. That is, there is no dissimilar behavior as between the uniaxial tension bar and the biaxial specimen under biaxial tension.

The actual experimental strains are obtained for the (1:0) and (1:1.26) stress ratios in the following manner. The tensile stress-strain curve in the axial direction for the biaxial specimen is entered at 50 psi less than the nominal stress, and the corresponding strain is read. (A more precise stress correction is unrealistic because (1) the friction error is approximate and (2) 50 psi is the maximum practical resolution on the plotted stress-strain curves.) The circumferential strain for the (1:1.26) biaxial stress is read directly, (i.e., without adjustment for friction). The two strains (axial and circumferential) are then plotted in Fig. 57 with the assumption that they are for the same biaxial load. The experimental strains for the (1:1) stress ratio are plotted without correction because stress-strain curves are not available. Accordingly, results from Fig. 66 of Ref. 8 are used directly. The predicted strains are obtained by use of the nominal stresses.

The predicted strains in Fig. 57 are obtained with the MULTIW computer program described in Section 4.4. For nominal stress ratios (1:1.26) and (-1:1), two experimental data points with slightly different actual stress ratios are presented. Thus, slightly different strain predictions are obtained for each actual stress ratio. Both strain predictions for the (1:1.26) stress ratio nearly coincide. The predictions shown for the (-1:1) stress ratio are com-

puted for the actual stress ratio of the billet 10V9 results (inverted triangle). Three different sets of strain predictions are shown for each of the two "mixed" stress ratios, $(-.64:1)$ and $(-1:1)$. The different strain predictions for these stress ratios are a result of the differences in the three energy approaches investigated (total energy, weighted energy with $n=1$, and divided energy). Strain predictions for the $(-1:0)$ stress ratio are shown in Fig. 57 despite the fact that no strains were measured on biaxial specimens at that stress ratio (the biaxial specimens might buckle). These predicted strains for the hollow graphite specimen are based on uniaxial stress-strain data for compression rods. The strain prediction is identical for all energy approaches with the nonlinear RCM for the $(-1:0)$ stress ratio.

Because of billet-to-billet variation in material properties, the correlations in Fig. 57 are mainly qualitative in nature. The differences between predicted and measured strain values for the $(1:0)$ stress ratio are attributed mainly to differences in billet stiffnesses. The predicted strains are based on the 16K9 billet data whereas the measured strains are from tests on specimens from billets 1C0 and 10V9. Based on the strain correlations for the $(1:0)$ stress ratio case, billet 16K9 is stiffer in the across-grain (z) direction than either billets 1C0 or 10V9. All three energy approaches in the nonlinear WCM result in the identical strain predictions for the $(1:0)$ loading case. Identical strain predictions also result for the other two uniaxial loading cases, $(0:1)$ and $(-1:0)$, and the two biaxial tension loading cases, $(1:1)$ and $(1:1.26)$.

The predicted and measured strains for the equal biaxial tension stress ratio case, $(1:1)$, agree to within 5.5%. Here, again, the strain correlations could be affected by billet-to-billet variations in material properties. For the two $(1:1.26)$ cases, the deviations between predicted and measured strains

are 4.6% and 7.4%. Recall that, for these cases and the (0:1) case, the data base material properties and the measured strains are obtained from tests of specimens from the same billet. Thus, no undesired effects are introduced in the strain correlations by variations in material properties between billets. However, some variations between predicted and measured strain results can be expected due to the gradient in circumferential stress through the thickness of the biaxial test specimens. The stresses at the outer surface of the specimens where the strains are measured can be different from the "thin-wall" stresses used as a basis for the predictions. The circumferential stress gradient could be the major factor in the 7.7% deviation between predicted and measured strains found for the (0:1) stress ratio case. Consistent billets are not used to obtain the predicted and measured strains for the (-.64:1) and (-1:1) stress ratio cases in Fig. 57. Consequently, an evaluation of the predictions for the different energy approaches will be deferred until Section 6.2.3.

Strain predictions for the nonlinear RCM obtained with the MULTIR computer program and strains measured in room temperature tests are shown in Fig. 58. The strain predictions are for a maximum principal thin-wall stress of 3550 psi. The experimental strains presented in Fig. 58 are identical to those shown in Fig. 57. Material property set E_{ZC} described in Section 5.3.1 was used as a uniaxial data base for the nonlinear restricted compliance material model. The material property constants for the independent material properties in the data base are obtained from billet 16K9 values in Table 8. Due to the composition of the E_{ZC} property set, the predictions of the nonlinear RCM in Fig. 58 and those of the nonlinear WCM in Fig. 57 are identical for the biaxial tension and uniaxial tension cases. When the divided energy approach is used in the nonlinear RCM with the E_{ZC} property set, the transverse

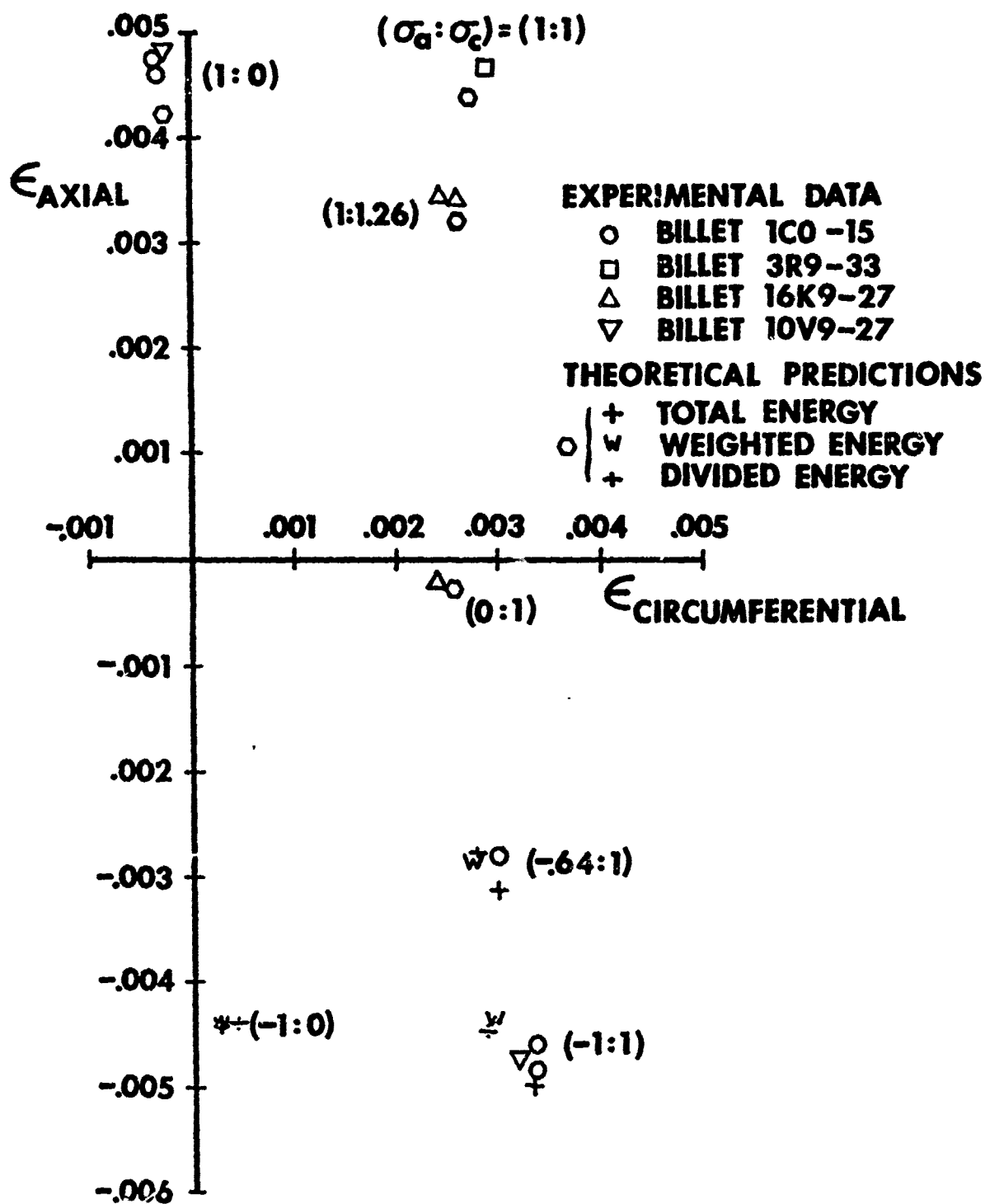


FIGURE 58 PREDICTED AND MEASURED STRAINS IN A HOLLOW GRAPHITE BIAxIAL TEST SPECIMEN - ROOM TEMPERATURE NONLINEAR RCM PREDICTIONS - 16K9 DATA SET

strain prediction for the uniaxial compression stress state (-1:0) is different from the common prediction of the total and weighted energy approaches. With the divided energy approach, the implied off-diagonal compliances are constant on successive iterations because the off-diagonal compliances are always determined from the linear tensile material properties.

The strain predictions with the nonlinear WCM and RCM are different for the mixed biaxial stress states in Figs. 57 and 58. The percentage deviations in the strain predictions with the two material models are shown in Table 10.

TABLE 10 PERCENTAGE DEVIATIONS OF NONLINEAR
RCM STRAIN PREDICTIONS FROM NONLINEAR WCM STRAIN PREDICTIONS

NOMINAL LOADING ($\sigma_a:\sigma_c$)	PERCENTAGE DEVIATIONS		
	TOTAL ENERGY	WEIGHTED ENERGY	DIVIDED ENERGY
(-.64:1)	2.4	1.6	1.5
(-1:1)	3.4	2.3	2.4

The strain predictions with the nonlinear WCM are used as the baseline values for calculation of percentage deviations. The largest percentage deviation in predicted strains is 3.4%. Thus, the effects on strain predictions of the differences in the multimodulus formulations of the two material models are relatively small for the loading conditions and material properties investigated. The agreement between predicted and measured strains found for one material model could be used in a general assessment of both material models.

6.2.3 Strain Correlations for Nonlinear Restricted Compliance Material Model Predictions with the ICO Data Base

The experimental strains and the strains from two numerical prediction

techniques are shown in Fig. 59. Two separate sets of strain predictions for a maximum principal thin-wall stress of 3550 psi are shown for the nonlinear restricted compliance material model. The uniform stress model in the MULTIR computer program is one prediction technique. The 355 element model of the specimens discussed in Section 6.2.1 is used with a modified version of the SAAS III computer program. Both the nonlinear restricted compliance and the nonlinear weighted compliance material models with all three energy approaches are incorporated in the modified version of the SAAS III program. Convergence of the nonlinear material models with changing stresses on each iteration can be studied with the finite element procedure. Moreover, stress and strain gradients can be predicted in the specimens. Strain predictions shown for the nonlinear RCM in the modified SAAS III program are extrapolated to the outer surface of the specimens where the experimental strains were measured.

The experimental results shown in Fig. 59 for all but one case are obtained from tests of specimens from a single billet (1C0-15) in contrast to Figs. 57 and 58. The measured strains presented for the equal biaxial tension stress state were found in tests of a specimen from billet 3R9-33.

To reduce effects caused by differences in billet stiffness, specimen design, and test procedures in the evaluation of the nonlinear multimodulus material models, uniaxial tests of the tubular specimens were used, where possible, to establish the material property constants. The material property constants $[A, B, C, \text{ and } U_0 \text{ of Eq. (5)}]$ for the six independent material properties in the nonlinear RCM property set E_{zc} are given in billet coordinates in Table 11. These material property constants are used to obtain both sets of predictions for the nonlinear RCM. The origin of the material property constants for four of the material properties in this table (E_{rt} , E_{zt} , and $\nu_{z\theta t}$) which are repeated from Table 9 is discussed in Section 6.2.1. As

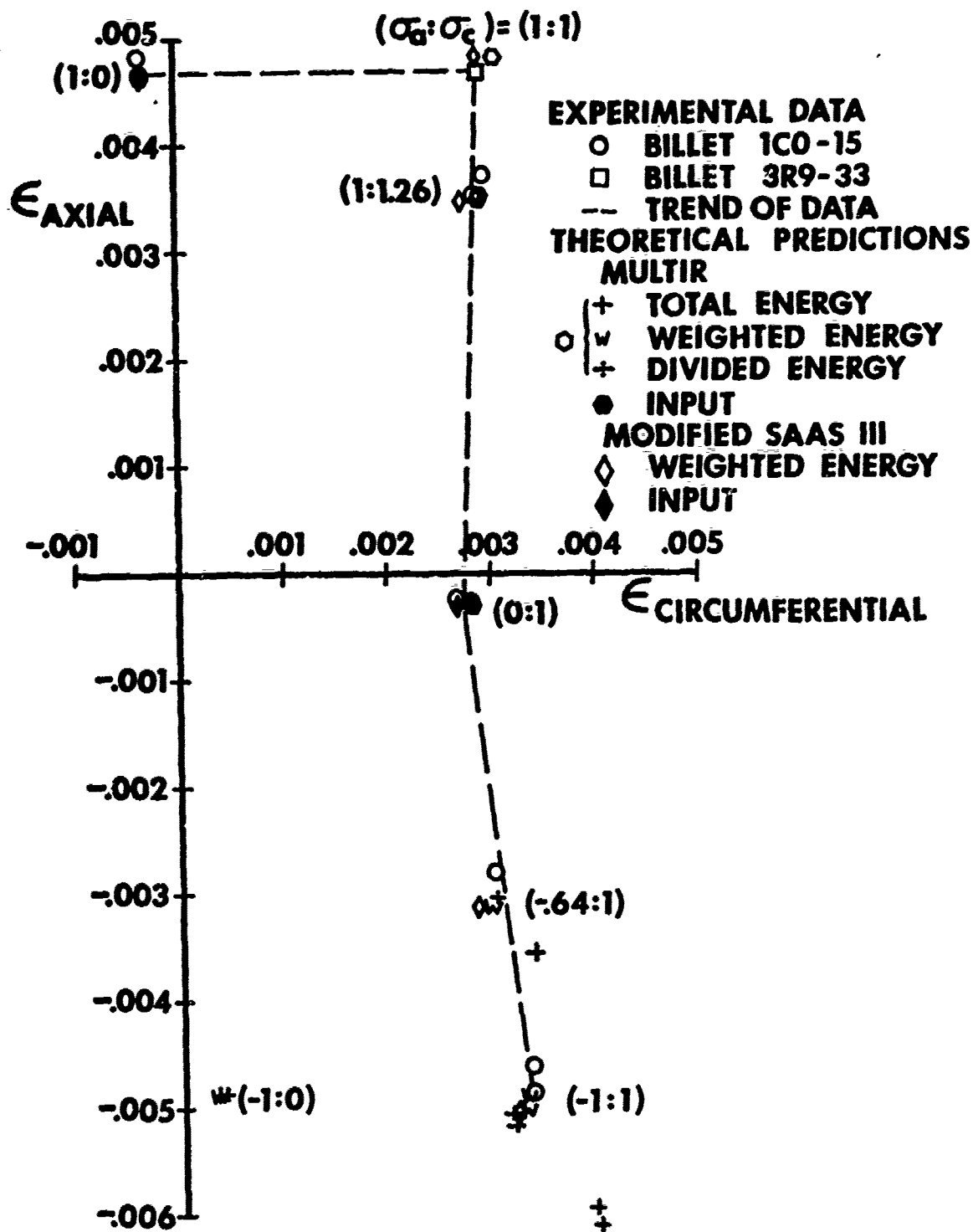


FIGURE 59 PREDICTED AND MEASURED STRAINS IN A HOLLOW GRAPHITE BIAxIAL TEST SPECIMEN - ROOM TEMPERATURE NONLINEAR RCM PREDICTIONS - 1C0 DATA SET

TABLE 11
1C0 DATA BASE AT 70°F FOR NONLINEAR RCM

MATERIAL PROPERTY	A	B	C	U_0	DATA SOURCE
E_{rt}	$1.8519 \times 10^6 \text{ psi}$.191829	.314467	1 psi	Fig. 17, Ref. 30, 1C0 with circumferential stress gradient adjustment
E_{zt}	$1.235 \times 10^6 \text{ psi}$.204557	.293684		Fig. 14, Ref. 30, 1C0
ν_{ret}	.1	.376247	.169649		Fig. 7, Ref. 30, 16K9
ν_{zet}	.1383	.407264	.0879388		Fig. 14, Ref. 30, 1C0
E'_{rzt}	$1.385 \times 10^6 \text{ psi}$.132548	.365323		Fig. 5, Ref. 30, 16K9
E_{zc}	$1.04 \times 10^6 \text{ psi}$.114414	.443771		Fig. 9, Ref. 30, 16K9 Adjusted for billet 1C0 stiffness

was the case with ν_{ret} , material property constants for E_{rzt} are obtained from results from billet 16K9 instead of 1C0. Consequently, the material property constants for ν_{ret} and E'_{rzt} are identical in both the 16K9 (Table 8) and 1C0 (Table 11) data bases.

Material property constants for E_{zc} are obtained from results from billet 16K9. Uniaxial stress-strain results are not available for the tube specimens from billet 1C0 under compression loading (the specimens would buckle!). Thus, an adjustment for the apparent difference in stiffnesses of billets 16K9 and 1C0 is made. The uniaxial strain results in Fig. 9 of Ref. 30 are obtained from the across-grain compression loading of the rod specimens from billet 16K9. At a given stress level, the strain from Fig. 9 of Ref. 30 is multiplied by the ratio of the strains found in across-grain uniaxial tension tests of tube specimens from billet 1C0 and rod specimens from

billet 16K9. The resultant strain is used to evaluate the material property constants for E_{2c} .

The 1C0 data base is used with both nonlinear RCM prediction techniques considered in Fig. 59. For the convergence criterion used in the MULTIR and modified SAAS III programs (relative change in total strain energy $\leq .005$), the procedures converge in four to six iterations for each of the cases analyzed. Recall that the differences in predictions of the two nonlinear RCM approaches are due to stress gradients in the specimens. For the five stress ratios which have a thin-wall circumferential stress of 3550 psi, the circumferential strains predicted with the 355 element grid in the SAAS III program are between 4% and 6% less than those predicted with the MULTIR program with the same energy approach.

Strains predicted with the nonlinear RCM agree well with measured strains for the two biaxial tension stress ratios investigated with the modified SAAS III approach. For the equal biaxial tension stress ratio, a 3% deviation between predicted and measured strains is found. The predictions with the modified SAAS III approach for the nominal (1:1.26) stress ratio are based on the stress ratio of the upper of the two data points. Those predictions are 7% less than the experimental strains. If, instead, the stress ratio of the lower experimental point were used, better (but not significantly better) correlation would be obtained. This speculation is based on the observation that the two predictions with the MULTIR program are essentially on top of one another; a similar result is expected for the modified SAAS III results.

The actual ratio of axial stress to circumferential stress for the two data points with a nominal (1:1.26) stress ratio in Fig. 59 is slightly smaller for the upper point than for the lower point. When the circumferential stress is 3550 psi in Fig. 16 of Ref. 30, then the axial stress in Fig. 15 of

Ref. 30 for the upper experimental data point in Fig. 59 is lower than the axial stress for the lower point. The upper point has the largest strains, but corresponds to a lower axial stress in contradiction to the expected stress-strain behavior. Thus, the differences between the two experimental points for the nominal (1:1.26) stress ratio are probably an indication of the data scatter and not a result of differences in actual stress levels. Given the scatter expected in experimental results, a 7% deviation may represent good agreement.

For the (1:1.26) stress ratio, the strain predictions of the nonlinear material model shown in Fig. 56 are not identical to the strain predictions of the nonlinear RCM shown in Fig. 59 predominantly because of the different stress ratios used. However, even for the identical stress ratios, a small difference between the two sets of predictions could occur. A radial stress gradient exists through the thickness of the specimen. Thus, a triaxial stress state must actually be analyzed. Different material properties are used to determine the compliances in the two material models since the radial stress is a compressive principal stress.

In the biaxial loading quadrant with mixed tensile and compressive loading, the correlation between predicted and measured strain response is dependent on the energy approach used. The percentage deviations for the (-.64:1) data point and one of the (-1:1) data points are presented in Table 12. These percentage deviations are based on the experimental strain results. Results for both the MULTIR and the modified SAAS III formulations of the nonlinear RCM are presented. Percentage deviations are shown for the MULTIR program with all three of the energy approaches. Only the weighted energy approach is investigated with the modified SAAS III program. The actual stress ratios for the two (-1:1) data points are (-.97:1) and (-.99:1). The percentage

TABLE 12
PERCENTAGE DEVIATIONS OF NONLINEAR RCM
STRAIN PREDICTIONS FROM MEASURED STRAINS

LOADING ($\sigma_a:\sigma_c$)	PERCENTAGE DEVIATIONS			
	MULTIR			MODIFIED SAAS III
	TOTAL ENERGY	WEIGHTED ENERGY	DIVIDED ENERGY	WEIGHTED ENERGY
(-.64:1)	20.2	8.3	6.1	9.0
(-.99:1)	23.5	3.2	6.5	4.3

deviations in Table 12 are given for the $(-.99:1)$ data point. To determine the effects of stress gradients in the specimens on the predicted strain response, the $(-.99:1)$ stress ratio is investigated with the nonlinear RCM in the modified SAAS III computer program. The lower of the two $(-1:1)$ experimental points shown in Fig. 59 is the strain result for the $(-.99:1)$ stress ratio. Thus, the strain predictions denoted by the diamond symbol must be compared with the experimental strains for the lower of the two circles.

Based on comparison of the percentage deviations between predicted and experimental strains presented in Table 12, the weighted or divided energy approaches with deviations of 3-9% are superior to the total energy approach with deviations of 20-24%. A recommendation as to which approach, the divided energy or the weighted energy, should be generally used cannot be made based on the percentage deviations in Table 12. However, from the standpoint of the theoretical formulations of the nonlinear RCM, the weighted energy approach might be preferable. With the weighted energy approach, all material properties are evaluated at the same energy level. In that manner, the additional restrictive implications of the evaluation of tensile and compressive

material properties at different energy levels are avoided.

6.3 FRACTURE STRAIN CORRELATIONS

The experimental stress-strain results obtained by Jortner [6-8] in the biaxial fracture investigation at room temperature are used to further evaluate the nonlinear multimodulus material models. In this section, measured strains at failure are compared with predicted strains. In fact, these fracture strain results were obtained by further loading of the same specimens discussed in the preceding section. Note that a failure criterion is not included in the modified SAAS III computer program nor in MULTIW or MULTIR. Thus, only the relationships between failure stresses and strains are predicted herein, not the stresses and strains which will produce failure. The failure stress levels are input quantities used to predict the strains at failure.

Hollow test specimens (see Fig. 54) were loaded at room temperature to failure. Stresses and strains at fracture found by Jortner [7] for six of the tubular test specimens from billet 16K9-27 are presented in Table 13.

The predictions with both the nonlinear WCM and the nonlinear RCM are shown along with measured strains in Figs. 60 and 61, respectively. Data base material properties in Table 8 are used with the MULTIR and MULTIW computer programs to obtain the predicted strains in these figures. Recall that the material property constants presented in Table 8 are determined from uniaxial tests of specimens from billet 16K9-27. Thus, billet-to-billet variations in material properties are not introduced in the strain predictions in Figs. 60 and 61. The effects of stress gradients on strains in the hollow specimens are expected to be similar in nature and perhaps slightly larger than those found in the strain predictions of Section 6.2.3. Moreover, those stress gradient effects can be evaluated only by use of the relatively expen-

TABLE 13
FRACTURE STRESSES AND STRAINS AT 70°F
FROM BILLET 16K9-27 (Ref. 7, p. 52)

CASE NUMBER	σ_a (psi)	σ_c (psi)	ϵ_a	ϵ_c
1	3980	0	.0054	-.0004
2	3900	0	.0049	-.0004
3	3870	4900	.0056	.0038
4	3550	4490	.0047	.0035
5	0	4710	-.0003	.0035
6	-400	4890	-.0008	.0034

sive finite element approach. Thus, the essential characteristics of the stress gradient effects are known well enough that the finite element analysis expense is not justified. Basically, the stress gradient is believed to be the main cause of differences between predicted and measured strains for the specimen under internal pressure.

The predictions with the nonlinear WCM and the nonlinear RCM are identical for all stress states except the mixed biaxial stress states ($\sigma_a = -400$ psi, $\sigma_c = 4890$ psi) for the loading conditions and material property sets investigated. The differences in predicted strains for the mixed biaxial stress states are small and not even perceptible in Figs. 60 and 61. The largest deviation between predictions with the two material models based on the prediction of the nonlinear RCM is approximately .5%. Approximate percentage deviations between measured strains and strains predicted with the nonlinear RCM for the weighted energy approach are presented in Table 14. The measured

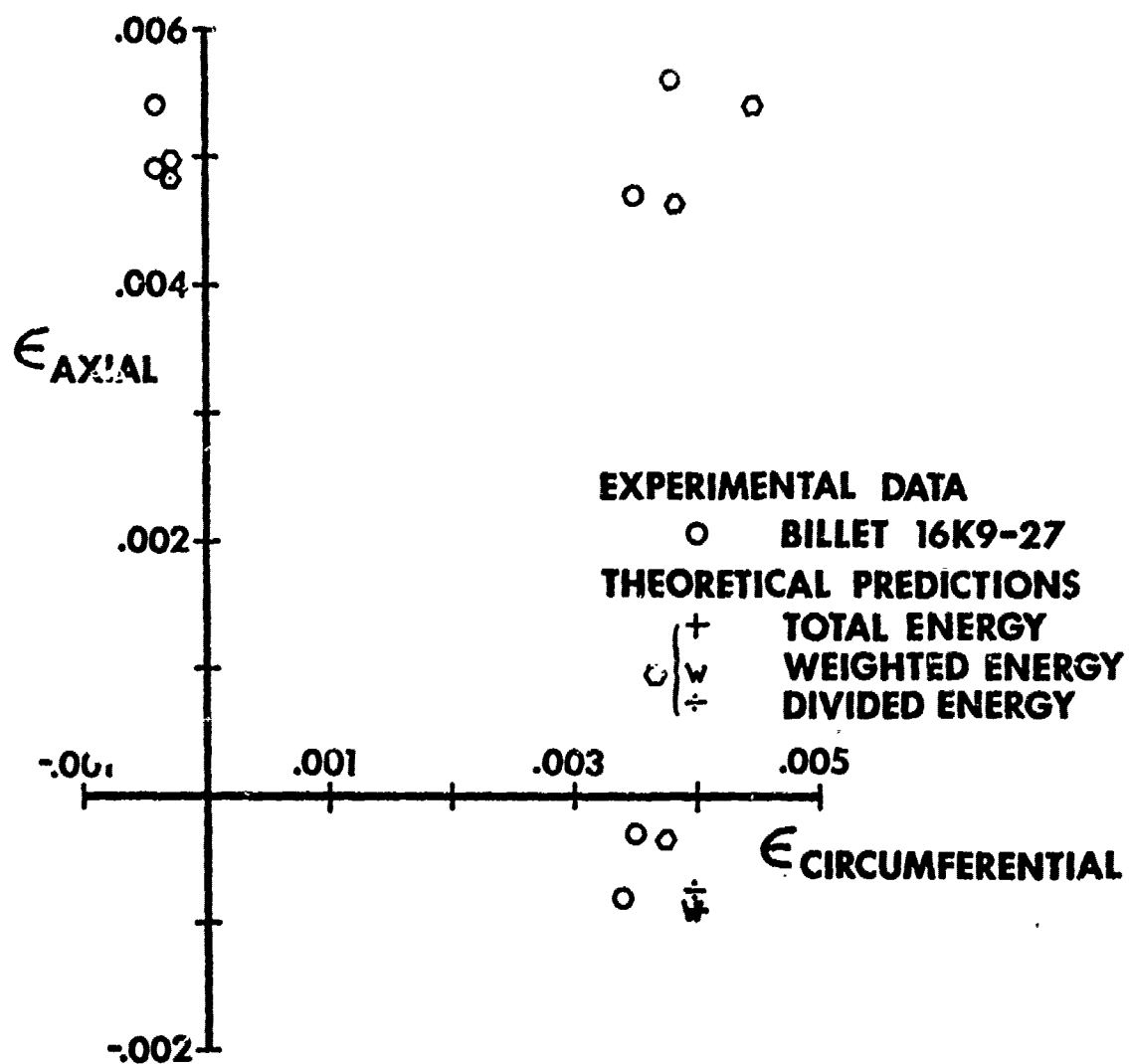


FIGURE 60 PREDICTED AND MEASURED STRAINS IN A HOLLOW GRAPHITE BIAxIAL TEST SPECIMEN - ROOM TEMPERATURE FRACTURE RESULTS - NONLINEAR WCM PREDICTIONS - 16K9 DATA SET

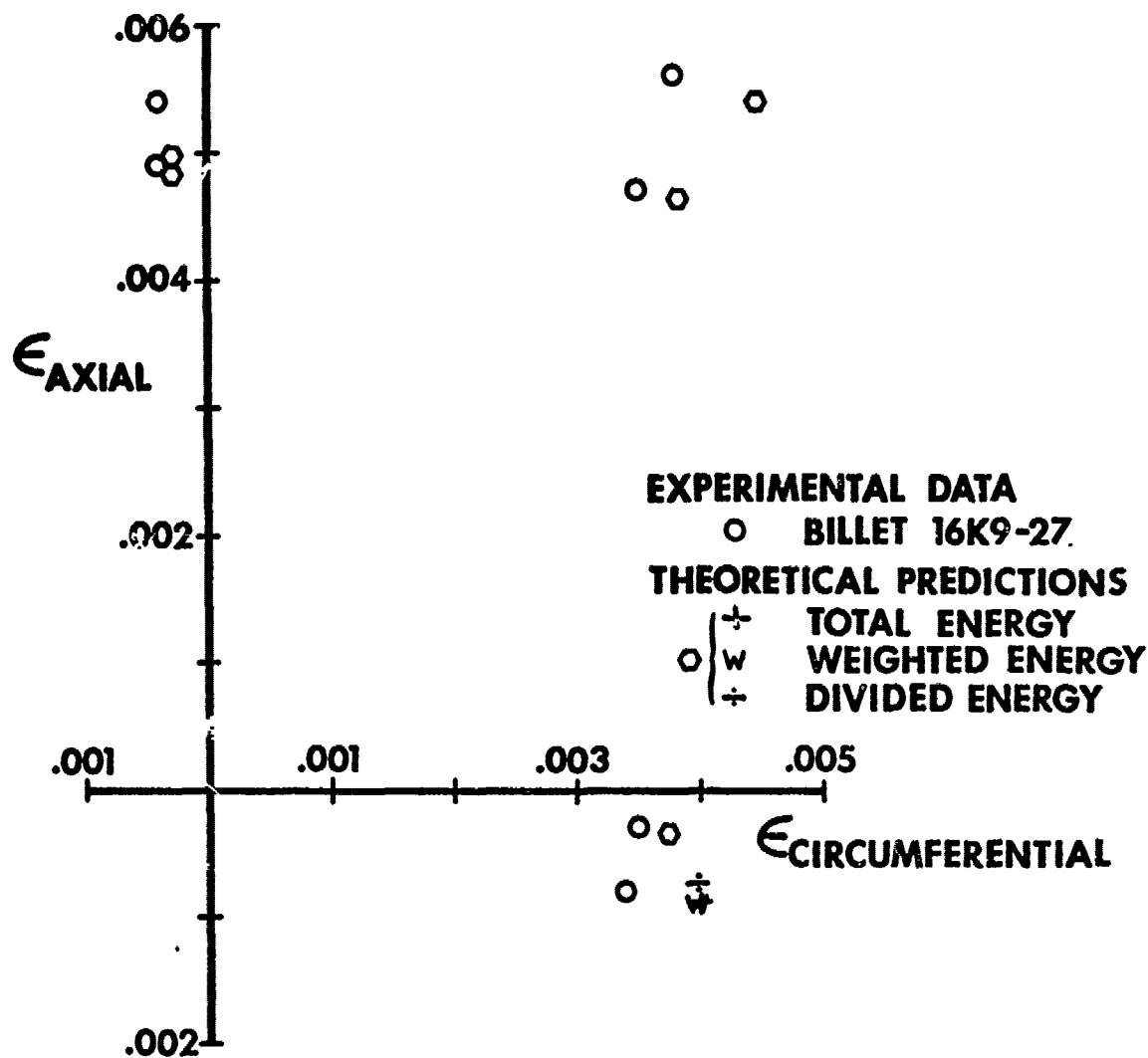


FIGURE 61 PREDICTED AND MEASURED STRAINS IN A HOLLOW GRAPHITE BIAxIAL TEST SPECIMEN - ROOM TEMPERATURE FRACTURE RESULTS - NONLINEAR RCM PREDICTIONS - 16K9 DATA SET

TABLE 14
PERCENTAGE DEVIATIONS OF NONLINEAR RCM
STRAIN PREDICTIONS (WEIGHTED ENERGY APPROACH) FROM FRACTURE STRAINS

CASE NUMBER	σ_a (psi)	σ_c (psi)	PERCENTAGE DEVIATION
1	3980	0	8.2
2	3900	0	2.8
3	3870	4900	10.4
4	3550	4490	5.5
5	0	4710	7.0
6	-400	4890	16.2

strains are used as base values in the computation of the percentage deviations. As can be seen in Table 14, the smallest deviation, 2.8%, occurs for the uniaxial stress state ($\sigma_a = 3900$ psi, $\sigma_c = 0$) and the largest deviation, 16.2%, occurs for the mixed biaxial stress state. The percentage deviations in Table 14 for cases 3-6 would be reduced if the effects of stress gradients were evaluated. The overall agreement between predicted and measured strain results is only fair since the largest deviation is 16.2%. However, as fracture is approached, the stress-strain curves become more nonlinear than at 3550 psi maximum principal stress. Thus, fracture strain predictions should be expected to be less accurate than at lower stress levels.

6.4 2000°F STRAIN CORRELATIONS

The 2000°F stress-strain behavior of ATJ-S graphite under multiaxial loadings was investigated by Jortner [7-9]. His measured biaxial strain results are compared with the predictions of the nonlinear RCM in this section.

The hollow test specimens used in the 2000°F biaxial investigations are identical in shape to those used in the room temperature investigations (see Fig. 54). A thin nickel bladder was used inside the 2000°F specimens to contain the internal pressurizing gas instead of the rubber bladder used in the room temperature specimens. Strains at 2000°F were measured with optical extensometers. (Recall that strain gages were used in room temperature tests.) Several different ratios of axial stress to circumferential stress ($\sigma_a:\sigma_c$) were investigated. The loading directions were aligned with the nominal principal material direction. Details of the specimen design, loading apparatus, and test procedures are found in Refs. 7 and 8.

To implement the nonlinear multimodulus strain prediction procedures, a uniaxial data base is required to establish the relations between material properties and total strain energy. The 2000°F experimental biaxial strain results were obtained by Jortner [8] for ATJ-S graphite billet 1C0-15. Unfortunately, uniaxial test data at 2000°F are not available for billet 1C0-15. The uniaxial data bases used for the strain correlations in this section are obtained from the average results of Starrett and Pears [14]. Those results are the average of test results from a large number of tests performed on numerous billets.

Material property constants for the "average" 2000°F data base are presented in Table 15. The constants for the material properties E_{rt} , E_{zt} , and E_{zc} are derived from the stress-strain curves in Figs. 4, 8, and 20 of Ref. 14, respectively. For the balance of the material properties in the data set in Table 15, stress-strain data are not available to define material property variation with total strain energy. Thus, constant values are used for ν_{rt} , ν_{zt} , and E'_{rzt} . Some raw transverse deformation data is presented by Starrett [33]. However, these data are results from individual tests and are

TABLE 15
AVERAGE DATA BASE AT 2000°F

MATERIAL PROPERTY	A	B	C	U_0	DATA SOURCE
E_{rt}	1.88×10^6 psi	.0321362	.788298	1 psi	Fig. 4, Ref. 14
E_{zt}	1.375×10^6 psi	.0527850	.665860	↓	Fig. 8, Ref. 14
ν_{rt}	.128	0	1		Fig. 26, Ref. 14
ν_{zt}	.108	0	1		ν_{rzt} and compliance relation
E'_{rzt}	1.4875×10^6	0	1		Compliance transformation relationship with G_{rz} from Fig. 28, Ref. 14
E_{zc}	1.58×10^6 psi	.156581	.352135	↓	Fig. 20, Ref. 14

not compatible with "average" results. The material property constant A for the direct modulus at 45° to the r-z principal material directions is estimated from the value of G_{rz} in Fig. 28 of Ref. 14 and a compliance transformation relationship.

A data base suitable for the nonlinear WCM was not developed because the uniaxial stress-strain data are inadequate. Strains are correlated only with the nonlinear RCM. Differences between the predictions of the nonlinear RCM and the nonlinear WCM are small in the room temperature investigation in Section 6.2.2. In fact, for the material property sets used in Section 6.2.2, the predictions with the nonlinear RCM and the nonlinear WCM are identical for the biaxial tension stress states. An RCM property set with the same composition of independent material properties is used in this section. Accordingly, the results for the nonlinear RCM might be representative of those expected for the nonlinear WCM.

The experimental strains obtained at 2000°F and the strains predicted

with the nonlinear restricted compliance material model are shown in Fig. 62. The experimental data points in Fig. 62 for a maximum principal stress of 3550 psi are obtained from Fig. 67 of Ref. 8. The average data base in Table 15 is used with the MULTIR computer program to obtain the predicted values. The strain correlations for the uniaxial loading cases (1:0) and (0:1) are evidence that the 1C0-15 billet stiffnesses differ from the average values. In the axial (across-grain) direction, billet 1C0-15 is probably not as stiff as the "average" billet. The differences between predicted and measured strains for the (0:1) case is possibly due in part to stress gradients in the tube specimens.

To obtain a more effective evaluation of the three biaxial loading conditions, the predicted strains for the two uniaxial loading conditions in Fig. 62 are forced to approximately correspond to experimental results by adjustments of the uniaxial data base material properties. The values of material property constant A for three of the six independent material properties are altered in the following manner. The values of A for E_{rt} and E_{zt} are scaled by the ratios of the apparent experimental stiffness at 3550 psi to the stiffness predicted with the average data base. An average of experimental strains is used to define the apparent experimental stiffness. For E_{rt} ($=E_{\theta t}$), a correction for stress gradient is also made. The thin-wall stress is multiplied by .97 to obtain an estimate of the stress at the outer surface of the specimen where the strains were measured. The factor .97 is based on the stress gradient predicted for the tube specimen under the same uniaxial loading at room temperature. The new value for $\nu_{z\theta t}$ is computed from the average experimental transverse strain for the (0:1) stress ratio case. The revised 2000°F data base is presented in Table 16. Good correlation is ensured at a specific strain energy level by these adjustments. However,

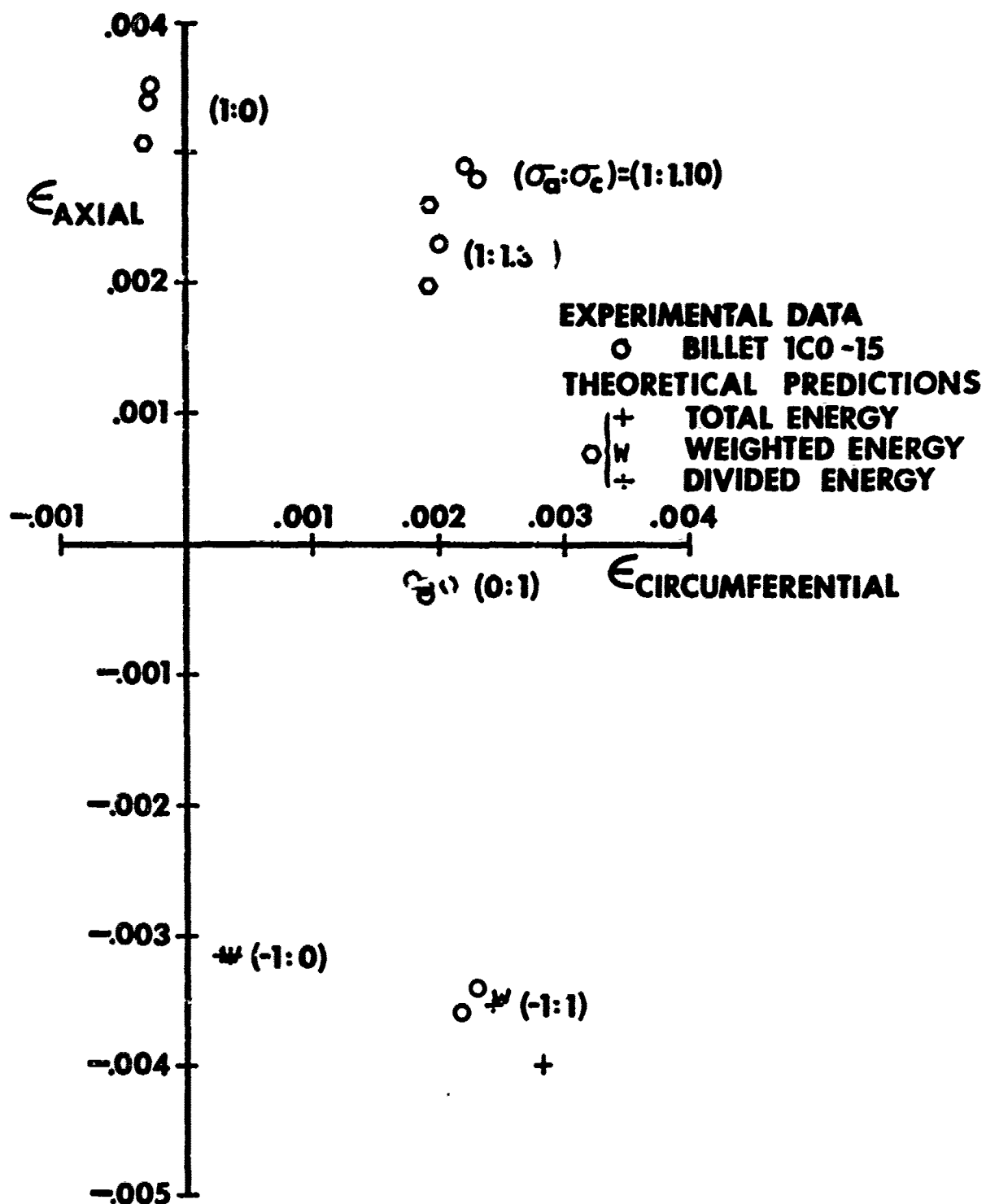


FIGURE 62 PREDICTED AND MEASURED STRAINS IN A HOLLOW GRAPHITE BIAxIAL TEST SPECIMEN - NONLINEAR RCM PREDICTIONS - 2000°F AVERAGE DATA SET

TABLE 16
REVISED DATA BASE AT 2000°F

MATERIAL PROPERTY	A	B	C	U_0	DATA SOURCE
E_{rt}	2.0135×10^6 psi	.0321362	.788298	1 psi	Revised Fig. 4, Ref. 14
E_{zt}	1.2495×10^6 psi	.0527850	.665860	↓	Revised Fig. 8, Ref. 14
$\nu_{r\theta t}$.128	0	1		Fig. 26, Ref. 14
$\nu_{z\theta t}$.093	0	1		Estimated from uniaxial loadings herein on Fig. 59
E'_{rzt}	1.4875×10^6 psi	0	1		Compliance transformation relationship with G_{rz} from Fig. 28, Ref. 14
E_{zc}	1.4357×10^6 psi	.156581	.352135		Revised Fig. 20, Ref. 14

strain correlation at other energy levels is still an unresolved question. In any event, the available experimental results are not adequate for more refined adjustments.

Strain predictions with the nonlinear RCM for the revised 2000°F data base are presented in Fig. 63 along with experimental strains at a maximum principal thin-wall stress of 3550 psi. The predicted strains for the (0:1) stress ratio case do not coincide with the average experimental strains because the effects of stress gradients cannot be predicted with the MULTIR computer program used to obtain all the predicted strain results. For the two biaxial tension stress ratios, (1:1.10) and (1:1.35), the predicted circumferential strains are too small possibly because of the assumption of a constant tensile Poisson's ratio ($\nu_{z\theta t}$) independent of the strain energy level. However, if $\nu_{z\theta t}$ did decrease with increasing energy level, then the axial strains as well as the circumferential strains would increase.

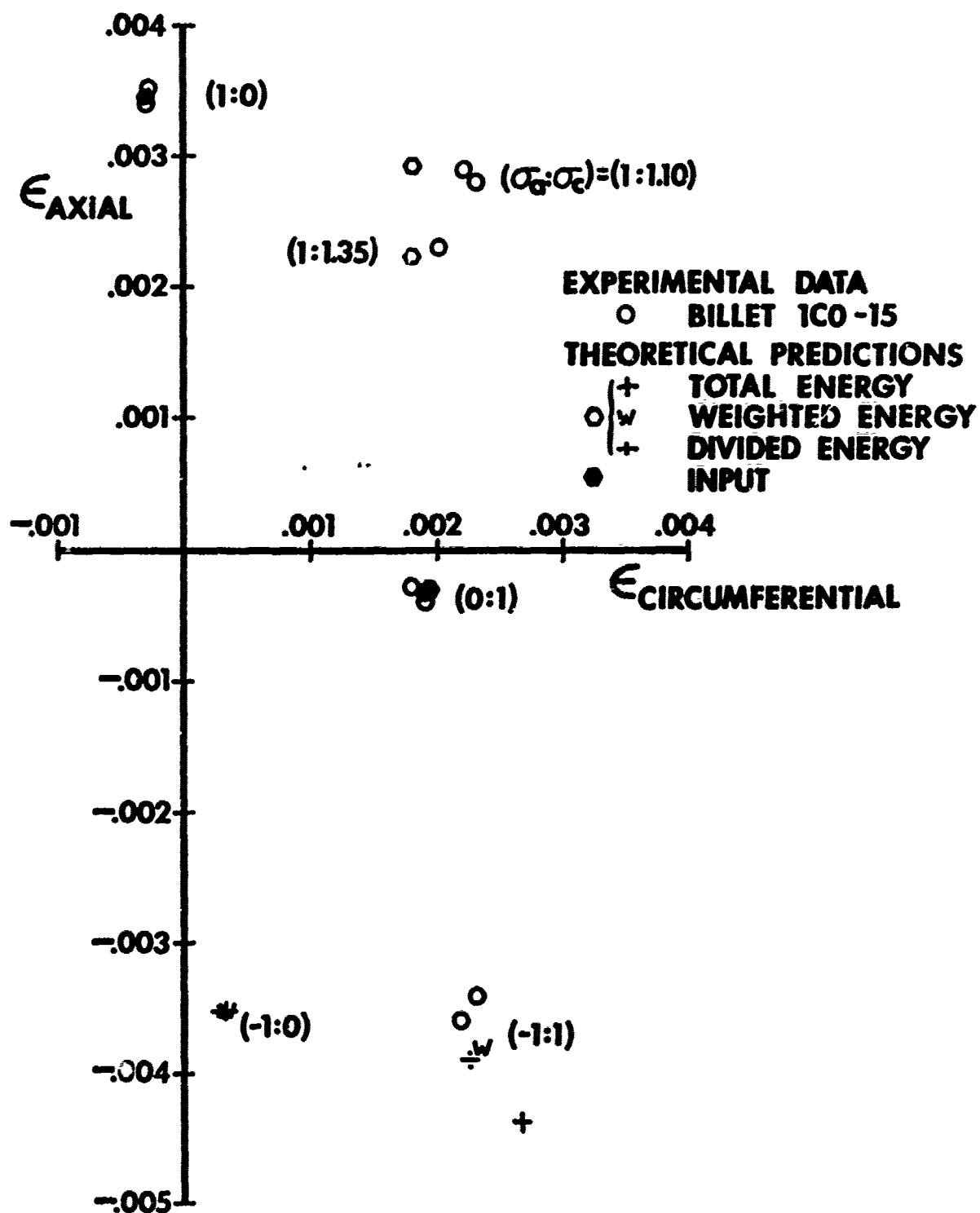


FIGURE 63 PREDICTED AND MEASURED STRAINS IN A HOLLOW GRAPHITE BIAxIAL
 TEST SPECIMEN - NONLINEAR RCM PREDICTIONS - 2000°F REVISED
 DATA SET

A quantitative discussion of the strain correlation might be inappropriate for the 2000°F results because of possible inaccuracies in the experimental results. Jortner [9] states that the use of the optical extensometers might induce "relatively large experimental uncertainties" in the measured strain results. He also states that the nickel bladder is so stiff that it cannot be ignored in comparison to the specimen stiffness (as is done in the present correlations). Even with the uncertainties in both the predicted and measured strains, the general trend of the predictions does agree with the 2000°F experimental results.

6.5 SUMMARY

Biaxial strain predictions with the various nonlinear material models described in this report are compared with several types of experimental data in this section. The comparisons with room temperature data are for biaxial tension and mixed tension and compression at a maximum principal thin-wall stress of 3550 psi as well as at higher stresses at fracture. Comparisons are also made at elevated temperature (2000°F) to round out the comparisons of model predictions with representative nosetip conditions.

The room temperature biaxial tension predictions are within about 3% of the experimental results. Thus, the basic relationship between the secant moduli of the nonlinear stress-strain curves and the strain energy is shown to be accurate. Accordingly, the phenomenon of softening under biaxial tension is now predictable with the new material model.

The extensions of the new material model to different room temperature behavior in tension and compression are not quite as accurate as in biaxial tension. The strain predictions are fairly good (within 9%), however, when the weighted energy or divided energy approaches are used in the nonlinear RCM

as opposed to the total energy approach. The predictions with the nonlinear WCM are slightly different from those with the nonlinear RCM for the loading and material properties considered. However, uniaxial stress-strain data are often not sufficient to apply the nonlinear WCM.

The room temperature predictions of strains at fracture are less accurate than the strain predictions at 3550 psi maximum principal stress. As fracture is approached, the stress-strain curves become more nonlinear than at 3550 psi. Thus, the larger strain prediction inaccuracy, up to 10% in biaxial tension and 16% in mixed tension and compression, should be expected.

The 2000°F strain predictions are the least accurate of all comparisons made. However, the 2000°F comparisons are adversely influenced by the fact that the stiffness of the pressure retaining bladder inside the graphite specimen is not accounted for in the present analysis.

7. CONCLUDING REMARKS

New material models for deformation behavior of artificial graphite under initial loading are discussed. These new material models are based on a new deformation theory of orthotropic plasticity and can be used in finite element computer programs. One material model is used to predict nonlinear stress-strain behavior of ATJ-S graphite under arbitrary uniaxial and biaxial tension stress states. Two other material models are investigated for prediction of both nonlinear and multimodulus deformation behavior. The same nonlinear approach is common to all three new material models. The distinction between the two nonlinear multimodulus material models is based on the multimodulus approach used or, more specifically, on the determination of the compliance matrix.

Each independent material property in the nonlinear approach can vary in an arbitrary manner as actually occurs in uniaxial tests and is related to the multiaxial state of stress and strain by a strain energy function. In linear multimodulus material models, the composition of the compliance matrix is determined from the signs of the principal stresses. In the nonlinear multimodulus material model, the selection of material properties and, consequently, the stress-strain relations, is based on both the signs of the principal stresses and the magnitude of an energy function. An iteration procedure is used in the nonlinear material model to simultaneously satisfy, to a specified tolerance, the nonlinear stress-strain relations and the material property versus strain energy equations. An extension of the iteration approach is used in the nonlinear multimodulus material models to simultaneously satisfy the constraints of both the nonlinear and multimodulus problems. The iteration procedures are stable and converge in six iterations or less for a majority of the cases examined.

The practical use of the new material models is no more difficult than the material models of Jones and Crose [24, 32] which are now used in reentry vehicle nosetip stress analysis. For their models, constants are determined for the best-fit bilinear representation of uniaxial stress-strain data. In both the new nonlinear material model and the new nonlinear multimodulus material models, constants are required for the equations relating material properties to the strain energy. The necessary material property representation can be made by the people who measure the material properties. For example, Starrett and Pears [14] display both the experimental stress-strain curves and the bilinear approximation. They could, with little extra effort, present similar recommended material property values for the new material models. The number of independent material properties required to apply the nonlinear multimodulus material models is dependent on the multimodulus procedure used as well as on the symmetry of the body and loading and the degree of material anisotropy. In the restricted compliance material model, restrictions between the material properties determined in uniaxial tension and uniaxial compression are imposed to maintain compliance matrix symmetry under transformation of coordinates. As a consequence, the number of independent material properties is reduced. Because of these relations, restrictions are placed on the stress-strain behavior that can be treated with the restricted compliance approach. Not all materials have properties for which the restrictions are satisfied. In particular, the Poisson's ratios may decrease under increasing tension load, but increase under increasing compression load. Thus, the properties for each material, to which the model is to be applied, must be examined to see if the restricted compliance model is applicable. If those restrictions are not met, then another model must be used.

The application and evaluation of the new material models is hampered by

the lack of suitable uniaxial stress-strain data to determine material property constants in the general nonlinear stress-strain relations. Poisson's ratio data are inadequate to properly establish the variation with strain energy. All complexities of data acquisition are multiplied by two when multimodulus materials are considered. That is, all data must be gathered under tension as well as under compression loading. Moreover, a new parameter, the Young's modulus at 45° to principal material directions, must be measured in both tension and compression. These new moduli are the replacement for the usual shear modulus.

The validation of the new material models would be hastened if uniaxial and multiaxial test data were measured on specimens from the same billet. Accordingly, billet-to-billet variations in material properties could be eliminated as one cause for disagreement between predicted and measured strains. Then, the predictions and measurements could be compared without undesirable influences and hence in the most scientific manner.

The material property data and, in particular, the material property constants in the new material models are reported to more (usually six) significant figures than necessary. The accuracy of the model will not suffer at all if the number of significant figures is reduced to three. In fact, use of more than three significant figures in reentry vehicle nosetip stress analysis problems is not justified when the inescapable variability of graphite is considered.

In the nonlinear single modulus and the nonlinear multimodulus material models, several energy functions are investigated for relating multiaxial to uniaxial deformation behavior. Total strain energy and distortional strain energy are investigated for the nonlinear single modulus material model. However, application of distortional strain energy to anisotropic materials is

hindered by the interdependence of the distortional and dilatational energy components. Thus, the usual distortional energy-based theories for isotropic metals are not applicable to anisotropic materials such as ATJ-S graphite. For the nonlinear multimodulus models, three energy functions are studied: (1) total strain energy, (2) divided strain energy (the strain energy of tensile stresses is separated from that due to compressive stresses), and (3) weighted strain energy (the strain energy used in the material property-energy relations is a weighted combination of the tensile and compressive strain energies). The tensile and compressive strain energies are separated to describe the different deformation behavior under tensile and compressive loads. However, in the divided energy approach, the off-diagonal compliances must be constant for all energy levels so even more material behavior restrictions are imposed than with the basic restricted compliance model.

Two nonlinear multimodulus material models are used in prediction of uniaxial deformation behavior of ATJ-S graphite for loads applied at various angles from principal material directions (off-axis tests). When these predictions are compared with the strain response measured by Jortner [30], the best overall correlation exists for the nonlinear weighted compliance model. In that model, the tension and compression compliances are weighted in accordance with the proportion of tensile and compressive stresses to obtain a symmetric compliance matrix. Differences between measured strains and the predictions with the nonlinear restricted compliance material model are attributed mainly to the restrictions on tension and compression compliances inherent to the model. That is, the stress-strain behavior of ATJ-S graphite does not closely fit the restrictions on tension and compression compliances. Different strain predictions are obtained when mainly tension compliances are used and compression compliances are generated by use of the restrictions than when mainly

compression compliances are used. At 5000 psi, deviations of 8 to 12% in axial strain predictions occur between the two types of predictions. Accordingly, the nonlinear weighted compliance material model is preferable to the nonlinear restricted compliance material model for graphite.

Excellent correlation is obtained between predicted and measured strains. With the exception of two low stress level predictions, differences between predicted and measured strains are less than 8%. Thus, use of the general material property equation, Eq. (5), and the simultaneous solution procedure for material property constants B and C results in an effective description of the material property-strain energy variations for both tensile and compressive properties of ATJ-S graphite at 70°F. The form of the present equation may be generally applicable to a wide variety of engineering materials. Other forms for the general material property-strain energy equation could be investigated. Alternative, but more complicated, expressions might result in even better representation of material property variations with strain energy.

Biaxial strain predictions are compared with strain values from Jortner's tests of ATJ-S graphite [7-9, 30] to evaluate the new material models. The new nonlinear material model is a significant improvement over the previously used material model for the two biaxial tension stress ratios investigated with both material models. Strain predictions with the nonlinear material model due to Jones and Crose [24, 32] are approximately 30% lower than measured strains. For the new nonlinear material model, the theoretical results are within about 3% of the measured strains in biaxial tension. Thus, the new nonlinear material model is appropriate for description of the biaxial softening phenomenon.

The strain correlations for the nonlinear restricted compliance model with either the weighted energy or divided energy approach are within 9% for

biaxial loading cases with mixed tensile and compressive principal stresses at room temperature. Strains are overpredicted by about 20% with the total strain energy approach. Based on the results of some preliminary strain correlations, the predictions with the two nonlinear multimodulus material models are only slightly, if at all, different for the biaxial stress states investigated. Thus, similar strain correlations are anticipated for the nonlinear weighted compliance model.

When measured strains at fracture are compared with strain predictions from the nonlinear multimodulus material models, the overall agreement is only fair (the largest deviation is approximately 16%). The measured failure stress levels are used to predict the strains at failure. Measured biaxial strain results for tests at 2000°F are also compared with predictions from the nonlinear restricted compliance model. Uncertainties exist in the predictions due to neglect of the stiffness of a reinforcing bladder inside the graphite specimens. Moreover, uncertainties also exist in the measurement of strains with optical extensometers. Even with uncertainties in both the predicted and measured strains, the general trend of the predictions does agree with the 2000°F experimental results.

The experimental biaxial results are few in number and limited to only two quadrants of biaxial loading. Thus, a comprehensive validation of the nonlinear multimodulus material models must wait future experimental investigation. Study of ATJ-S graphite behavior in the biaxial loading quadrants with (1) axial and circumferential compression and (2) axial tension and circumferential compression is recommended. Without such a study, the possible hardening of graphite under biaxial compression (as opposed to softening under biaxial tension) cannot be confidently predicted. Both stress states exist simultaneously in reentry vehicle nosetips so they must be well understood.

The nonlinear weighted compliance material model with the weighted energy approach is recommended for use in graphite reentry vehicle nosetip stress analysis. This recommendation is based on the fact that better strain correlation exists for that model than for the nonlinear restricted compliance material model. The lack of success with the latter model is probably due to the fact that the compliance restrictions are not satisfied for graphite material properties. The nonlinear weighted compliance material model should be regarded as an engineering approach to the nonlinear deformation problem. The various energy approaches (weighted energy, etc.) fall in the same category as opposed to the more scientific, but unsubstantiated, approach of the restricted compliance material model.

Application of the new material models to stress analysis of engineering materials other than artificial graphites should be investigated. Further theoretical refinements could be considered to increase the applicability of the new material models. The energy function for the multiaxial stress states is one phase of the material models which might be improved. The relations between tension and compression compliances in the nonlinear restricted compliance material model could be extended to arbitrary orientations of the principal material directions in the body. Currently, one principal material direction must be aligned with a body coordinate direction. Extension of the material models to analysis of general bodies under arbitrary loads is recommended. At present, the material models are limited to analysis of axisymmetrically loaded axisymmetric bodies composed of orthotropic, transversely orthotropic, or isotropic materials.

APPENDIX A COMPARISON OF THE TOTAL STRAIN ENERGY APPROACH WITH THE DISTORTIONAL ENERGY APPROACH FOR ISOTROPIC MATERIALS

The distortional energy approach is used to determine stresses, strains, and displacements in isotropic materials which deform nonlinearly [34]. The distortional energy is the single parameter used to express the level of deformation attained. Alternatively, the distortional energy can be related to a stress intensity, σ_i , where

$$\sigma_i = (\sigma_x^2 + \sigma_y^2 - \sigma_x \sigma_y + 3\tau_{xy}^2)^{1/2} \quad (35)$$

The constant of proportionality between the distortional energy and the stress intensity is $1/(6G)$ or $(1+\nu)/(3E)$. This theory is also called J_2 deformation theory of plasticity.

In J_2 theory, an equal value of σ_i is achieved for the stress state $\sigma_x = \sigma$, $\sigma_y = 0$, and $\tau_{xy} = 0$ as for $\sigma_x = 0$, $\sigma_y = 0$, and $\tau_{xy} = \sigma/\sqrt{3}$. For example, stress states with $\sigma_x = 72$ ksi and $\tau_{xy} = 41.57$ ksi have the same distortional energy and, hence, have directly relateable moduli E_{sec} and G_{sec} . That is, a relation between E_{sec} , ν , and G_{sec} ,

$$G_{sec} = \frac{E_{sec}}{2(1 + \nu)} \quad (36)$$

is enforced at all time where ν varies with the deformation level or energy level. The distortional energy is used first to calculate E_{sec} , then E_{sec} is used to calculate ν , and finally G_{sec} is calculated from Eq. (36).

However, in the present total strain energy approach, the total strain energy, not just the distortional energy component, is used. First, observe that the distortional energy is only a component of the total strain energy in the uniaxial stress-strain curve of Fig.64 (a). On the other hand, the distortional energy is equal to the total strain energy in the shear stress-shear strain curve of Fig.64 (b). In the total strain energy approach, E_{sec} is predicted first even if only τ_{xy} is applied (and hence only distortional energy exists for isotropic

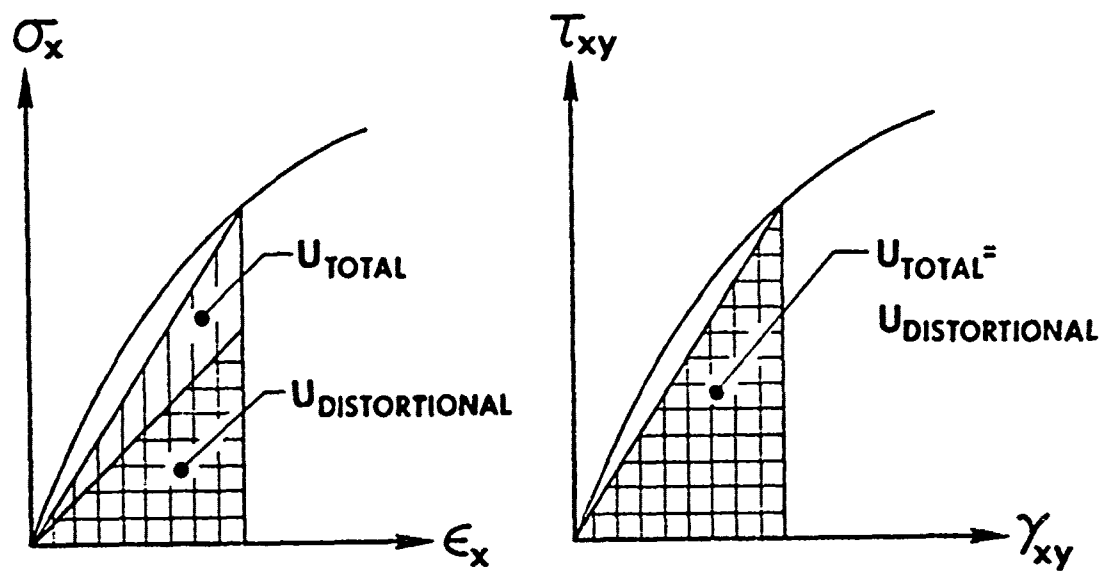


FIGURE 64 DISTORTIONAL VERSUS TOTAL STRAIN ENERGY

materials). Given a fixed applied stress τ , we use the elastic moduli to find an initial strain approximation. The associated energy (which is pure distortional energy) is used in the relation for E_{sec}

$$E_{sec} = A[1 - B(\frac{U}{U_0})^C] \quad (37)$$

to obtain a value of E_{sec} which is less than the initial value A . The coefficients A , B , and C are determined by fitting a curve to a plot of E_{sec} versus U for the uniaxial stress case σ_x versus ϵ_x . Thus, for a given value of U , a different correspondence exists between σ_x and τ_{xy} than in J_2 distortional energy theory. We will try to trace this correspondence through several iterations to predict the type of results we will obtain with our theory in comparison to J_2 theory.

First, we use elastic properties, namely G , to obtain a value of U which happens to be $U_{distortion}$ in Fig. 65. That value of U is then used in the relation for E_{sec} , Eq. (37). However, that value of U is obviously greater than $U_{distortion}$ for the uniaxial case $\sigma_x = \sigma$ in Fig. 65 indicated with point A. The corresponding point B for J_2 theory is shown in Fig. 65. The horizontally cross-hatched area associated with point B is the $U_{distortion}$ of the original τ - γ curve and the U_{total} of the σ - ϵ curve to point A. Thus, at every iteration, the value of E_{sec} is consistently higher for our total strain energy than for J_2 distortional energy theory. Accordingly, the value of G_{sec} is higher for our theory than for J_2 theory. Then, because $\gamma = \tau/G_{sec}$, the predicted shear strains for our theory are smaller than for J_2 theory when τ is specified. Finally, the total strain energy and simultaneously the distortional strain energy predicted is smaller in our theory than in J_2 theory.

Suppose we attempt to reverse the sequence of events and start with a prediction of G_{sec} instead of E_{sec} . First, we must find ν in terms of G_{sec} . We

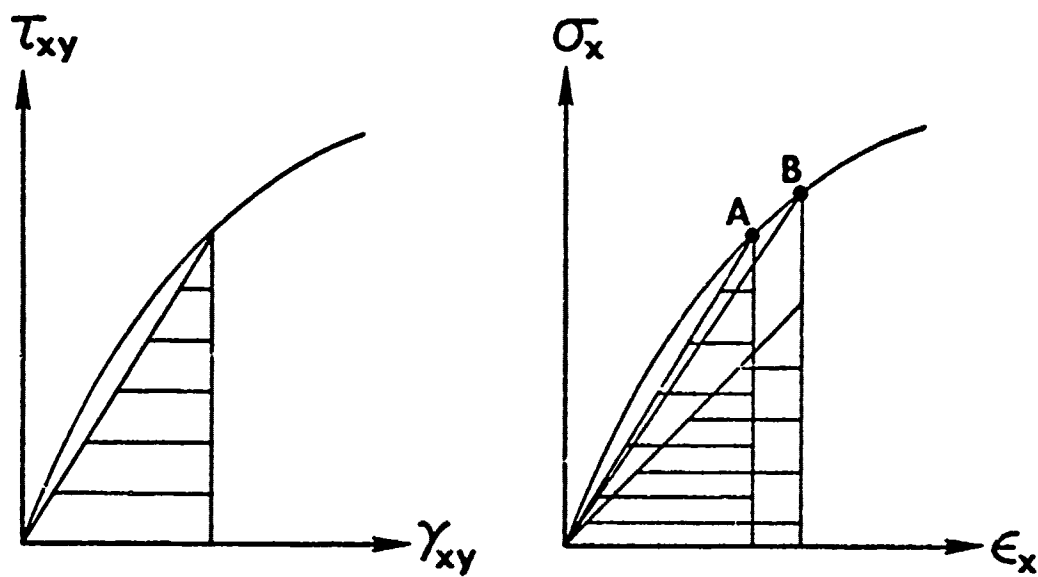


FIGURE 65 PREDICTION OF G_{sec}

know that

$$\nu = \frac{1}{2} - \left(\frac{1}{2} - \nu_e\right) \frac{E_{\text{sec}}}{E} \quad (38)$$

but because of Eq. (36),

$$\nu = \frac{1}{2} - \left(\frac{1}{2} - \nu_e\right) \frac{2(1+\nu)G_{\text{sec}}}{2(1+\nu_e)G} \quad (39)$$

whereupon, if we solve for ν ,

$$\nu = \frac{\frac{1}{2} - K G_{\text{sec}}/G}{1 + K G_{\text{sec}}/G} \quad (40)$$

where

$$K = \frac{\frac{1}{2} - \nu_e}{1 + \nu_e} \quad (41)$$

Equation (40) reduces to ν_e if $G_{\text{sec}}=G$. Then, knowing G_{sec} and ν , we can predict E_{sec} . The energy used to define the shear stress-shear strain curve is only distortional energy. Therefore, when the total strain energy is found for an arbitrary stress state (for example, the uniaxial case, σ_x versus ϵ_x) and then used to predict G_{sec} , a larger value of energy is used than in J_2 distortional energy theory. Accordingly, G_{sec} is smaller for this total strain energy approach than in distortional energy theory.

All of the foregoing rationale has been substantiated by numerical results.

REFERENCES

1. Robert M. Jones, "Reentry Vehicle Nosetip Stress Analysis," Proceedings of the Nosetip Stress Analysis Technical Interchange Meeting, (San Bernardino, California, 20 September 1967), Robert M. Jones, Editor, TR-0158 (S3816-22)-2, The Aerospace Corporation, San Bernardino, California, November 1967.
2. D. M. Forney, Jr., Editor. Graphitic Materials for Advanced Re-entry Vehicles, Part I, Analytical Techniques and Material Characterization, Air Force Materials Laboratory Technical Report AFML-TR-70-133, August 1970.
3. W. L. Greenstreet and G. C. Battle, Jr., Editors, Proceedings of Conference on Continuum Aspects of Graphite Design, (Gatlinburg, Tennessee, 9-12 November 1970), Oak Ridge National Laboratory, CONF-701105, February 1972.
4. P. J. Schneider, R. D. Teter, W. D. Coleman, and R. M. Heath, "Design of Graphite Nosetips for Ballistic Reentry", AIAA Paper 72-705.
5. Robert M. Jones and John R. Koenig, "Reentry Vehicle Nosetip Stress Analysis," Conference on Brittle Fracture of Graphites and Carbon/Carbon Composites, Asilomar, Pacific Grove, California, 27 February - 1 March 1973.
6. J. Jortner, Biaxial Mechanical Properties of ATJ-S Graphite, Final Report under AF Contract F04701-068-C-0288, Change Order 15, McDonnell-Douglas Report No. MDC G2072, December 1970.
7. J. Jortner, Multiaxial Behavior of ATJ-S Graphite, Interim Report, McDonnell-Douglas Astronautics Company, Air Force Material Laboratory Report AFML-TR-71-160, July 1971.
8. J. Jortner, Multiaxial Behavior of ATJ-S Graphite, McDonnell-Douglas Astronautics Company, Air Force Materials Laboratory Report AFML-TR-71-253, December 1971.
9. J. Jortner, Multiaxial Response of ATJ-S Graphite, McDonnell-Douglas Astronautics Company, Air Force Materials Laboratory Report AFML-TR-73-170,

October 1973.

10. J. William Davis and N. R. Zurkowski, Put the Strength and Stiffness Where You Need It, Report T-STDB(101.05)R, Reinforced Plastics Division, Minnesota Mining and Manufacturing Company.
11. Structural Design Guide for Advanced Composites Applications, Vol. 1, Material Characterization, 2nd Edition, Air Force Materials Laboratory, January 1971.
12. K. M. Kratsch, J. C. Schutzler, and D. A. Eitman, "Carbon-Carbon 3-D Orthogonal Material Behavior," AIAA Paper No. 72-365, AIAA/ASME/SAE 13th Structures, Structural Dynamics, and Materials Conference, San Antonio, Texas, 10-14 April 1972.
13. E. J. Seldin, "Stress-Strain Properties of Polycrystalline Graphites in Tension and Compression at Room Temperature," Carbon, Vol. 4 (1966), pp. 177-191.
14. K. S. Starrett and C. D. Pears, Probable and Average Properties of ATJ-S (WS) Graphite, Southern Research Institute, AFML-TR-73-14, Vol. 1, February 1973.
15. Personal communication with Dr. H. W. Babel of McDonnell-Douglas Astronautics Company, Western Division, Santa Monica, California.
16. S. A. Ambartsumyan, "The Axisymmetric Problem of a Circular Cylindrical Shell Made of Material with Different Stiffness in Tension and Compression," Izvestiya akademii nauk SSSR, Mekhanika, No. 4(1965), pp. 77-85. Translation available from STAR as N69-11070.
17. S. A. Ambartsumyan and A. A. Khachatryan, "Basic Equations in the Theory of Elasticity for Materials with Different Stiffness in Tension and Compression," Inzhenernyi zhurnal, Mekhanika tverdogo tela, No. 2(1966), pp. 44-53. Translation available as LRG-67-T-12, The Aerospace Corporation,

El Segundo, California.

18. S. A. Ambartsumyan, "Equations of the Plane Problem of the Multimodulus Theory of Elasticity," Izvestiya akademii nauk armianskoi SSR, Mekhanika, Vol. 19, No. 2(1966), pp. 3-19. Translation available as LRG-67-T-14, The Aerospace Corporation, El Segundo, California.
19. S. A. Ambartsumyan and A. A. Khachatryan, "Theory of Multimodulus Elasticity," Inzhenernyi zhurnal, Mekhanika tverdogo tela, No. 6(1966), pp. 64-67. Translation available from STAR as N67-27610.
20. Robert M. Jones, "Buckling of Circular Cylindrical Shells with Different Moduli in Tension and Compression," AIAA Journal, January 1971, pp. 53-61.
21. S. A. Ambartsumyan, "Basic Equations and Relations in the Theory of Elasticity of Anisotropic Bodies with Differing Moduli in Tension and Compression," Inzhenernyi zhurnal, Mekhanika tverdogo tela, No. 3(1969), pp. 51-61. Translation available as LRG-70-T-1, The Aerospace Corporation, El Segundo, California.
22. Robert M. Jones, "Buckling of Stiffened Multilayered Circular Cylindrical Shells with Different Orthotropic Moduli in Tension and Compression," AIAA Journal, May 1971, pp. 917-923.
23. N. G. Isabekian and A. A. Khachatrian, "On the Multimodulus Theory of Elasticity of Anisotropic Bodies in a Plane Stress State", Izvestiya Akademii Nauk Armianskoi SSR, Mekhanika, Vol. 22, No. 5(1969), pp. 25-34, IAA Accession Number A70-22152.
24. James G. Crose and Robert M. Jones, SAAS III, Finite Element Stress Analysis of Axisymmetric and Plane Solids with Different Orthotropic, Temperature-Dependent Material Properties in Tension and Compression, TR-0059(S6816-53)-1, The Aerospace Corporation, San Bernardino, California, June 1971.

25. Tu-Lung Weng, "Biaxial Fracture Strength and Mechanical Properties of Graphite-Base Refractory Composites," AIAA Paper 68-337, April 1968.
26. Tu-Lung Weng, "Stress-Strain Properties of Grade ATJ Graphite Under Combined Stresses," in Proceedings of the Conference on Continuum Aspects of Graphite Design, (Gatlinburg, Tennessee, 9-12 November 1970), W. L. Greenstreet and G. C. Battle, Jr., Editors, Oak Ridge National Laboratory, CONF-701105, February 1972.
27. Henry L. Langhaar, Energy Methods in Applied Mechanics, John Wiley and Sons, Inc., 1962, pp. 119-121.
28. Walter Ramberg and William R. Osgood, Description of Stress-Strain Curves by Three Parameters, NACA TN 902, July 1943.
29. B. M. Lempriere, "Poisson's Ratio in Orthotropic Materials," AIAA Journal, November 1968, pp. 2226-2227.
30. J. Jortner, Uniaxial and Biaxial Stress-Strain Data for ATJ-S Graphite at Room Temperature, McDonnell-Douglas Astronautics Company, Report MDC G3564, June 1972.
31. Stephen W. Tsai, A Test Method for the Determination of Shear Modulus and Shear Strength, Air Force Materials Laboratory, AFML-TR-66-372, January 1967.
32. Robert M. Jones and James G. Crose, SAAS II, Finite Element Stress Analysis of Axisymmetric Solids with Orthotropic, Temperature-Dependent Material Properties, TR-0200(S4980)-1, The Aerospace Corporation, San Bernardino, California, September 1968.
33. H. S. Starrett, Mechanical Properties of Two Billets of ATJ-S (WS) Graphite, Southern Research Institute, Air Force Materials Laboratory Report AFML-TR-73-14, Volume II, May 1973.
34. A. Nadai, Theory of Flow and Fracture of Solids, Vol. 1, McGraw-Hill, 1950.